

**Coherent spin dynamics and magnetization
transport in nanoscale magnetism**

Inauguraldissertation

zur
Erlangung der Würde eines Doktors der Philosophie

vorgelegt der
Philosophisch-Naturwissenschaftlichen Fakultät
der Universität Basel

von
Florian Meier
aus Deutschland

Basel, 2003

Genehmigt von der Philosophisch-Naturwissenschaftlichen Fakultät
auf Antrag von

Prof. Dr. Daniel Loss
Prof. Dr. Jan von Delft

Basel, den 6. Mai 2003

Prof. Dr. Marcel Tanner
Dekan

Acknowledgements

I am indebted to many people for their help and guidance during the time which I spent working on this PhD thesis. I am particularly grateful to Prof. Daniel Loss for his continuous support and innumerable stimulating discussions on fascinating problems in a rapidly evolving research field.

The research groups headed by Prof. Daniel Loss and Prof. Christoph Bruder provided an active, stimulating, and friendly environment for my work. I am indebted to all present and former members of these groups for countless discussions on physics and, just as importantly, topics totally unrelated to physics.

I was privileged to benefit from fruitful collaborations on spin cluster qubits with Prof. Jeremy Levy, and on exact diagonalization of antiferromagnetic molecular rings with Dr. Bruce Normand and Dr. Andreas Honecker.

I thank Prof. Jan von Delft for kindly accepting to coreferee this thesis.

I should like to acknowledge many people who made my time in Basel more interesting and enjoyable. I am grateful to my office mates Michael Leuenberger and William Coish and to Christoph Bruder, Florian Marquardt, and Patrik Recher for entertaining discussions; to Christian Schroll for joint runs along the Rhine; and, in particular, to Verónica Cerletti and Hanno Gassman for countless coffee breaks, a multitude of wonderful undertakings, and all the fun we had. Finally, I should like to thank my parents for their support and encouragement.

Summary

In this dissertation, we present a detailed theoretical analysis of the spin dynamics in small antiferromagnetic systems in view of macroscopic quantum phenomena, possible applications in quantum information processing, and transport of the magnetization. Ferromagnetic and antiferromagnetic systems with a size on the nanometer scale such as nanoparticles or magnetic molecular clusters, show intriguing quantum effects which are in stark contrast to the behavior of a macroscopic magnetic moment. In recent years, the interest in small magnetic systems has been renewed due to the discovery of possible future technological applications such as data storage or quantum information processing. Ferromagnetic molecular magnetic systems with a large net spin show incoherent tunneling of the magnetization on a long timescale. This quantum phenomenon is, by now, well established both experimentally and theoretically. Small antiferromagnetic systems have so far attracted less attention although quantum effects are even more pronounced than in their ferromagnetic counterparts. The main reason for this is that the predicted quantum phenomena such as coherent quantum tunneling of the Néel vector are not easily accessible in experiments. On a theoretical level, the description of an antiferromagnetic system is challenging because of the pronounced quantum fluctuations of the spins.

Several antiferromagnetic molecular ring molecules have been synthesized to date. The ferric wheels are the most prominent examples. These systems are promising candidates for macroscopic quantum coherence in the form of coherent Néel vector tunneling. Although the tunneling rate can be determined from the measurement of thermodynamic properties, a thorough understanding requires theoretical analysis and experimental observation of the spin dynamics. We calculate spin correlation functions using spin coherent state path integrals and find analytical expressions for the correlation functions of both the Néel vector and the total spin. Our results are in good agreement with numerical exact diagonalization for the small systems that are accessible numerically.

From the correlation functions, we deduce that the observation of Néel vector tunneling requires an experimental probe that couples to a single spin of the antiferromagnetic system only. Both nuclear magnetic resonance and electron spin resonance on doped rings meet this criterion. Nuclear spins coupled

only to single electron spins are ideal candidates for local probes because the nuclear spin susceptibility exhibits signatures of the coherent electron spin dynamics. Alternatively, by doping of the ring molecule, an antiferromagnetic system emerges that has uncompensated sublattice spins. The resulting tracer spin would allow one to detect Néel vector tunneling with electron spin resonance or magnetic susceptibility measurements.

Small antiferromagnetic systems with a finite net spin are interesting in view of quantum information processing. Single electron spins are among the most promising candidates for qubits in a solid state system. However, quantum computing is also possible with a wide range of antiferromagnetic clusters which form an effective two-state system in the low energy sector. The main advantage of a qubit formed by a spin cluster is that initialization, quantum gate operation, error correction, and readout are possible with techniques applicable to single spins, while the requirements on local control are relaxed. Spin cluster qubits are very insensitive to the details of intracluster exchange interactions and spin placement.

Quantum computing is only one of the exciting perspectives in the emerging field of spintronics in which the spin and charge degrees of freedom of an electron are treated on an equal footing. We analyze transport of magnetization in insulating systems described by a spin Hamiltonian in which the magnetization current is not accompanied by a charge current. The magnetization current through a quasi one-dimensional magnetic wire of finite length suspended between two bulk magnets is determined by the spin conductance which remains finite in the ballistic limit due to contact resistance. Magnetization currents produce an electric field and hence can be measured directly. For magnetization transport in an external electric field, phenomena analogous to the Hall effect emerge.

Contents

Acknowledgements	i
Summary	iii
1 Introduction	1
1.1 From classical to quantum magnetism	1
1.2 Macroscopic quantum phenomena	2
1.3 Quantum computing with spins	4
1.4 Magnetization transport	5
1.5 Outline	6
2 Coherent spin quantum tunneling	7
2.1 Spin quantum tunneling	7
2.1.1 Ferromagnetic systems	7
2.1.2 Antiferromagnetic systems	8
2.2 Antiferromagnetic molecular rings	12
2.2.1 Thermodynamic properties	13
2.2.2 Spin dynamics	17
2.3 Comparison with exact diagonalization	21
2.3.1 Na:Fe ₆	24
2.3.2 Cs:Fe ₈	30
3 Detecting macroscopic quantum coherence in antiferromagnetic molecular rings	33
3.1 Nuclear magnetic resonance	33
3.1.1 Nuclear susceptibilities	34
3.1.2 Experimental realization	38
3.1.3 ESR measurements in presence of hyperfine interactions	39
3.2 Doped antiferromagnetic molecular rings	40
3.2.1 A phenomenological model	42

3.2.2	Thermodynamics of the modified antiferromagnetic molecular rings	45
3.2.3	Dynamics of the modified antiferromagnetic molecular rings	50
3.2.4	Thermodynamics and spin dynamics for $J'/J \gg 1$ and $J'/J \ll 1$	52
3.2.5	Discussion	55
3.2.6	Spin quantum tunneling in ferritin	58
3.2.7	Conclusion	59
4	Quantum computing with spin cluster qubits	63
4.1	Spin chains	64
4.1.1	Isotropic spin chains	65
4.1.2	Varying exchange constants	71
4.1.3	Leakage	73
4.1.4	XY-like chains	76
4.1.5	Ising-like chains	79
4.1.6	Experimental realization	80
4.2	Spin clusters in $d > 2$	81
4.2.1	Bipartite lattices	81
4.2.2	Geometrically frustrated systems	82
4.2.3	Experimental realization	83
4.3	Larger spins	84
4.3.1	Antiferromagnetic molecular clusters	84
4.3.2	Hard axis systems	85
4.3.3	Easy axis systems	86
4.3.4	Experimental realization	86
4.4	Conclusion	87
5	Transport of magnetization	89
5.1	Ferromagnetic systems	90
5.2	Antiferromagnetic systems	94
5.3	Detection of spin currents	97
5.4	Spin currents in electric fields	99
5.5	Conclusion	100
A	Spin correlation functions	103
A.1	Undoped antiferromagnetic molecular rings	103
A.2	Doped antiferromagnetic molecular rings	105

B Effective coupling Hamiltonians	107
B.1 Spin chains	107
B.2 Larger spins	109
Bibliography	111
Lebenslauf	119

Chapter 1

Introduction

1.1 From classical to quantum magnetism

Magnetism was discovered by the Greek shepherd Magnes when he stepped accidentally on a lodestone and the iron nails of his boots held on to the rock – thus reports the legend. Indeed, it is likely that the stunning properties of magnetic materials were known in both Europe and China several centuries before Christ. In the 37th book of his Natural History, Pliny the Elder wrote of a hill which was made entirely of a material that attracted iron [1]. The Chinese were probably the first to realize the directive properties of lodestone in circa 100 A.D. [2].

Only from 1820 on, the theoretical understanding of magnetism started to develop. The milestones were (1) the discovery that a magnetic field is produced by an electric current, as first observed by Oersted in 1820 and described mathematically by Biot and Savart. (2) The constituents of a solid, atoms or ions, may have a net magnetic moment due to a current produced by either the orbital motion or the eigenrotation (spin) of electrons. (3) The magnetic moments of neighboring atoms or ions interact strongly with each other because, for overlapping electron wave functions, Pauli's exclusion principle puts severe constraints on the relative orientation of neighboring magnetic moments. This exchange interaction is described by the Heisenberg Hamiltonian for two neighboring spins, $\hat{\mathbf{s}}_1$ and $\hat{\mathbf{s}}_2$, $\hat{H} = J\hat{\mathbf{s}}_1 \cdot \hat{\mathbf{s}}_2$. The exchange coupling J determines whether spins and, hence, the elementary magnetic moments, align parallel ($J < 0$) or antiparallel ($J > 0$) and whether the material is ferromagnetic or antiferromagnetic, respectively. For parallel alignment, the elementary magnetic moments add up and a finite net magnetization emerges which gives rise, for example, to the orientation of a compass needle in Earth's magnetic field. The theoretical understanding of magnetism was not complete until the 20th century because magnetism results from the electron spin and the exchange

interaction, and is intrinsically a quantum mechanical effect [2].

Although magnetism originates from quantum mechanics, the magnetization \mathbf{M} of a bulk ferromagnet is classical in the sense that all three components of \mathbf{M} can be simultaneously measured with high precision. The Zeeman energy in an external magnetic field and anisotropy energies determine the potential energy for a given direction of \mathbf{M} and the minimum of the potential energy landscape is a stable equilibrium for \mathbf{M} . The magnetization of a system with length scales in the nanometer range, which consists of $10 - 10^4$ magnetic ions only, exhibits a behavior in stark contrast to the bulk system. The magnetization \mathbf{M} of the small system has an intrinsic quantum dynamics which makes it impossible to determine all components of \mathbf{M} simultaneously. If the magnetization is aligned along a direction that corresponds to a classical equilibrium, it will fluctuate around this position and may, eventually, escape from the potential well by a quantum tunneling process.

Studying the transition from classical to quantum behavior for magnetic systems is not only interesting in view of fundamental science. In magnetic storage devices such as computer hard disks, information is encoded in the magnetization vector of particles with ever decreasing size [3] and quantum tunneling of the magnetization must be avoided in order to store information reliably. In contrast to classical data storage, the new field of quantum information processing is based on the quantum mechanical behavior of, for example, small magnetic moments [4]. Utilizing magnetic moments in both classical data storage and quantum information processing requires a sound theoretical understanding of the quantum dynamics of magnetic systems.

1.2 Macroscopic quantum phenomena

The existence of quantum coherent superpositions is one of the most striking features of quantum mechanics. According to the rules of quantum mechanics, a system which has several states available can occupy several of them simultaneously rather than being restricted to a single state. Such linear superpositions are well established on the scale of single electrons with, for example, a spin state $|\psi\rangle = (|\uparrow\rangle + |\downarrow\rangle)/\sqrt{2}$. Here, $|\uparrow\rangle$ and $|\downarrow\rangle$ denote the state of a spin $s = 1/2$ pointing upward or downward, respectively. In contrast with the microscopic world of single electrons, quantum superpositions are not observed for macroscopic objects with 10^{23} particles. During the past decades, there have been significant research efforts aimed at the creation and detection of quantum superpositions for ever larger systems.

Ferromagnetic or antiferromagnetic nanoparticles or molecular clusters are promising candidates for observing quantum phenomena in systems with $10 - 10^4$ particles [5]. The main reason for this is that energy barriers in

magnetic systems are small and the systems may be well decoupled from the environment because the interaction of magnetic moments is weak. The latter is particularly important because an environment which is strongly coupled to the quantum system would permanently measure the coherent quantum state and thus destroy it, i.e., give rise to decoherence. For a magnetic system, the exchange interaction and anisotropy energy which govern the spin quantum dynamics can be determined independently, for example, from magnetization measurements. Other parameters, such as the magnitude and direction of a magnetic field, allow one to tune the properties of the magnetic system to a certain extent.

The two principal examples for quantum phenomena on the macroscopic scale are incoherent macroscopic quantum tunneling and macroscopic quantum coherence. Incoherent macroscopic quantum tunneling is the escape of a magnetic moment from a metastable state by a single quantum tunneling event. Incoherent quantum tunneling of the magnetization [6, 7, 8, 9, 10, 11, 12] has been observed in various nanoparticles and ferromagnetic molecular magnets. The most famous examples are the clusters Mn_{12} [13, 14, 15, 16, 17] and Fe_8 [18, 19, 20] for which both the interplay of thermal activation and quantum tunneling and quantum interference of different tunneling paths have been studied.

Macroscopic quantum coherence is realized when quantum tunneling between energetically degenerate and macroscopically different states occurs at a rate which is large compared to the decoherence rate. On average, the system tunnels several times between the different configurations before the coherent dynamics is disturbed by the environment. A different view of macroscopic quantum coherence is that the energy eigenstates are coherent superpositions of states which are macroscopically different – Schrödinger cat states. Evidence for macroscopic quantum coherence has been reported for various superconducting systems [21, 22, 23] and for the antiferromagnetic nanocluster ferritin [24, 25, 26, 27, 28, 29, 30, 31]. In ferritin, on the order of 10^4 Fe^{3+} ions are antiferromagnetically coupled and the spin state tunnels between two classical Néel ordered configurations. The staggered spin changes by $\sim 5 \times 10^4 \hbar$ in this process and the tunneling quantity is truly macroscopic compared to the quantum limit of single spins. Because the sublattice spins of ferritin do not, in general, have equal lengths, ferritin has a finite net spin pointing along the Néel vector that makes it possible to detect the macroscopic quantum coherence by electron spin resonance [24, 25, 26].

Macroscopic quantum coherence requires a quantum tunneling rate that is large compared to the decoherence rate. Antiferromagnetic systems are more promising candidates for the observation of quantum coherent behavior than ferromagnetic systems for the following two reasons. Firstly, the spin quantum

dynamics is generated by the antiferromagnetic exchange interaction J which is large compared to the typical energy scale of anisotropy energies. Hence, the potential barrier through which spins tunnel remains small even for large systems and the tunneling rate is larger than for a ferromagnetic system. Secondly, because of the small total magnetic moment, the coupling of an antiferromagnetic system to the environment remains small.

1.3 Quantum computing with spins

Quantum mechanical superpositions are not only interesting from a theoretical point of view. Rather, certain problems such as factoring numbers [32] or data base search [33] could be solved significantly faster with a quantum computer than with a classical computer. On a classical computer information is encoded in bits which are either “0” or “1”. The fundamental information unit of a quantum computer is a quantum bit (qubit), a quantum mechanical two-state system with basis states $|0\rangle$ and $|1\rangle$. In contrast to a classical bit, the qubit can be put into a coherent superposition $|\psi\rangle = \alpha|0\rangle + \beta|1\rangle$. Because a qubit can be in both logical states simultaneously, in a quantum algorithm many calculations can be carried out in parallel. This quantum parallelism gives rise to a significant speedup for a quantum computer compared to a classical computer. For example, for the search of a data base with N entries, the quantum computer only requires \sqrt{N} queries instead of $N/2$ queries necessary on a classical computer [33].

The implementation of qubits in a physical system is challenging because qubits need to be manipulated externally while decoherence rates should remain small. Electron [4, 34] and nuclear [35] spins have been identified as promising candidates for qubits because they are natural two state systems and because decoherence times for the spin degree of freedom are unusually large [36]. For electron spins, states with the spin pointing along \mathbf{e}_z and $-\mathbf{e}_z$, $|\uparrow\rangle$ and $|\downarrow\rangle$, are identified as logical basis states of the qubit. The manipulation of electron spins required for quantum gate operation can be achieved by magnetic fields and exchange interactions. A magnetic field B_x perpendicular to the spin quantization axis leads to a rotation of the spin from an initial state $|\uparrow\rangle$ into an arbitrary superposition $\alpha|\uparrow\rangle + \beta|\downarrow\rangle$. Similarly, an exchange interaction $J\hat{\mathbf{s}}_1 \cdot \hat{\mathbf{s}}_2$ leads to the unitary time evolution required for the SWAP gate of two qubits, $|\uparrow\rangle_1|\downarrow\rangle_2 \rightarrow |\downarrow\rangle_1|\uparrow\rangle_2$, and the additional two-qubit gates required for quantum computation such as the square-root of SWAP. After a series of quantum gates has been performed, the result of the algorithm must be read out. Schemes which make it possible to read out the state of a single spin via charge degrees of freedom are challenging but feasible with present day experimental techniques [37].

Although the spin $s = 1/2$ of a single electron is a natural candidate for a qubit, quantum computing is also possible using systems with larger spin quantum numbers. As shown recently, Grover's search algorithm could be implemented with the spin $s = 10$ of a Mn_{12} or Fe_8 molecule using a unary representation [38]. In the unary representation, numbers up to $2^N - 1$ can be encoded in $N + 1$ states of a single quantum system which makes ferromagnetic systems with a large number of states natural candidates. For universal quantum computing which requires entanglement of many effective two-state systems, antiferromagnetic clusters which form a net spin $s = 1/2$ are promising. Indeed, as will be shown in Chapter 4, quantum computing is possible not only with single spins $s = 1/2$ but rather with a wide variety of antiferromagnetic clusters for which the spin state of the cluster defines the logical qubit. This shows that antiferromagnetic nanoclusters and molecular magnets hold promising perspectives for quantum information processing.

1.4 Magnetization transport

The discovery that the spin of an electron rather than its charge may be used as an information carrier has led to the development of the field of magnetoelectronics or spintronics [39]. On both the theoretical and experimental level, transport of the spin has so far mainly been discussed for systems in which electrons are mobile and spin transport is accompanied by charge transport. Semiconductors and various ferromagnet-semiconductor heterostructures have attracted much attention because of possible future applications, for example, the spin transistor [40].

Magnetization transport is also possible in insulating systems in which all electrons are localized. In Heisenberg ferromagnets and antiferromagnets, magnetization is transported by magnons or spinons, the elementary excitations of these systems. Magnetization currents are driven by a gradient of the magnetic field, in close analogy to a charge current driven by a gradient of the electrostatic potential. In the diffusive regime, in which the magnon or spinon mean free path is short compared to the typical length scale over which the magnetic field varies, the magnetization current density is proportional to the local gradient of the magnetic field. A quantum theory for magnetization transport in the ballistic limit has, however, so far been lacking.

In the ballistic limit, the transport properties of a sample change drastically. For the charge current I between two reservoirs which are connected by a slab of width W and length L , Ohm's law predicts a conductance $G = I/V \propto W/L$. Here, eV is the difference in electrochemical potentials of the two reservoirs. However, if electrons are transported ballistically, i.e., if the electron mean free path is larger than L , charge transport is more appropriately viewed as

transmission of electrons from one reservoir to the second [41]. In the ballistic regime, the conductance $G = (2e^2/h)[k_F W]$ is independent of the length L of the slab and increases stepwise as a function of transverse width [41, 42, 43].

Naturally, the question arises whether a similar phenomenon can be expected also for the transport of magnetization. As will be shown in Chapter 5, for both ferromagnetic and antiferromagnetic systems the magnetization current between two reservoirs of magnetization connected by a quasi one-dimensional system is determined by a universal spin conductance. For a wide range of phenomena known from charge transport, analogous effects exist in the transport of magnetization.

1.5 Outline

This thesis is organized as follows. In Chapter 2, we describe macroscopic quantum coherence in the form of Néel vector tunneling in antiferromagnetic molecular rings. We calculate spin correlation functions using coherent state path integrals and compare the results with numerical exact diagonalization.

In Chapter 3, we analyze various experimental strategies which would allow one to detect Néel vector tunneling in antiferromagnetic molecular rings experimentally. Both nuclear magnetic resonance and electron spin resonance on doped antiferromagnetic rings are techniques which trace the dynamics of the Néel vector and can be used to detect spin quantum tunneling in antiferromagnetic molecular rings.

Spin clusters with antiferromagnetic intracluster coupling allow one to define a qubit, as will be shown in Chapter 4. For this spin cluster qubit, quantum computing is possible using the techniques analyzed for single-spin qubits. Compared to single spins, the requirements on local control of electric and magnetic fields are relaxed. We show that the existence of a spin cluster qubit is insensitive to the details of intracluster exchange interactions, spatial dimension, and the spin quantum numbers of the constituent spins.

In Chapter 5, the quantum limit of ballistic transport of magnetization is discussed for insulating systems described by a Heisenberg Hamiltonian for both ferromagnetic and antiferromagnetic exchange interaction. The magnetization current through a quasi one-dimensional system is determined by a spin conductance which, for the ferromagnet, is strongly temperature dependent but universal for the antiferromagnetic spin-1/2 chain. We analyze the detection of magnetization currents and develop a theory of spin transport in the presence of an external electric field.

Chapter 2

Coherent spin quantum tunneling

We review some results on spin quantum tunneling in ferromagnetic and antiferromagnetic systems (Sec. 2.1) and discuss the thermodynamic properties and spin dynamics of antiferromagnetic molecular rings [44, 45] in Sec. 2.2. In Sec. 2.3, we compare our results for spin correlation functions obtained from coherent state spin path integrals with numerical exact diagonalization [46].

2.1 Spin quantum tunneling

2.1.1 Ferromagnetic systems

In contrast to bulk systems, small ferromagnetic or antiferromagnetic systems exhibit pronounced quantum effects which can be interpreted as spin quantum dynamics [5, 6, 7, 8, 9, 10, 11, 12]. The low energy properties of a small ferromagnetic system are to a good approximation described in terms of the total spin $\hat{\mathbf{S}}$ of the system. For illustration, consider a ferromagnetic system with total spin S described by the spin Hamiltonian

$$\hat{H} = -D\hat{S}_z^2 + E(\hat{S}_+^2 + \hat{S}_-^2) \quad (2.1)$$

with $D \gg E > 0$. The ground state obtained from a classical vector model – with the spin pointing along $\pm \mathbf{e}_z$ – is no energy eigenstate of the quantum spin model. In Eq. (2.1), $\hat{S}_\pm = \hat{S}_x \pm i\hat{S}_y$, and \hat{S}_α with $\alpha = x, y, z$ are the components of the spin operator. Due to the transverse anisotropy E , the \hat{S}_z eigenstates $|m\rangle$ with $m = -S, -S + 1, \dots, S - 1, S$ are not energy eigenstates. Rather, $E \neq 0$ gives rise to a mixing of states $|m\rangle$ and $|n\rangle$ with $|m - n|/2$ integer.

More specifically, for $S = 1$, in the basis of \hat{S}_z eigenstates,

$$\hat{H} = \begin{pmatrix} -D & 0 & 2E \\ 0 & 0 & 0 \\ 2E & 0 & -D \end{pmatrix}. \quad (2.2)$$

The transverse anisotropy $E \neq 0$ lifts the degeneracy between $|-1\rangle$ and $|1\rangle$. The energy eigenstates are $|0\rangle$ and $|e_{\pm}\rangle = (|-1\rangle \pm |1\rangle)/\sqrt{2}$ with energies $E_0 = 0$ and $E_{\pm} = -D \pm 2E$, respectively.

For larger spin quantum numbers $S \geq 2$, E does not only lead to a mixing of states $|\pm m\rangle$ on opposite sites of the anisotropy barrier. Rather, energy eigenstates are complicated superpositions of several states connected by \hat{H} in Eq. (2.1). The physical properties of the system are then more easily described in terms of coherent state spin path integrals [47]. In particular, the energy splitting of the ground state doublet for integer S [5, 6, 7, 8, 9, 10],

$$\Delta_{\text{FM}} \propto e^{-S\sqrt{D/E}}, \quad (2.3)$$

can be interpreted as the tunnel splitting due to spin quantum tunneling through the energy barrier created by the axial anisotropy term proportional to D in Eq. (2.1). By comparison of Eq. (2.3) with the WKB result for the tunnel splitting of a particle with mass m in a double well potential, it is evident that a finite transverse anisotropy E leads to spin quantum dynamics similarly to the finite inverse mass $1/m \neq 0$ for a particle in a potential well. In this sense, the transverse anisotropy E generates the spin quantum dynamics in the ferromagnetic system.

The quantum spin system exhibits a rich and interesting behavior when a magnetic field \mathbf{B} is applied,

$$\hat{H} = -D\hat{S}_z^2 + E(\hat{S}_+^2 + \hat{S}_-^2) + g\mu_B(B_x\hat{S}_x + B_z\hat{S}_z). \quad (2.4)$$

The longitudinal field B_z allows one to establish or destroy the tunneling resonance between two given levels $|m\rangle$ and $|n\rangle$. The transverse field B_x gives rise to intriguing effects such as Berry phase oscillations which can be traced back to the geometrical phase acquired by a spin tunneling in a transverse magnetic field [11, 12, 48]. Spin quantum tunneling has by now been well established in various ferromagnetic molecular systems, the most widely studied being Mn_{12} and Fe_8 [13, 14, 18].

2.1.2 Antiferromagnetic systems

The theoretical description of antiferromagnetic systems is more challenging than that of their ferromagnetic counterparts which are well described in terms

of a single large spin. The main reason for this is that, in contrast to the ferromagnetic system, for the antiferromagnet the Néel ordered state is not an energy eigenstate of the quantum spin system [47]. For illustration, consider two antiferromagnetically coupled spins $\hat{\mathbf{s}}_1$ and $\hat{\mathbf{s}}_2$ with spin quantum number s and an easy axis anisotropy,

$$\begin{aligned}\hat{H} &= J\hat{\mathbf{s}}_1 \cdot \hat{\mathbf{s}}_2 - k_z (\hat{s}_{1,z}^2 + \hat{s}_{2,z}^2) \\ &= \frac{J}{2} (\hat{\mathbf{S}}^2 - 2s(s+1)) - k_z (\hat{s}_{1,z}^2 + \hat{s}_{2,z}^2).\end{aligned}\quad (2.5)$$

Here, $\hat{\mathbf{S}} = \hat{\mathbf{s}}_1 + \hat{\mathbf{s}}_2$ is the operator of total spin. For $k_z = 0$, $[\hat{\mathbf{S}}, \hat{H}] = 0$ and the total spin is a good quantum number. Diagonalization of the Hamiltonian is greatly simplified in such cases with spin symmetry. For $k_z \neq 0$, the Hamiltonian is no longer block diagonal in the S -subspaces whereas \hat{S}_z remains a good quantum number in absence of a magnetic field. Perturbation theory in the anisotropy term in Eq. (2.5) is valid as long as the typical energy scale of the anisotropy, $2k_z s^2$, is small compared to J , the characteristic energy scale of the exchange term. For $2k_z s^2 \gtrsim J$, the energy eigenstates must be determined from the diagonalization of the full Hamiltonian Eq. (2.5) in the various subspaces with given S_z .

Alternatively, for $s \gg 1$, coherent state path integrals allow one to determine thermodynamic and dynamic properties of the antiferromagnetic system [49, 50]. The spin coherent states are defined by [47, 51]

$$|\Omega\rangle = e^{i\hat{s}_z\phi} e^{i\hat{s}_y\theta} e^{i\hat{s}_x\chi} |s, m=s\rangle, \quad (2.6)$$

where $\hat{\mathbf{s}}$ is the spin operator and $\Omega = (\sin\theta \cos\phi, \sin\theta \sin\phi, \cos\theta)$ a vector on the Bloch sphere. By construction, the coherent state Eq. (2.6) is an eigenstate of $\hat{\mathbf{S}}^2$ with eigenvalue $s(s+1)$ and obeys

$$\hat{\mathbf{s}} \cdot \Omega |\Omega\rangle = s |\Omega\rangle. \quad (2.7)$$

Introducing spin coherent states $\mathbf{s}_1 = s\Omega_1$ and $\mathbf{s}_2 = s\Omega_2$, the two spin vectors \mathbf{s}_1 and \mathbf{s}_2 in Eq. (2.5) can be decomposed into a component along the Néel vector \mathbf{n} and fluctuations $\mathbf{l} \perp \mathbf{n}$ around it,

$$\mathbf{s}_1 = s\mathbf{n} + \mathbf{l}, \quad \mathbf{s}_2 = -s\mathbf{n} + \mathbf{l}. \quad (2.8)$$

Here, \mathbf{l} is the homogeneous magnetization of the system. Evaluating the partition function Z as a trace over spin coherent states and integrating out \mathbf{l} in a saddle point approximation, the partition function

$$\begin{aligned}Z &= \text{Tr} e^{-\beta\hat{H}} \\ &= \int \mathcal{D}\mathbf{n} e^{-\int d\tau L[\mathbf{n}]/\hbar}\end{aligned}\quad (2.9)$$

can be expressed as a path integral over \mathbf{n} under the constraint $\mathbf{n}^2 = 1$ [47]. The Euclidean Lagrangean

$$L[\mathbf{n}] = \frac{\hbar^2}{2J} \dot{\mathbf{n}}^2 - 2k_z s^2 n_z^2 \quad (2.10)$$

evidences that the antiferromagnetic exchange interaction J gives rise to quantum dynamics of the Néel vector \mathbf{n} . For $k_z > 0$, the anisotropy energy $-2k_z s^2 n_z^2$ creates a double well potential with minima corresponding to spin configurations with $\mathbf{n} = \pm \mathbf{e}_z$ (Fig. 2.1). In particular, for $s\sqrt{k_z/J} \gg 1$, quantum fluctuations of $\mathbf{s}_{1,2}$ around the minima are small. For low temperatures $k_B T \lesssim \Delta_{\text{AFM}}$, the antiferromagnetic system is well described by a two-state model in terms of the states $|\uparrow\rangle$ and $|\downarrow\rangle$ that correspond to the classical ground state configurations. The path integral over \mathbf{n} with the Lagrangean Eq. (2.9) can then be evaluated as sum over instanton-paths connecting the energy minima [49, 52, 53],

$$Z = 2 \cosh\left(\frac{\beta \Delta_{\text{AFM}}}{2}\right). \quad (2.11)$$

The two lowest lying states are separated in energy by the tunnel splitting

$$\Delta_{\text{AFM}} \propto e^{-4s\sqrt{k_z/J}}. \quad (2.12)$$

Because, typically, $k_z/J \ll 1$, the WKB exponent remains smaller than 10 even for large spin quantum numbers s . For given s , the tunnel splitting in the antiferromagnetic system is significantly larger than for ferromagnetic systems, Eq. (2.3), where $\sqrt{D/E}$ is of order unity.

Equation (2.12) shows that the exchange interaction J gives rise to spin dynamics in the antiferromagnetic system and, hence, spin quantum tunneling through the energy barrier provided by the easy axis anisotropy. This can also be understood directly from the Hamiltonian of the system: The transverse exchange interaction $J(\hat{s}_1^+ \hat{s}_2^- + \hat{s}_1^- \hat{s}_2^+)/2$ generates spin dynamics in the sense that it connects a Néel ordered state, such as $|m_1 = -s, m_2 = s\rangle$ with other states in the same S_z -subspace of the Hilbert space, for example, $|m_1 = -s + 1, m_2 = s - 1\rangle$.

The wave functions of the ground state doublet of Eq. (2.5), $|g\rangle = (|\uparrow\rangle + |\downarrow\rangle)/\sqrt{2}$ and $|e\rangle = (|\uparrow\rangle - |\downarrow\rangle)/\sqrt{2}$, correspond to the symmetric and antisymmetric superposition of states with \mathbf{n} centered at $\pm \mathbf{e}_z$, $|\uparrow\rangle$ and $|\downarrow\rangle$, respectively. The expectation value of staggered magnetization $\langle \hat{s}_{1,z} - \hat{s}_{2,z} \rangle$ evaluated for the states $|\uparrow\rangle$ and $|\downarrow\rangle$ differs approximately by $2s$. Hence, for $s \gg 1$, $|g\rangle$ and $|e\rangle$ are coherent superpositions of macroscopically different states, i.e., $|g\rangle$ and $|e\rangle$ are Schrödinger cat states. A state prepared in $|\uparrow\rangle$ at a time $t = 0$ will oscillate between $|\uparrow\rangle$ and $|\downarrow\rangle$ at a frequency $\omega = \Delta_{\text{AFM}}/\hbar$.

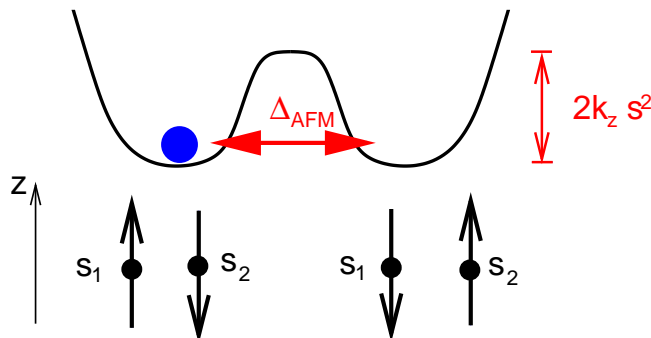


Figure 2.1: The antiferromagnetic system with easy axis anisotropy, Eq. (2.5), is mapped onto a particle in a double well potential, Eq. (2.10). The minima of the potential energy correspond to the Néel ordered configurations with \mathbf{n} pointing along $+\mathbf{e}_z$ and $-\mathbf{e}_z$, respectively. The antiferromagnetic exchange interaction generates spin dynamics which leads to spin quantum tunneling between these configurations at a rate Δ_{AFM}/h [Eq. (2.12)].

If the antiferromagnetic system is coupled to an environment, the environment leads to decoherence and the coherent oscillations between the states $|\uparrow\rangle$ and $|\downarrow\rangle$ are damped. More specifically, if the system is prepared in state $|\uparrow\rangle$ at time $t = 0$, the decoherence time $T_2 = 1/\Gamma_{\text{dec}}$ is the characteristic time in which the off-diagonal matrix elements of the density matrix in the energy eigenbasis vanish. In contrast, the relaxation time T_1 , where typically $T_1 \gtrsim T_2$, is the time scale on which the system reaches thermal equilibrium, i.e., in the energy eigenbasis:

$$\begin{aligned} \hat{\rho}(t=0) = |\uparrow\rangle\langle\uparrow| &= \frac{1}{2} \begin{pmatrix} 1 & 1 \\ 1 & 1 \end{pmatrix} \\ \xrightarrow{T_2} &\frac{1}{2} \begin{pmatrix} 1 & 0 \\ 0 & 1 \end{pmatrix} \\ \xrightarrow{T_1} &\frac{1}{2 \cosh(\beta\Delta_{\text{AFM}}/2)} \begin{pmatrix} e^{\beta\Delta_{\text{AFM}}/2} & 0 \\ 0 & e^{-\beta\Delta_{\text{AFM}}/2} \end{pmatrix}. \end{aligned}$$

The vanishing of the off-diagonal elements of the density matrix is experimentally accessible in dynamical quantities. For example, the expectation value of the staggered spin,

$$\langle \hat{s}_{1,z}(t) - \hat{s}_{2,z}(t) \rangle = 2s(\hat{\rho}_{eg}(t) + \hat{\rho}_{ge}(t)) \quad (2.13)$$

is determined by the off-diagonal matrix elements of the density matrix. This shows the importance of looking at the spin dynamics, i.e., spin correlation func-

tions, for measuring decoherence of quantum coherent oscillations [54]. Macroscopic quantum coherence is established only if the system oscillates several times between $|\uparrow\rangle$ and $|\downarrow\rangle$ before coupling to the environment destroys the coherent dynamics. Hence, $\hbar\Gamma_{\text{dec}} < \Delta_{\text{AFM}}$ is required for macroscopic quantum coherence.

For the antiferromagnetic system, due to the small WKB exponent entering the tunnel splitting, Eq. (2.12), Δ_{AFM} is typically much larger than in ferromagnetic systems. Hence, antiferromagnetic systems are more promising candidates for the observation of quantum coherent tunneling. A disadvantage of antiferromagnetic systems compared to their ferromagnetic counterparts is that the experimental detection of quantum tunneling of the Néel vector is more challenging than for quantum tunneling of the total spin, as will be discussed below.

2.2 Antiferromagnetic molecular rings: Thermodynamics and spin dynamics

Although various molecular magnetic clusters with antiferromagnetic exchange interactions have been synthesized to date, the antiferromagnetic molecular rings (AFMR's) such as various ferric wheels [55, 56, 57, 58] (see Fig. 2.2) or the Cr_8 wheel [59] are particularly appealing not only from an esthetical point of view. Rather, the high symmetry of these compounds limits the number of parameters in the microscopic spin Hamiltonian. For AFMR's in which an even number N of spins is arranged on a ring, the system is well described by the spin Hamiltonian

$$\hat{H}_0 = J \sum_{i=1}^N \hat{\mathbf{s}}_i \cdot \hat{\mathbf{s}}_{i+1} + g\mu_B \mathbf{B} \cdot \sum_{i=1}^N \hat{\mathbf{s}}_i - k_z \sum_{i=1}^N \hat{s}_{i,z}^2, \quad (2.14)$$

where $\hat{\mathbf{s}}_i$ is the spin operator at site i with spin quantum number s , $\hat{\mathbf{s}}_{N+1} \equiv \hat{\mathbf{s}}_1$, J is the nearest neighbor exchange interaction, \mathbf{B} the magnetic field, and k_z the single ion anisotropy directed along the ring axis (Fig. 2.3). The anisotropy term in Eq. (2.14) is the only second order anisotropy term possible for a system with rotational symmetry c_N . Because the g factor is well known for both the Fe^{3+} ions in the various ferric wheel compounds and the Cr^{3+} ion in the Cr_8 wheel, only k_z and J remain to be determined experimentally, for example, from the measurement of the magnetization curve as function of the magnetic field and the angle between the magnetic field and the ring axis of the molecules [60, 61]. For most AFMR's synthesized to date, J and k_z have been well established by various experimental techniques including electron spin resonance [62], specific heat [63], torque magnetometry and magnetic susceptibility [56, 57, 58, 60],

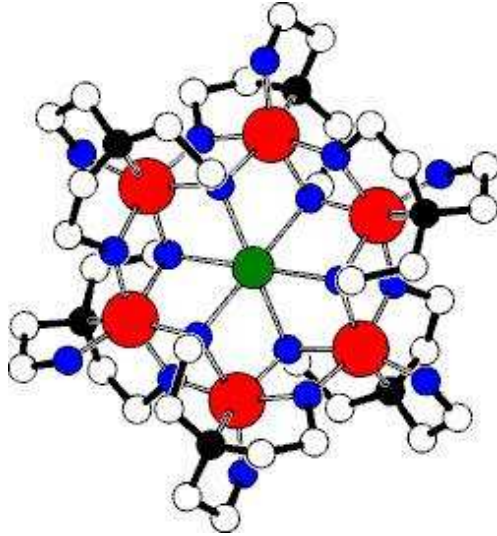


Figure 2.2: The ferric wheel NaCFe_6 . Six Fe^{3+} ions are arranged on a ring and coupled by antiferromagnetic exchange interactions.

inelastic neutron scattering [57], and spin relaxation in nuclear magnetic resonance [64].

In the following, the low energy properties of antiferromagnetic molecular rings will be discussed in view of coherent tunneling of the Néel vector. For the particularly interesting case of a magnetic field applied in the ring plane, $\mathbf{B} = B\mathbf{e}_x$, all symmetries apart from mirror reflection in the ring plane and translational invariance in Eq. (2.14) are broken and numerical exact diagonalization is challenging due to the large dimension of the subspaces of the Hilbert space in which \hat{H} is block diagonal. The description in terms of coherent state spin path integrals allows one to calculate both thermodynamic quantities and dynamic quantities analytically in the low energy sector.

2.2.1 Thermodynamic properties

All thermodynamic properties of the antiferromagnetic molecular ring can be obtained from the partition function Z_0 for the Hamiltonian \hat{H}_0 in Eq. (2.14). Introducing spin coherent states, we decompose the local spin fields \mathbf{s}_i ,

$$\mathbf{s}_i = (-1)^{i+1} \mathbf{s}\mathbf{n} + \mathbf{l}, \quad (2.15)$$

into a Néel ordered field $\pm \mathbf{s}\mathbf{n}$ ($\mathbf{n}^2 = 1$) and fluctuations $\mathbf{l} \perp \mathbf{n}$ around it. For small systems containing 6, 8, or 10 spins, spatial fluctuations of the fields \mathbf{n} and \mathbf{l} are frozen out at low temperature T . Because the typical energy scale

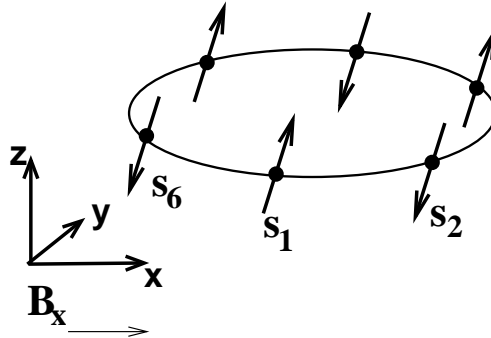


Figure 2.3: Schematic plot of the ferric wheel Fe_6 . Six Fe^{3+} ions with spin quantum number $s = 5/2$ each are arranged on a ring and coupled by an antiferromagnetic nearest neighbor exchange interaction $J > 0$. The easy axis anisotropy k_z makes energy configurations with the spins pointing along the z -axis energetically favorable.

for spatial fluctuations of \mathbf{n} is determined by the finite size gap of the magnon spectrum, $2\pi J/N$, this approximation is good for small rings but becomes questionable for increasing N . Comparison with numerical exact diagonalization in Sec. 2.3 shows that corrections due to spatial fluctuations of the Néel vector are indeed small for $N = 6$ and $N = 8$.

Carrying out the Gaussian integral over \mathbf{l} , we obtain $Z_0 = \int \mathcal{D}\mathbf{n} \exp\left(-\int_0^{\beta\hbar} d\tau L_0[\mathbf{n}]/\hbar\right)$ with a Euclidean Lagrangean depending only on \mathbf{n} [65],

$$L_0[\mathbf{n}] = \frac{N\hbar^2}{8J} [-(i\mathbf{n} \times \dot{\mathbf{n}} - \mathbf{h})^2 + (\mathbf{h} \cdot \mathbf{n})^2 - \omega_0^2 n_z^2], \quad (2.16)$$

where $\omega_0 = s\sqrt{8Jk_z}/\hbar$ and $\mathbf{h} = g\mu_B\mathbf{B}/\hbar$.

The classical ground state configurations of the easy axis antiferromagnetic ring, Eq. (2.14), correspond to the two Néel ordered states with the spins aligned along \mathbf{e}_z . In contrast to the classical description, in a quantum mechanical treatment \mathbf{n} always exhibits quantum fluctuations around its classical minima. The notion of quantum tunneling, however, is only applicable if \mathbf{n} is well localized in the states $|\uparrow\rangle$ and $|\downarrow\rangle$, i.e. if $1 - \langle \uparrow | n_z^2 | \uparrow \rangle \ll 1$. Here, $|\uparrow\rangle$ and $|\downarrow\rangle$ denote states where \mathbf{n} is centered at $\pm\mathbf{e}_z$, respectively. The quantum fluctuations of \mathbf{n} can be estimated from Eq. (2.16). For $\mathbf{h} = 0$, L_0 describes two independent harmonic oscillators of frequency ω_0 , corresponding to fluctuations of \mathbf{n} in the direction of \mathbf{e}_x and \mathbf{e}_y . If the amplitude of the fluctuations is small, we can evaluate the mean deviation of the Néel vector from \mathbf{e}_z , $1 - \langle n_z^2 \rangle \simeq 2/(\mathcal{S}_0/\hbar)$, where $\mathcal{S}_0/\hbar = Ns\sqrt{2k_z/J}$ is the classical tunnel action. Hence, \mathbf{n} is well localized

along \mathbf{e}_z only if $\mathcal{S}_0/\hbar \gg 2$ or, equivalently, if the ground-state energy, $2 \times \omega_0/2$, is small compared to the potential barrier $Nk_z s^2$. The scenario changes if a strong magnetic field $\mathbf{h} = h_x \mathbf{e}_x$, $h_x \gg \omega_0$, is applied in the ring plane. Then, the mode of \mathbf{n} along \mathbf{e}_x is frozen out, such that $1 - \langle n_z^2 \rangle \simeq 1/(\mathcal{S}_0/\hbar)$, and the AFMR exhibits quantum tunneling if $\mathcal{S}_0/\hbar \gg 1$. Note that for large tunnel action, $\mathcal{S}_0/\hbar \gtrsim 10$, the tunnel splitting becomes small, which would make the system under consideration a less favorable candidate for the observation of coherent quantum tunneling.

The AFMR's Li:Fe₆, Na:Fe₆, Cs:Fe₈, Fe₁₀, and Cr₈ have been well characterized [55, 56, 57, 58, 59, 60, 61]. For Fe₁₀, $J = 15.56\text{K}k_B$ and $k_z = 0.0088J$. For Cs:Fe₈, $J = 22.5\text{K}k_B$ and $k_z = 0.0185J$ [58]. For Fe₆, J and k_z vary appreciably depending on the central alkali metal ion and ligands: for Na:Fe₆, $J = 32.77\text{K}k_B$ and $k_z = 0.0136J$, whereas for Li:Fe₆, $J = 20.83\text{K}k_B$ and $k_z = 0.0053J$ [60, 61]. For Cr₈, $J = 17.2\text{K}k_B$ and $k_z = 0.0154J$. In Table 2.1, \mathcal{S}_0/\hbar and $\hbar\omega_0/2\mu_B$ are given for Fe₁₀, Cs:Fe₈, Na:Fe₆, Cr₈, and Li:Fe₆. As is obvious from these values, for none of the molecular rings \mathcal{S}_0/\hbar is sufficiently large to assure that a tunnel scenario is rigorously applicable if $h_x \lesssim \omega_0$. In Na:Fe₆, even at large $B_x \gg 20\text{T}$, \mathbf{n} is far less well localized along \mathbf{e}_z than in Fe₁₀ or Cs:Fe₈, which hence remain the most favorable candidates for the observation of quantum tunneling. Note however that even in Fe₁₀ and Cs:Fe₈, \mathcal{S}_0/\hbar is so small that corrections to the instanton techniques applied below may become large.

For $h_x \gg \omega_0$, the magnetic field \mathbf{B} strongly confines \mathbf{n} to the (y, z) -plane and thus determines the tunneling path of the electron spins. This allows one to further evaluate Z_0 . We parameterize

$$\mathbf{n} = (\cos \theta, \sin \theta \cos \phi, \sin \theta \sin \phi) \quad (2.17)$$

and expand L_0 [Eq. (2.16)] to second order in $\vartheta = \theta - \pi/2$,

$$L_0[\mathbf{n}] = \frac{N\hbar^2}{8J} [-(h_x - i\dot{\phi})^2 - \omega_0^2 \sin^2 \phi] + \frac{1}{2} \vartheta G^{-1}[\phi] \vartheta, \quad (2.18)$$

	N	s	k_z/J	\mathcal{S}_0/\hbar	$\hbar\omega_0/2\mu_B$
Fe ₁₀	10	5/2	0.0088	3.32	7.68T
Cs:Fe ₈	8	5/2	0.0185	3.85	16.37T
Na:Fe ₆	6	5/2	0.0136	2.47	20.11T
Cr ₈	8	3/2	0.0154	2.07	6.4T
Li:Fe ₆	6	5/2	0.0053	1.54	7.98T

Table 2.1: $\mathcal{S}_0/\hbar = Ns\sqrt{2k_z/J}$ and $\hbar\omega_0/2\mu_B$ for Fe₁₀, Cs:Fe₈, Na:Fe₆, Cr₈, and Li:Fe₆.

where $G^{-1}[\phi] = (N\hbar^2/4J)(-\partial_\tau^2 + (h_x - i\dot{\phi})^2 + \omega_0^2 \sin^2 \phi)$, $\dot{\phi} = \partial_\tau \phi$, and $\omega_0 = s\sqrt{8Jk_z}/\hbar$ as defined above. The typical energy scales for the dynamics of ϕ and ϑ are ω_0 and h_x , respectively. Because, by assumption, $h_x \gg \omega_0$, we can use an adiabatic approximation, in which ϑ oscillates rapidly in a quasistatic harmonic potential $(N\hbar^2/8J)(h_x^2 - 2ih_x\dot{\phi})$. Integrating out ϑ , we obtain an expression for L_0 depending only on ϕ [65]. For $k_B T/\hbar \ll \omega_0 \ll h_x$, we find

$$L_0[\phi] \simeq \frac{N\hbar^2}{8J} [-(h_x - i\dot{\phi})^2 - \omega_0^2 \sin^2 \phi] + \hbar \frac{h_x - i\dot{\phi}}{2} + \mathcal{O}(\omega_0^2/h_x), \quad (2.19)$$

where the term $\hbar(h_x - i\dot{\phi})/2$ arises from the ϑ fluctuation determinant. The two saddle-points of Eq. (2.19), $\phi \equiv \pi/2$ and $\phi \equiv 3\pi/2$, correspond to the two classical ground state spin configurations. If tunneling is weak, $\mathcal{S}_0/\hbar \gg 1$, the remaining path integral over ϕ is straightforward [53, 65]. Summing all multi-instanton solutions, one finds

$$Z_0 = 2 \exp \left[\beta \left(\frac{N\hbar^2}{8J} h_x^2 - \hbar \frac{h_x + \omega_0}{2} \right) \right] \cosh \left(\frac{\beta \Delta(h_x)}{2} \right) \quad (2.20)$$

with the tunnel splitting

$$\Delta(h_x) = \Delta_0 \left| \sin \left(\pi \frac{N\hbar}{4J} h_x \right) \right|, \quad (2.21)$$

where $\beta = 1/k_B T$, $\Delta_0 = 8\hbar\omega_0\sqrt{\mathcal{S}_0/2\pi\hbar} \exp(-\mathcal{S}_0/\hbar)$, and $\mathcal{S}_0/\hbar = Ns\sqrt{2k_z/J}$. In particular, Δ is periodic as a function of h_x . Differentiating with respect to B_x , we obtain the magnetization [65]

$$M_x = (g\mu_B) \left[\frac{N\hbar}{4J} h_x - \frac{1}{2} + \frac{1}{2\hbar} \frac{\partial \Delta}{\partial h_x} \tanh \left(\frac{\beta \Delta}{2} \right) \right]. \quad (2.22)$$

Because $\partial \Delta / \partial h_x$ is discontinuous at the zeroes of Δ , M_x exhibits steps at $B_{c,n} = n4J/Ng\mu_B$, where $n = 1, 2, \dots, Ns$. From

$$M_\alpha = (g\mu_B) \frac{N\hbar}{4J} \frac{1}{Z} \int \mathcal{D}\mathbf{n} [h_\alpha - i(\mathbf{n} \times \dot{\mathbf{n}})_\alpha - n_\alpha \mathbf{h} \cdot \mathbf{n}] \times e^{-\int_0^{\beta\hbar} d\tau L_0[\mathbf{n}]/\hbar}, \quad (2.23)$$

it also follows that, for arbitrary h_x , $M_\alpha = 0$ for $h_\alpha = 0$, $\alpha = y, z$, which is implied by the invariance of \hat{H}_0 under rotation around \mathbf{B} by π .

More generally, from the partition function Eq. (2.20) and the free energy $F = -k_B T \ln Z$, one can calculate all thermodynamic properties of the anti-ferromagnetic molecular rings in the low temperature regime $T \lesssim \Delta/k_B$ where

$$\begin{aligned}
|g\rangle &= (|\uparrow\downarrow\uparrow\downarrow\rangle + |\downarrow\uparrow\downarrow\uparrow\rangle) / \sqrt{2} \\
|e\rangle &= (|\uparrow\downarrow\uparrow\downarrow\rangle - |\downarrow\uparrow\downarrow\uparrow\rangle) / \sqrt{2}
\end{aligned}$$

Figure 2.4: Schematic representation of the ground state doublet of an AFMR in the tunneling regime, $\mathcal{S}_0/\hbar \gg 2$. $|g\rangle$ and $|e\rangle$ are coherent superpositions of macroscopically different states.

only the two tunnel-split levels, the ground state and the first excited state of the ring, are thermally populated. For example, the specific heat c_V is expected to exhibit the Schottky anomaly characteristic for a two-state system. $c_V(T)$ has a maximum at $T = 0.4\Delta/k_B$ [65].

In conclusion, from the semiclassical analysis the following picture of the low-energy properties of antiferromagnetic molecular rings emerges [65, 44, 45]. There is a doublet of tunnel-split states. The ground state $|g\rangle$ and first excited state $|e\rangle$ are the symmetric and antisymmetric superposition, respectively, of states with the Néel vector centered around $\pm\mathbf{e}_z$, $|\uparrow\rangle$ and $|\downarrow\rangle$, respectively,

$$|g\rangle = \frac{1}{\sqrt{2}}(|\uparrow\rangle + |\downarrow\rangle), \quad |e\rangle = \frac{1}{\sqrt{2}}(|\uparrow\rangle - |\downarrow\rangle). \quad (2.24)$$

These energy eigenstates are shown schematically in Fig. 2.4.

2.2.2 Spin dynamics

Thermodynamic properties, such as the rounding of the magnetization steps $M_x(B_x)$ or the Schottky anomaly in the low temperature specific heat $c_V(T)$ provide a first experimental test for the functional dependence of $\Delta(B_x)$ [65]. More information can be obtained from dynamic quantities, i.e., response functions. In particular, quantum coherent tunneling requires a decoherence rate Γ_{dec} much smaller than the tunneling rate Δ/\hbar . An upper bound for Γ_{dec} is given by the linewidth of the resonance line corresponding to a transition between the tunnel split states at $\omega = \Delta/\hbar$ in an electron spin resonance (ESR) or nuclear magnetic resonance (NMR) experiment. The identification of a correlation function which provides the signature of Néel vector tunneling is essential to aid the experimental search for macroscopic quantum coherence in AFMR's. We next calculate the correlation functions of the total spin $\hat{\mathbf{S}}$ and the Néel vector $\hat{\mathbf{n}}$ using coherent state spin path integrals.

Correlation function of total spin

The correlation function of the total spin of the ring, $\hat{\mathbf{S}} = \sum_{i=1}^N \hat{\mathbf{s}}_i$,

$$\chi_{\alpha\alpha}(i\omega_n) = (g\mu_B)^2 \int_0^{\beta\hbar} d\tau e^{i\omega_n\tau} [\langle T_\tau \hat{S}_\alpha(\tau) \hat{S}_\alpha(0) \rangle - \langle \hat{S}_\alpha \rangle^2], \quad (2.25)$$

where $\alpha = x, y, z$, is experimentally accessible, e.g., in alternating current (AC) susceptibility or ESR measurements. However, $\chi_{\alpha\alpha}(i\omega_n)$ contains *no* terms proportional to $1/(i\omega_n - \Delta/\hbar)$ as we will show below. This implies that AC susceptibility or ESR measurements cannot be used to detect Néel vector tunneling in AFMR's described by Eq. (2.14).

$\chi_{xx}(i\omega_n)$ can be calculated from the generating functional $Z[\delta h_x(\tau)]$, where $\delta h_x(\tau)$ is a small probing field added to the static field $h_x \gg \omega_0$. Because we are only interested in the low frequency response of the AFMR, $\omega_n \lesssim \Delta/\hbar \ll \omega_0$, we may restrict our attention to a slowly varying field δh_x whose Fourier components vanish for $\omega_n \gtrsim \Delta/\hbar$. The typical timescale for the dynamics of ϕ , $1/\omega_0$, is short compared to the timescale on which δh_x varies. In particular, approximating $\delta h_x(\tau)$ by a constant during instanton passage, we find

$$Z[\delta h_x(\tau)] \simeq 2 \exp\left[\int_0^{\beta\hbar} \frac{d\tau}{\hbar} \left(\frac{N\hbar^2}{8J} (h_x + \delta h_x(\tau))^2 - \hbar \frac{h_x + \delta h_x(\tau) + \omega_0}{2} \right) \cosh\left[\int_0^{\beta\hbar} \frac{d\tau}{\hbar} \frac{\Delta(h_x + \delta h_x(\tau))}{2}\right]\right]. \quad (2.26)$$

Differentiating twice and setting $\delta h_x \rightarrow 0$, for $\omega_n \lesssim \Delta/\hbar$,

$$\chi_{xx}(i\omega_n) = (g\mu_B)^2 \left[\frac{N\hbar}{4J} + \frac{1}{2\hbar} \frac{\partial^2 \Delta}{\partial h_x^2} \tanh(\beta\Delta/2) + \frac{\beta}{\hbar} \left(\frac{1}{2} \frac{\partial \Delta}{\partial h_x} \right)^2 \cosh^{-2}(\beta\Delta/2) \delta_{\omega_n,0} \right]. \quad (2.27)$$

Here, Δ is the tunnel splitting defined in Eq. (2.21).

The transverse susceptibilities can be evaluated directly from $\delta^2 Z / \delta h_\alpha(\tau) \delta h_\alpha(0)$, $\alpha = y, z$. Using the parameterization in Eq. (2.17), $\vartheta = \theta - \pi/2$ can be integrated out in the path-integral expression for $\chi_{\alpha\alpha}$. We obtain for $\omega_n \ll h_x$ (see Appendix A.1 for further details)

$$\begin{aligned} \chi_{yy}(i\omega_n) &\simeq (g\mu_B)^2 \frac{N\hbar}{4J}, \\ \chi_{zz}(i\omega_n) &\simeq (g\mu_B)^2 \frac{N\hbar}{4J}. \end{aligned} \quad (2.28)$$

From Eqs. (2.27) and (2.28) it is evident that none of the susceptibilities $\chi_{\alpha\alpha}(i\omega_n)$ contains a term proportional to $1/(i\omega_n \pm \Delta/\hbar)$. In the tunneling regime discussed here, $|g\rangle$ and $|e\rangle$ are energetically well separated from all other states. Then, Eq. (2.28) and the spectral representation

$$\chi_{\alpha\alpha}(i\omega_n) = \sum_{i,j} \frac{e^{-\beta E_i}}{Z} |\langle i|\hat{S}_\alpha|j\rangle|^2 \left(\frac{1}{i\omega_n - (E_i - E_j)/\hbar} - \frac{1}{i\omega_n + (E_i - E_j)/\hbar} \right) - \beta\hbar\delta_{\omega_n,0} \langle \hat{S}_\alpha \rangle^2, \quad (2.29)$$

where $|i\rangle$ and $|j\rangle$ label energy eigenstates, imply that $\langle e|\hat{S}_\alpha|g\rangle = 0$ ($\alpha = x, y, z$). Although for the parameters of Fe₁₀, Cs:Fe₈, Na:Fe₆, and Cr₈ tunnel corrections to $\chi_{\alpha\alpha}$ neglected in Eq. (2.28) can be significant, the main conclusion of our calculation – that coherent tunneling of \mathbf{n} does not enter the susceptibilities $\chi_{\alpha\alpha}$ – remains valid.

Indeed, $\langle e|\hat{S}_\alpha|g\rangle = 0$ is a direct consequence of the invariance of \hat{H}_0 as $i \rightarrow i + 1$, i.e., the exchange of the two sublattices of the bipartite AFMR. In order to clarify this point, we introduce the sublattice spin operators

$$\hat{\mathbf{S}}_A = \sum_{i \text{ odd}} \hat{\mathbf{s}}_i, \quad \hat{\mathbf{S}}_B = \sum_{i \text{ even}} \hat{\mathbf{s}}_i. \quad (2.30)$$

with $\hat{\mathbf{S}} = \hat{\mathbf{S}}_A + \hat{\mathbf{S}}_B$. In a semiclassical description of the AFMR, spins of one sublattice couple ferromagnetically to each other. The classical spin fields \mathbf{s}_i then obey $\mathbf{s}_i = \mathbf{S}_A/(N/2)$ for odd i , and $\mathbf{s}_i = \mathbf{S}_B/(N/2)$ for even i . This amounts to treating \mathbf{S}_A and \mathbf{S}_B as single large spins [49, 50, 66] with spin quantum number $Ns/2$, and \hat{H}_0 reduces to

$$\hat{H}_{0,\text{subl}} = \frac{4J}{N} \hat{\mathbf{S}}_A \cdot \hat{\mathbf{S}}_B + \hbar\mathbf{h} \cdot (\hat{\mathbf{S}}_A + \hat{\mathbf{S}}_B) - \frac{2k_z}{N} (\hat{S}_{A,z}^2 + \hat{S}_{B,z}^2). \quad (2.31)$$

Similarly to the nonlinear sigma model formalism used above, $\hat{H}_{0,\text{subl}}$ provides an appropriate description of the low-energy physics of the AFMR.

In Fig. 2.5, the two classical ground-state spin configurations of $\hat{H}_{0,\text{subl}}$ are shown. A finite magnetic field \mathbf{B} tilts the sublattice spins toward \mathbf{B} such that $\mathbf{S} = \mathbf{S}_A + \mathbf{S}_B$ is parallel to \mathbf{B} . On tunneling of \mathbf{n} , the sublattice spins retain their positions relative to each other and rotate jointly around \mathbf{e}_x . The total spin vector \mathbf{S} , however, remains invariant during tunneling such that the real-time spin correlation function does not contain terms proportional to $e^{i\Delta t/\hbar}$ or, equivalently, $\langle e|\hat{S}_\alpha|g\rangle = 0$.

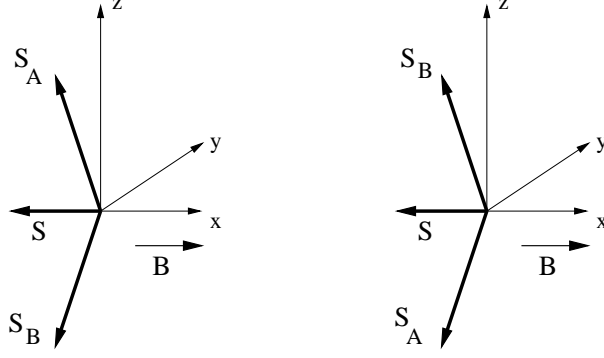


Figure 2.5: Sublattice spins and total spin of the AFMR in a magnetic field \mathbf{B} .

Correlation function of the Néel vector

Although the dynamics of the total spin does not provide information on the quantum tunneling of the Néel vector, the tunneling dynamics with tunnel frequency Δ/\hbar enters the correlation function of the Néel vector, as will be detailed next.

We define the Néel vector operator

$$\hat{\mathbf{n}} = \frac{1}{N_S} \sum_i^N (-1)^{i+1} \hat{\mathbf{s}}_i. \quad (2.32)$$

The correlation function of the Néel vector is difficult to measure directly. However, it is closely related to the correlation function of a single spin,

$$\langle \hat{s}_{i,\alpha}(t) \hat{s}_{i,\alpha} \rangle \simeq s^2 \langle n_\alpha(t) n_\alpha \rangle, \quad (2.33)$$

where $i = 1, \dots, N$. For low temperatures $T \lesssim \Delta/k_B$, we find

$$\begin{aligned} \langle \hat{n}_z(t) \hat{n}_z \rangle &\simeq \frac{|\langle e | \hat{n}_z | g \rangle|^2 (e^{\beta\Delta/2} e^{i\Delta t/\hbar} + e^{-\beta\Delta/2} e^{-i\Delta t/\hbar})}{2 \cosh(\beta\Delta/2)} \\ &\simeq \frac{e^{\beta\Delta/2} e^{i\Delta t/\hbar} + e^{-\beta\Delta/2} e^{-i\Delta t/\hbar}}{2 \cosh(\beta\Delta/2)}, \end{aligned} \quad (2.34)$$

where $|g\rangle$ and $|e\rangle$ denote the ground and first excited state of the antiferromagnetic ring, respectively. Equation (2.34) follows from Eq. (2.24) for the tunneling regime, the relations

$$\begin{aligned} \hat{n}_z |g\rangle &\simeq |e\rangle, \\ \hat{n}_z |e\rangle &\simeq |g\rangle \end{aligned} \quad (2.35)$$

and

$$\begin{aligned}\hat{n}_z|\uparrow\rangle &\simeq |\uparrow\rangle, \\ \hat{n}_z|\downarrow\rangle &\simeq -|\downarrow\rangle.\end{aligned}\tag{2.36}$$

Quantum fluctuations around the minima in the action Eq. (2.18) lead to a reduction of the matrix element $|\langle e|\hat{n}_z|g\rangle|$ in Eq. (2.34) compared to 1 by $1/(\mathcal{S}_0/\hbar)$. The fluctuation-dissipation theorem implies that, because of Eq. (2.34), the imaginary part of the Néel vector susceptibility exhibits a delta peak at the tunnel frequency of the Néel vector,

$$\begin{aligned}\chi''_{n_z n_z}(\omega \simeq \Delta/\hbar) &= \frac{1}{2} \int_{-\infty}^{\infty} dt e^{i\omega t} \langle [\hat{n}_z(t), \hat{n}_z] \rangle \\ &\simeq \pi \tanh\left(\frac{\beta\Delta}{2}\right) \delta(\omega - \Delta/\hbar).\end{aligned}\tag{2.37}$$

In presence of decoherence, the delta peak will be broadened. The linewidth provides an upper limit for the decoherence rate Γ_{dec} of the Néel vector tunneling. This illustrates that measurement of dynamic quantities, i.e., frequency dependent response functions, is vital in order to determine whether quantum coherence is established ($\Gamma_{\text{dec}} < \Delta/\hbar$) or quantum tunneling is incoherent ($\Gamma_{\text{dec}} \gtrsim \Delta/\hbar$).

Finally, it should be pointed out that the observation of an approximate single-frequency oscillation in a correlation function, e.g. $\langle n_z(t)n_z \rangle$ for the AFMR, does not prove the existence of a quantum tunneling phenomenon. Rather, the measurement of a dynamic quantity must be supplemented by additional information on the confining potential for the system under consideration, i.e., the easy axis anisotropy parameter k_z for the present case.

2.3 Comparison with exact diagonalization

The semiclassical analysis of AFMR's presented in Secs. 2.2.1 and 2.2.2 is based on the following assumptions:

- (i) The spin quantum number s is sufficiently large that $1/s$ -corrections in the spin path integral are negligible.
- (ii) Spatial fluctuation of the Néel vector and the homogeneous magnetization are small in rings with $N = 6, 8,$ and 10 .
- (iii) The tunnel action \mathcal{S}_0/\hbar is sufficiently large that the partition function can be evaluated using the non-interacting instanton approximation.

As shown in Table 2.1, the AFMR's available are marginal in view of quantum tunneling because the tunnel actions are of order $\mathcal{S}_0/\hbar \sim 2-4$. In order to estimate the quality of the semiclassical approach discussed in Secs. 2.2.1 and 2.2.2, we now compare our results with numerical exact diagonalization. The rigid rotor approach [65], in which assumption (i) and (ii) are also invoked but no tunneling regime is assumed allows us to estimate the errors introduced by (i) and (ii). Lanczos exact diagonalization techniques have previously been applied only for the ground state, in order to compute magnetization and torque as a function of applied field [61]. We will focus on the dynamical properties of the molecular rings Na:Fe₆ and Cs:Fe₈. We present a detailed investigation of the dynamical properties of ferric wheels which require that excited states and all corresponding matrix elements be taken into account. We work within the minimal model Hamiltonian for AFMR's with effective uniaxial anisotropy, Eq. (2.14). For finite anisotropy the total spin is not a good quantum number because $k_z \neq 0$ leads to mixing of different spin multiplets which makes numerical exact diagonalization challenging.

The dynamical variables we consider are the autocorrelation functions of the total-spin and Néel-vector operators, $\langle \hat{S}_\alpha(t) \hat{S}_\alpha(0) \rangle$ and $\langle \hat{n}_\alpha(t) \hat{n}_\alpha(0) \rangle$, from which one may seek temporal oscillations characteristic of coherent tunneling dynamics. Working with correlation functions of total spin and Néel vector is advantageous because it allows one to retain some of the spatial symmetries in numerical exact diagonalization. This simplifies the computation of matrix elements of $\hat{\mathbf{S}}$ and $\hat{\mathbf{n}}$ required in addition to the energy spectra for a full understanding of the dynamics.

The dynamical response of a single spin of the AFMR may also be considered directly. However, we state that all relevant dynamical properties are encoded in the two correlation functions $\langle \hat{S}_\alpha(t) \hat{S}_\alpha(0) \rangle$ and $\langle \hat{n}_\alpha(t) \hat{n}_\alpha(0) \rangle$, and show that the single-spin quantities can be deduced from these as follows. We denote by e^{ip} the eigenvalue of the one-site translation operator on the ring, and presume that all low-energy states are contained in the sectors $p = 0$ and $p = \pi$, a fact we will verify below. If the ground state, $|g\rangle$, is in the sector $p = 0$, then matrix elements $\langle i | S_\alpha | g \rangle$ are finite only for states $|i\rangle$ in the sector $p = 0$ and matrix elements $\langle i | n_\alpha | g \rangle$ are finite only for states $|i\rangle$ in the sector $p = \pi$. Because all states considered are invariant under translations by two lattice sites, $\hat{\mathbf{S}}$ may be approximately substituted by $\frac{1}{2}N(\hat{\mathbf{s}}_1 + \hat{\mathbf{s}}_2)$ and $\hat{\mathbf{n}}$ by $\frac{1}{2s}(\hat{\mathbf{s}}_1 - \hat{\mathbf{s}}_2)$. It follows that single-spin correlation functions are given at low frequencies by

$$\langle \hat{s}_{1\alpha}(t) \hat{s}_{1\alpha}(0) \rangle \simeq s^2 \langle \hat{n}_\alpha(t) \hat{n}_\alpha(0) \rangle + \frac{1}{N^2} \langle \hat{S}_\alpha(t) \hat{S}_\alpha(0) \rangle, \quad (2.38)$$

because the cross-correlation functions $\langle \hat{n}_\alpha(t) \hat{S}_\alpha(0) \rangle$ vanish due to the opposing symmetries of $\hat{\mathbf{n}}$ and $\hat{\mathbf{S}}$ under one-site translation.

Taking as a guide the semiclassical treatment in Sec. 2.2.2, a tunneling scenario is applicable if the ground and first excited states, $|g\rangle$ and $|e\rangle$, are energetically well separated from all other states and form a (weakly) tunnel-split doublet with splitting $\Delta = E_e - E_g$. Because the states $|g\rangle$ and $|e\rangle$ have opposing behavior under translation, as mentioned above, the total-spin matrix element vanishes in this manifold, $\langle e|\hat{\mathbf{S}}|g\rangle = 0$, and $\langle \hat{S}_z(t)\hat{S}_z(0)\rangle$ has no coherent oscillations with period characteristic of the tunneling time h/Δ . This result has been obtained in Sec. 2.2.2 using a spin path integral formalism. By contrast, the dynamical properties of the Néel vector are dominated by tunneling in the lowest manifold, $|\langle e|\hat{n}_z|g\rangle| \sim 1$, so that $\langle \hat{n}_z(t)\hat{n}_z(0)\rangle$ should exhibit coherent oscillations with period $2\pi/\Delta$.

The complete Hilbert spaces for Fe_6 and Fe_8 rings contain $6^6 = 46656$ and $6^8 = 1679616$ states, respectively. Due to the presence of the single ion anisotropy ($k_z \neq 0$) in Eq. (2.14), there are no symmetries in spin space for a magnetic field applied at a generic angle to the z -direction, leaving the spatial symmetries of one-site translation and reflection at a given site. The ground state in a magnetic field is always located either in the sector with $p = 0$ or with $p = \pi$ and has positive parity with respect to site reflection. These two sectors also contain the lowest excitations. The dimensions of these sectors are 4291 (107331) for $p = 0$ and 4145 (106680) for $p = \pi$ in the case of Fe_6 (Fe_8). Since the Néel vector connects these two subspaces, we work in the sum of the two spaces for the computation of matrix elements and correlation functions. For Fe_6 we have computed the lowest 350 eigenvectors and eigenvalues in the subspace of dimension 8436. We estimate that this truncation leads to errors in the temporal correlation functions on the order of 10^{-6} of the peak values, meaning that the truncation error is undetectable in any of the figures below for Fe_6 , while numerical errors for the individual eigenstates are considerably smaller still. For Fe_8 we have retained the lowest 50 energy levels in the combined subspace, and have an estimated truncation error on the order of 10^{-4} of the peak values in the temporal correlation functions. All of our results are obtained for zero temperature using the minimal Hamiltonian Eq. (2.14), and so include no source of decoherence.

We will focus on magnetic fields applied in the plane of the ring, the geometry which retains the highest tunnel barrier, with maximal localization of the Néel vector, at given field. We have also considered field angles out of the plane of the ring, and confirmed that they yield qualitatively similar results at strong fields. This is to be expected because the physical situation remains one in which the spins are largely confined to a planar motion between two potential minima. Here we calculate dynamical quantities and discuss the information they contain on quantum coherent tunneling.

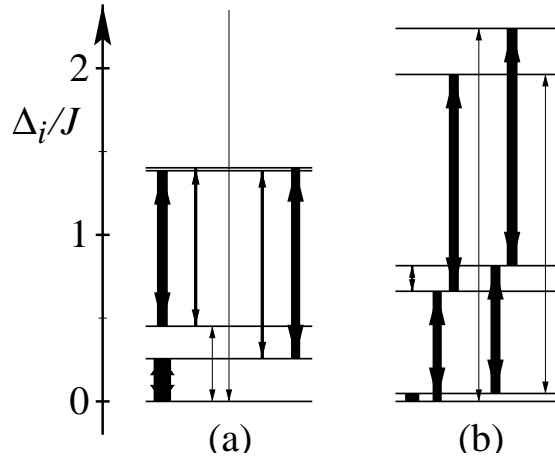


Figure 2.6: Lowest energy level spacings $\Delta_i = E_i - E_g$ for an Na:Fe₆ ring described by the minimal Hamiltonian (2.14), for applied fields $g\mu_B B_x = 3.1J$ (a) and $g\mu_B B_x = 3.5J$ (b). The thickness of the vertical lines represents the magnitude of the matrix elements of \hat{n}_z connecting each level pair.

2.3.1 Na:Fe₆

We begin with a discussion of the energy spectrum for Na:Fe₆, for which $k_z/J = 0.0136$ in Eq. (2.14) [61]. Fig. 2.6 shows the lowest energy levels for two fields chosen near the center of a magnetization plateau (a) and very close to a level crossing (b) (see Figs. 2.9 and 2.10 below). Near the level crossing, there are indeed two nearly degenerate levels lying well below any of the others, but we stress that this alone is not sufficient to guarantee single-frequency oscillations corresponding to the energy difference Δ in any observable, and thus to justify a two-level tunneling scenario. This point is represented schematically in Fig. 2.6 by the lines connecting the levels, the thickness of which corresponds to the magnitude of the matrix element $|\langle i|\hat{n}_z|j\rangle|$, where i and j denote energy levels. For fields corresponding to the center of a magnetization plateau, one observes by contrast that there is no clear two-level manifold, but that the matrix element of \hat{n}_z between the lowest pair of levels is dominant. This situation, $|\langle e|\hat{n}_z|g\rangle| \sim 1$, can be taken to express the requirement for a two-level description to be adequate for tunneling of the Néel vector.

Time Domain

There are in principle two ways of testing the coherent low-energy dynamics of a two-level system at low temperatures. The first would be to prepare the

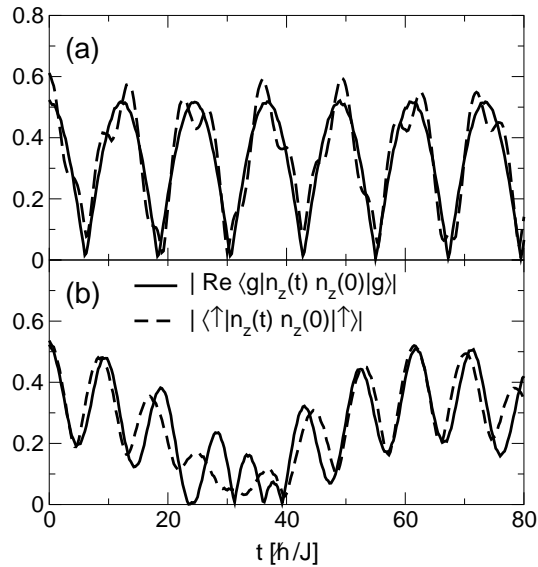


Figure 2.7: The Néel vector correlation function $\langle \hat{n}_z(t) \hat{n}_z(0) \rangle$ for Na:Fe₆ in magnetic fields (a) $g\mu_B B_x = 3.1J$ and (b) $g\mu_B B_x = 3.5J$. The frequency of the oscillation varies strongly with B_x because of the sinusoidal dependence of Δ on B_x in Eq. (2.21).

system in a non-eigenstate of the Hamiltonian, $|\uparrow\rangle = (|g\rangle + |e\rangle)/\sqrt{2}$, and then to observe coherent oscillations of the quantity of interest (here \hat{n}_z) in the time domain. The second is to measure ground-state correlation functions such as $\langle g|\hat{n}_z(t) \hat{n}_z(0)|g\rangle$ with a spectroscopic method. For an idealized tunneling scenario in which \hat{n}_z connects only $|g\rangle$ and $|e\rangle$, these two quantities contain the same information because

$$|\text{Re} \langle g|\hat{n}_z(t) \hat{n}_z(0)|g\rangle| \approx |\langle \uparrow|\hat{n}_z(t) \hat{n}_z(0)|\uparrow\rangle|. \quad (2.39)$$

In the tunneling limit where $|\langle g|\hat{n}_z|e\rangle| \sim 1$, $\langle g|\hat{n}_z(t) \hat{n}_z(0)|g\rangle = |\langle g|\hat{n}_z|e\rangle|^2 e^{i\Delta t/\hbar}$. The correlation functions obtained from exact diagonalization indeed show coherent oscillations with periods $h/\Delta = 24.5\hbar/J$ near the plateau center [Fig. 2.7(a)] and $h/\Delta = 132.0\hbar/J$ near the level crossing, where in addition a strong component of a higher harmonic is clearly evident [Fig. 2.7(b)]. The solid and dashed curves in Fig. 2.7, representing respectively the left- and right-hand sides of Eq. (2.39), do not coincide because of additional components present in the correlation function of $|\uparrow\rangle$ [right-hand side of (2.39)]. These indicate that $|e\rangle$ has significant matrix elements of \hat{n}_z with states other than $|g\rangle$ (Fig. 2.6). This is also expected from the semiclassical analysis in Sec. 2.2

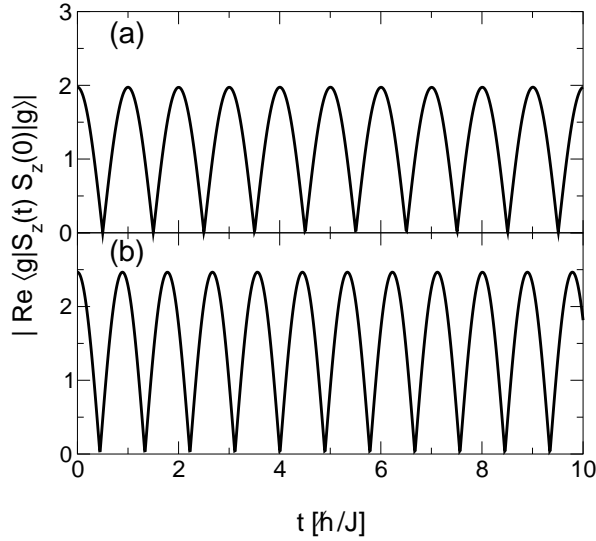


Figure 2.8: The total-spin correlation function $\langle \hat{S}_z(t) \hat{S}_z(0) \rangle$ for Na:Fe₆ in magnetic fields (a) $g\mu_B B_x = 3.1J$ and (b) $g\mu_B B_x = 3.5J$. The characteristic frequency is determined by the Zeeman energy, $g\mu_B B_x$.

because the mapping of Na:Fe₆ onto a two-level system is marginal because of the small tunnel action $\mathcal{S}_0/\hbar = 2.47$.

In stark contrast to $\langle \hat{n}_z(t) \hat{n}_z(0) \rangle$, the total-spin correlation function $\langle \hat{S}_z(t) \hat{S}_z(0) \rangle$ (Fig. 2.8) shows oscillations only at the much higher frequency h_x , as expected from Eq. (A.8) and the symmetry considerations presented in Sec. 2.2.2. These field-driven oscillations do not correspond to a quantum tunneling process.

Spectra and Matrix Elements

The correlation functions shown above may be understood directly from the matrix elements between the lowest-lying energy levels for the components of the total-spin and Néel-vector operators. The symbols in Fig. 2.9 show the numerical results for energy-level splittings and matrix elements of \hat{n}_z in the low-energy manifold of Na:Fe₆. The energy separations Δ_i [Fig. 2.9(a)] confirm that an appreciable separation remains between the lowest pair of states and the next higher level for all fields. That this criterion alone is not sufficient to assess the quality of a two-level description is shown by the matrix elements in Fig. 2.9(b). While $|\langle e | \hat{n}_z | g \rangle|$ is indeed large for all fields, the matrix element $|\langle 2 | \hat{n}_z | g \rangle|$ is also significant at fields close to the level crossings. Here, $|2\rangle$ denotes the second

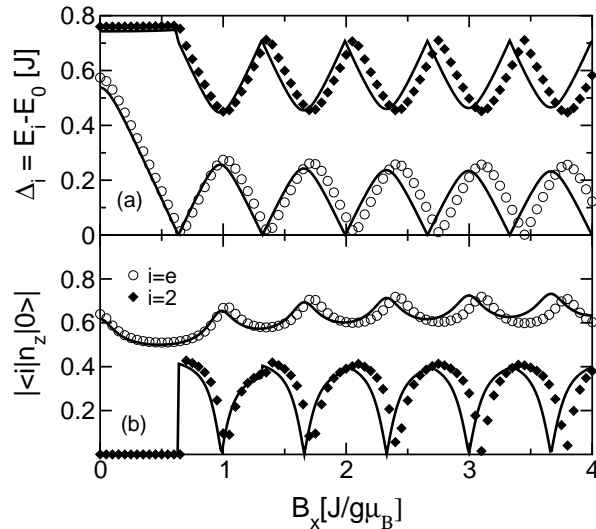


Figure 2.9: Evolution with magnetic field of (a) the energy-level splittings Δ_i and (b) the matrix elements $|\langle i|\hat{n}_z|g\rangle|$ for the low-energy sector ($i = 1, 2$) in Na:Fe₆. Exact diagonalization results (symbols) are compared with the rigid rotor approximation (lines).

excited state. In fact at the plateau centers $|\langle 2|\hat{n}_z|g\rangle|$ vanishes identically, and in this field regime $|\langle e|\hat{n}_z|g\rangle|$ is considerably larger than $|\langle i|\hat{n}_z|g\rangle|$ for all $i \geq 2$.

Our exact diagonalization calculations confirm that the semiclassical picture of Néel vector tunneling between directions $+\mathbf{e}_z$ to $-\mathbf{e}_z$ is indeed appropriate here. At the level-crossing fields more of the higher matrix elements of \hat{n}_z are appreciable [Fig. 2(b)], and in particular $|\langle 2|\hat{n}_z|g\rangle|$ has 66.0% of the magnitude of $|\langle e|\hat{n}_z|g\rangle|$. In the semiclassical description this corresponds to the Néel vector being rather less well localized along $\pm\mathbf{e}_z$ than for fields at the plateau centers. The effects of the higher matrix elements with $|g\rangle$ [Fig. 2.9(b)] are evident in the solid lines in Figs. 2.7(a) and (b): High frequency components are superimposed on the dominant slow dynamics of the Néel vector which reflects the quantum tunneling. These fast oscillations correspond to the oscillations of the Néel vector in each of the potential wells rather than the tunneling between the potential wells.

Fig. 2.10(a) shows the spectrum of Na:Fe₆ as a function of magnetic field, expanded to splittings $\Delta_i = 5.5J$, which illustrates both the anticrossing between the second and third levels, and the presence of a linearly evolving Zeeman-split level at $\Delta_i \approx \hbar h_x$. The total-spin matrix elements in Fig. 2.10(b) show the two primary features expected on symmetry grounds. The matrix element

in the low-energy sector vanishes, $\langle e|\hat{S}_z|g\rangle = 0$, and the dominant matrix element appears at the Zeeman splitting. This situation remains very close to the $k_z = 0$ limit, where the field-driven Zeeman transition is the only process with a non-vanishing matrix element, $|\langle i|\hat{S}_z|g\rangle| = \sqrt{S(h_x)/2}$, in which $S(h_x)$ denotes the spin of the ground state at field B_x and $|i\rangle$ is the energy eigenstate with $E_i - E_g \simeq \hbar h_x$.

Rigid-Rotor Model

Further insight may be gained into the nature of our exact results by comparison with those from semiclassical approaches (Sec. 2.2), which specify the conditions for the two-level system to provide an appropriate description of the low-energy spectrum of Eq. (2.14). Under the assumptions that the spins in the ferric wheel have alternating (Néel) alignment and that magnon excitations may be neglected, \hat{H}_0 can be mapped to the Hamiltonian of a rigid rotor (RR) [65],

$$\hat{H}_{\text{RR}} = \frac{2J}{N}\hat{\mathbf{L}}^2 + \hbar\mathbf{h} \cdot \hat{\mathbf{L}} - Nk_z s^2 \hat{n}_z^2, \quad (2.40)$$

where $\hat{\mathbf{n}}$ and $\hat{\mathbf{L}}$ are respectively the position and angular momentum of a particle confined to the unit sphere. Equation (2.40) follows from the Lagrangean, Eq. (2.16), by a canonical transformation. The operator for total spin is represented by the angular momentum of the particle, $\hat{\mathbf{S}} = \hat{\mathbf{L}}$, the eigenstates of which, $|l, m\rangle$, are spherical harmonics. The term $-Nk_z s^2 \hat{n}_z^2$ accounts for the anisotropy potential which renders energetically favorable those spin configurations for which the Néel vector \mathbf{n} is aligned with $\pm\mathbf{e}_z$. For small k_z , the eigenstates of Eq. (2.40) have almost uniform probability distribution of \mathbf{n} in the plane perpendicular to the magnetic field, which corresponds to the kinetic limit of \hat{H}_{RR} . The opposite limit of large k_z is specified by the condition that the tunnel action $\mathcal{S}_0/\hbar = Ns\sqrt{2k_z/J}$ be very much greater than 1, and it is here that a two-level description of quantum tunneling of the staggered magnetization is appropriate.

The condition $\mathcal{S}_0/\hbar > 1$ may be taken to mark the onset of a spin quantum tunneling regime, in which there is only one pair of tunnel-split states in the low-energy sector. In this respect a two-level approximation is marginal for the real AFMR's, although it should be rather better defined for Cs:Fe₈ ($\mathcal{S}_0/\hbar = 3.8$) and Fe₁₀ ($\mathcal{S}_0/\hbar = 3.3$) than for Na:Fe₆ ($\mathcal{S}_0/\hbar = 2.5$). In this regime of intermediate k_z/J the rigid rotor framework remains applicable because no weak tunneling is assumed in deriving Eq. (2.40), but the anisotropy energy $-Nk_z s^2 \hat{n}_z^2$, which may not be treated perturbatively, gives rise to significant mixing of states of differing angular momentum l . A quantitative comparison of rigid rotor results with exact diagonalization then requires exact diagonalization of Eq. (2.40). This is most easily performed in the basis $|l, m\rangle$ in which $\hat{\mathbf{L}}$ is diagonal, and

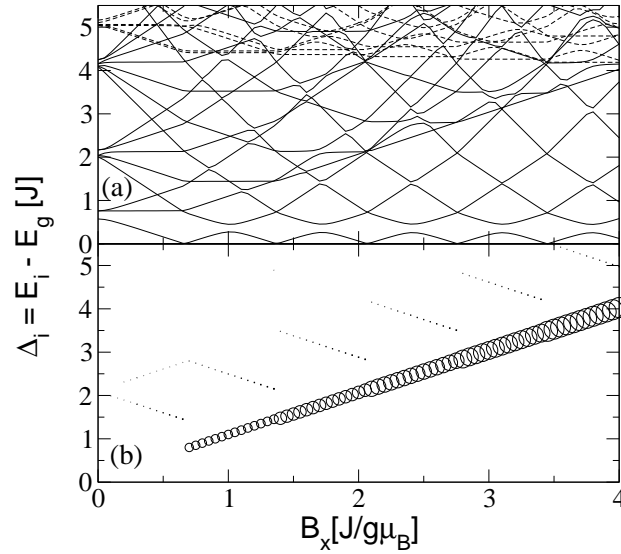


Figure 2.10: (a) Evolution with magnetic field of energy spectra for Na:Fe₆ up to $\Delta_i = 5.5J$. The solid lines represent exact diagonalization data in the momentum sectors $p = 0$ and $p = \pi$ (in both cases, only states with positive site parity appear in the energy range of the figure), while the dashed lines correspond to momenta $p = \pi/3$ and $p = 2\pi/3$ which are absent in the rigid rotor model. Note the almost linearly Zeeman-split state at $\Delta_i \approx \hbar h_x$. (b) Matrix element $|\langle i | \hat{S}_z | g \rangle|$ as a function of magnetic field, represented by radius of open circles. The dominant matrix element corresponds to the level with $\Delta_i \approx \hbar h_x$ for $\hbar h_x \geq 0.7J$, while for the same field range the next-largest elements correspond to still higher excited levels.

the matrix elements $\langle l', m' | \hat{n}_z^2 | l, m \rangle$ are evaluated in spherical coordinates. For moderate fields, the unphysical states of large angular momenta ($l > 15$) may be neglected in the rigid rotor approach, and the dimension of the Hilbert space is then reduced very significantly over that of the full Hamiltonian (256 compared to 46656 for Fe₆).

Comparisons between exact diagonalization of the rigid rotor model (2.40) and the exact numerical results are shown in Fig. 2.9. There is rather good general agreement in the low-energy sector, especially in magnitudes of Δ_i and $|\langle i | \hat{n}_z | g \rangle|$, but also a drift in field of the predicted magnetization step positions from the exact result [67, 68, 69]. This is thought to be largely a consequence of neglecting magnon excitations, by which is meant spin misalignments within each of the sublattices, and can be removed by a uniform rescaling (with a factor

of 1.036 for the parameters of Na:Fe₆). The rigid rotor model is not expected to perform as well at higher energies, a statement which can be quantified by inspection of the exact spectra shown in Fig. 2.10(a), where energy levels corresponding to the momentum sectors $p = \pi/3$ and $2\pi/3$ appear at $\Delta_i > 4J$. These momentum sectors are not contained in the rigid rotor description in which spatial fluctuations of the Néel vector have been neglected. However, the rigid rotor prediction of the total-spin matrix elements shown in Fig. 2.10(b) remains quite accurate for the energies shown, including the qualitative result that no matrix elements of the total-spin components connect $|g\rangle$ and $|e\rangle$ and the quantitative result for the ground-state spin $S(h_x) \sim \lfloor N\hbar h_x/4J \rfloor$ appearing in the only large matrix element $|\langle i|\hat{S}_z|g\rangle| \approx \sqrt{S(h_x)/2}$ at $\Delta_i \approx h_x$. We may summarize by remarking that, for $\mathcal{S}_0/\hbar > 1$, the two-level paradigm [Eq. (2.24)] delivers a simple conceptual picture of the low-energy spin dynamics in terms of coherent tunneling of the staggered magnetization, and that in addition the semiclassical treatment based on exact diagonalization of the rigid rotor approximation provides semi-quantitative accuracy for the physical parameters of the real materials.

2.3.2 Cs:Fe₈

We turn briefly to the 8-membered ferric wheel Cs:Fe₈. The effective uniaxial anisotropy which may be extracted from the magnetization data for this material [58] is considerably stronger than in the case of Na:Fe₆ presented above. Numerically, dynamical simulations remain possible for this system, despite the much larger Hilbert space. Figure 2.11 shows the energy spectrum for a Cs:Fe₈ system, again described by Eq. (2.14), with the anisotropy ratio deduced [61] from the angle-dependence of the first critical field [58] to be $k_z/J = 0.0185$. The situation remains qualitatively similar to Na:Fe₆, but has visible differences as a result of the larger values of N and k_z/J . The stronger coupling between eigenstates $|l, m\rangle$ results in a stronger anticrossing of levels $|e\rangle$ and $|2\rangle$ at the plateau centers and a smaller maximal Δ . This enhanced separation of the two-state manifold at lowest energies, combined with an increased tunnel barrier, makes the semiclassical tunneling description more appropriate, as expected from the larger value of \mathcal{S}_0/\hbar . Although in Fig. 2.11 we show only the results of full diagonalization, we have verified that, as in the case of Na:Fe₆, the rigid rotor model again provides qualitatively similar results, albeit with a larger drift in the level-crossing fields.

Figure 2.12 shows the Néel vector correlation function for the system in two magnetic fields chosen close to a plateau center and to a plateau edge. We observe rather clean, single-component temporal oscillations near the center of the magnetization plateau [Fig. 2.12(a)], where the admixture of higher frequencies is indeed weak. Near the level crossing [Fig. 2.12(b)] the second-largest matrix

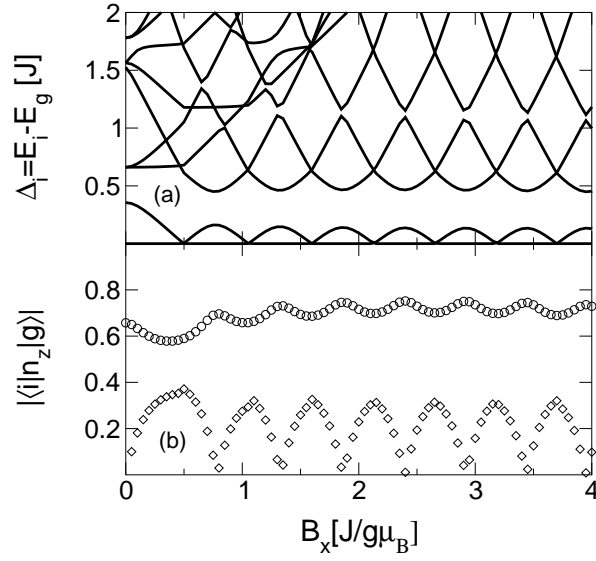


Figure 2.11: Evolution with magnetic field of (a) energy-level splittings Δ_i and (b) matrix elements $|\langle i|\hat{n}_z|g\rangle|$ for the low-energy sector in Cs:Fe₈. In (b), the circles correspond to $|i\rangle = |e\rangle$ and diamonds to higher excited states $i \geq 2$.

element, $|\langle 2|\hat{n}_z|g\rangle|$, has 43.4% of the magnitude of $|\langle e|\hat{n}_z|g\rangle|$. However, the large separation in frequency scales results in clearly visible contributions from both components, and thus to pronounced low-frequency oscillations in $\langle \hat{n}_z(t)\hat{n}_z(0)\rangle$ corresponding to coherent Néel vector tunneling in Fig. 2.12(b).

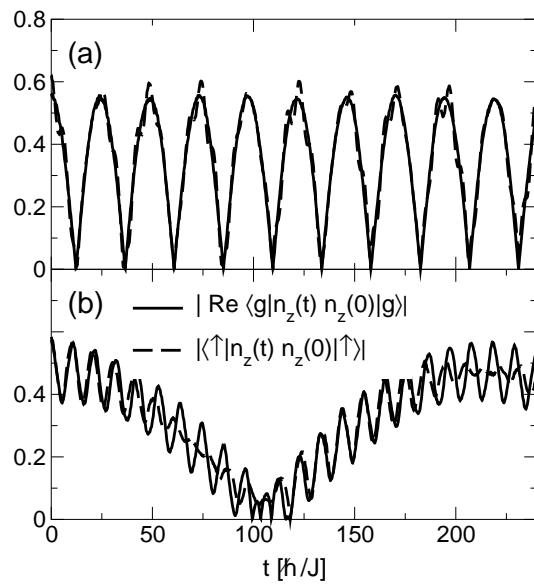


Figure 2.12: The Néel vector correlation function $\langle \hat{n}_z(t) \hat{n}_z(0) \rangle$ for Cs:Fe₈ in magnetic fields (a) $g\mu_B B_x = 3.4J$ and (b) $g\mu_B B_x = 3.72J$.

Chapter 3

Detecting macroscopic quantum coherence in antiferromagnetic molecular rings

As shown in Sec. 2.2, antiferromagnetic molecular rings (AFMR's) are promising candidates for macroscopic quantum coherence in the form of tunneling of the Néel vector. Detection of the Néel vector tunneling requires probes that couple only to single spins of the ring because the total spin of the AFMR remains invariant on tunneling of the Néel vector. In the following we show that both nuclear magnetic resonance (Sec. 3.1) and electron spin resonance in doped rings (Sec. 3.2) are adequate experimental techniques for the observation of Néel vector quantum tunneling [44, 45].

3.1 Nuclear magnetic resonance

A nuclear spin $\hat{\mathbf{I}}$ coupled only to a single electron spin of the antiferromagnetic ring is a natural candidate for a local probe, as indicated in [70] for a bulk antiferromagnetic system. We show that in small AFMR's in which the Néel vector \mathbf{n} itself has additional coherent dynamics, the correlation functions of the nuclear spin exhibit signatures of the tunneling of \mathbf{n} . In particular, we discuss the coherent dynamics of one nuclear spin coupled to one of the electron spins of the AFMR and show that both the tunnel splitting Δ and the electron spin decoherence rate can be obtained from nuclear magnetic resonance (NMR) and electron spin resonance (ESR) spectra.

3.1.1 Nuclear susceptibilities

NMR techniques have been widely used to study molecular magnets [64, 71, 72, 73, 74]. For simplicity, we restrict our considerations to interactions of the form $\hat{H}' = A\hat{\mathbf{s}}_1 \cdot \hat{\mathbf{I}}$, which includes both the hyperfine contact interaction and the direction-independent part of the magnetic dipolar interaction. Our theoretical framework will be illustrated for the ferric wheel Fe_{10} . For the NMR active nucleus ^{57}Fe , the dominant coupling to the electron spin is by a hyperfine contact interaction, $A_{\text{Fe}}s \simeq 3.3\text{mK}k_B$ [75]. In contrast, the interaction of a ^1H nuclear spin with the electron spins is dipolar, with a direction-independent term $\sum_i A_i \hat{\mathbf{s}}_i \cdot \hat{\mathbf{I}}$. For antiferromagnetic order, the sum yields an effective coupling $A_H s \hat{\mathbf{n}} \cdot \hat{\mathbf{I}}$, where, for Fe_{10} , the coefficient $A_H = \sum_i (-1)^{i+1} A_i$ depends strongly on the site of the proton spin $\hat{\mathbf{I}}$. For many of the inequivalent sites, however, A_H is of order $0.1\text{mK}k_B$ [74]. With N_{Fe} and N_{H} the numbers of NMR-active ^{57}Fe and proton nuclei, as long as $N_{\text{Fe}}A_{\text{Fe}} + N_{\text{H}}A_H \ll \Delta$, the effect of the nuclear spins on the electron spin dynamics remains small. In particular, the hyperfine field of the the nuclear spins is too small to give rise to a substantial energy bias between different Néel ordered spin configurations that would suppress quantum tunneling of \mathbf{n} . We define the decoherence rates Γ_I and Γ_{dec} of the nuclear and electronic spins as the decay rates of the oscillations with $\omega = \gamma_I B_x / \hbar$ in $\langle \hat{I}_y(t) \hat{I}_y \rangle$ and $\omega = \Delta / \hbar$ in $\langle \hat{n}_z(t) \hat{n}_z \rangle$, respectively. For time scales $t < 1/\Gamma_{\text{dec}}$, the electron spin produces a coherently oscillating effective magnetic field with frequency Δ/\hbar at the site of the nucleus.

In order to show that this field affects the nuclear spin dynamics, we now consider a single, NMR-active ^{57}Fe or ^1H nucleus (inset of Fig. 3.2). For $k_B T \ll \hbar\omega_0$, we may restrict our considerations to the Hilbert space spanned by the tunnel-split states $\{|g\rangle, |e\rangle\}$ of the AFMR [Eq. (2.24)]. By using the decomposition $\mathbf{s}_i = (-1)^{i+1} s \mathbf{n} + \mathbf{l}$ of a single spin into staggered magnetization $\pm s \mathbf{n}$, $\mathbf{n}^2 = 1$, and fluctuations $\mathbf{l} \perp \mathbf{n}$ around the Néel ordered state, we obtain $\hat{H}' = A\hat{\mathbf{s}}_1 \cdot \hat{\mathbf{I}} \simeq A s \hat{\mathbf{n}} \cdot \hat{\mathbf{I}}$. We show now that, due to $\langle e | \hat{n}_z | g \rangle \neq 0$, the tunneling dynamics of \mathbf{n} can be obtained from the nuclear spin correlation functions $\langle \hat{I}_\alpha(t) \hat{I}_\alpha \rangle$. With $\langle e | \hat{n}_z | g \rangle = \mathcal{O}(1)$, the dominant term in \hat{H}' is $A s \hat{n}_z \hat{I}_z$, and we approximate the hyperfine coupling

$$\hat{H}' \simeq A s \hat{n}_z \hat{I}_z. \quad (3.1)$$

NMR experiments measure via power absorption the imaginary part of the nuclear spin susceptibility, $\chi''_{I,\alpha\alpha}(\omega)$, and by pulsed techniques the nuclear spin correlation functions $\langle \hat{I}_\alpha(t) \hat{I}_\alpha \rangle$ in the time domain [76]. From expanding $\langle \hat{I}_\alpha(t) \hat{I}_\alpha \rangle$

in \hat{H}' ,

$$\begin{aligned} \langle \hat{I}_\alpha(t) \hat{I}_\alpha \rangle &\simeq \langle \hat{I}_\alpha(t) \hat{I}_\alpha \rangle_0 - A^2 s^2 / \hbar^2 \int_{-\infty}^t dt' \int_{-\infty}^0 dt'' \\ &\times \langle [\hat{I}_z(t'), \hat{I}_\alpha(t)] [\hat{I}_z(t''), \hat{I}_\alpha] \rangle_0 \langle \hat{n}_z(t') \hat{n}_z(t'') \rangle_0, \end{aligned} \quad (3.2)$$

it is evident that the dynamics of \mathbf{n} enters $\chi''_{I,\alpha\alpha}(\omega)$. Here, the subscript 0 denotes the thermal average for the system in which electron and nuclear spins are uncoupled, $A = 0$.

To evaluate Eq. (3.2), we diagonalize the Hamiltonian

$$\hat{H} = -\frac{\Delta}{2} (|g\rangle\langle g| - |e\rangle\langle e|) - \gamma_I B_x \hat{I}_x + A s \hat{I}_z \hat{n}_z, \quad (3.3)$$

with γ_I the nuclear gyromagnetic ratio, which describes the ferric wheel in the low-energy sector with a single nuclear spin $\hat{\mathbf{I}}$ coupled to $\hat{\mathbf{s}}_1$, Eq. (3.1). We assume thermal equilibrium for both electron and nuclear spins. For Fe₁₀ and the other AFMR's in the high field regime, the results may be derived by expansion to leading order in As/Δ and $\gamma_I B_x/\Delta$, because $\Delta_0 \gg \gamma_I B_x, As$, for both ⁵⁷Fe and ¹H nuclei, and $B_x \simeq 10$ T. For a nuclear spin $I = 1/2$, $\chi''_{I,zz}(\omega)$ displays the unperturbed emission and absorption peaks at $\omega \simeq \pm \gamma_I B_x/\hbar$, although these are slightly shifted if the hyperfine term $A\mathbf{I} \cdot \mathbf{I}$ is taken into account. $\chi''_{I,xx}(\omega)$, however, displays resonant absorption and emission of small intensity at $\omega = \pm(\Delta \pm \gamma_I B_x)/\hbar$. Finally, the nuclear susceptibility

$$\begin{aligned} \chi''_{I,yy}(\omega) &= \frac{\pi}{4} \left[\tanh\left(\frac{\beta\gamma_I B_x}{2}\right) \delta(\omega - \gamma_I B_x/\hbar) \right. \\ &\quad \left. + \left(\frac{As}{\Delta}\right)^2 \tanh\left(\frac{\beta\Delta}{2}\right) \delta(\omega - \Delta/\hbar) \right] - [\omega \rightarrow -\omega] \end{aligned} \quad (3.4)$$

exhibits *satellite resonances at the tunnel splitting Δ of the electron spin system*.

Their physical origin is readily understood in terms of a classical vector model (see Fig. 3.1). For $A = 0$, $\mathbf{I}(t)$ precesses around the static magnetic field $\mathbf{B} = B_x \mathbf{e}_x$. For $A \neq 0$, the coherent tunneling of \mathbf{n} leads to an oscillating hyperfine field $As_1(t) \simeq As \cos(\Delta t/\hbar) \mathbf{e}_z$ at the site of the nucleus. In contrast to a static hyperfine field which induces a change in precession frequency and axis for \mathbf{I} , the rapidly oscillating hyperfine field in the AFMR leads only to a small deviation $\delta\mathbf{I}(t) = \mathcal{O}(As/\Delta)$ from the original precession. In particular, $\delta I_y(t) \propto (As/\Delta) \sin(\Delta t/\hbar)$ also oscillates at frequency Δ/\hbar and, hence, gives rise to the second term in Eq. (3.4).

On a technical level, the simplest way to derive Eq. (3.4) is to apply perturbation theory in \hat{H}' in the truncated Hilbert space spanned by the ground state doublet $\{|g\rangle, |e\rangle\}$ of the AFMR and the \hat{I}_x eigenstates of the nuclear spin, $\{|\uparrow_x$

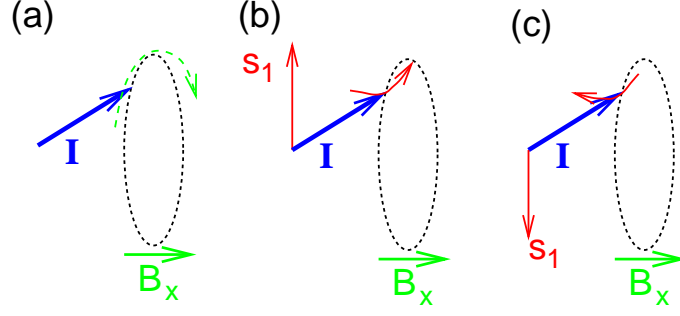


Figure 3.1: (a) In absence of a hyperfine coupling, the nuclear spin \mathbf{I} precesses around the external magnetic field. (b) and (c) For $A \neq 0$, a precession around the hyperfine field $A\mathbf{s}_1$ is superimposed on the precession around the magnetic field. For a tunneling electron spin which reverses its direction at a rate Δ/h , the typical timescale of the precession of \mathbf{I} around the hyperfine field is h/Δ .

$\rangle, |\downarrow_x\rangle\}$. For vanishing hyperfine coupling, $A = 0$, $\{|g \downarrow_x\rangle, |e \uparrow_x\rangle, |g \uparrow_x\rangle, |e \downarrow_x\rangle\}$ are energy eigenstates with eigenenergies $\{(-\Delta + \gamma_I B_x)/2, (\Delta - \gamma_I B_x)/2, (-\Delta - \gamma_I B_x)/2, (\Delta + \gamma_I B_x)/2\}$, respectively. To first order in perturbation theory in \hat{H}' , for $\Delta \gg \gamma_I B_x, As$, one obtains the eigenstates

$$\begin{aligned}
 |1\rangle &\simeq |g \downarrow_x\rangle - \frac{As}{2\Delta} |e \uparrow_x\rangle, \\
 |2\rangle &\simeq |e \uparrow_x\rangle + \frac{As}{2\Delta} |g \downarrow_x\rangle, \\
 |3\rangle &\simeq |g \uparrow_x\rangle - \frac{As}{2\Delta} |e \downarrow_x\rangle, \\
 |4\rangle &\simeq |e \downarrow_x\rangle + \frac{As}{2\Delta} |g \uparrow_x\rangle
 \end{aligned} \tag{3.5}$$

with eigenenergies

$$E_{1,3} = -\frac{\Delta}{2} \pm \frac{\gamma_I B_x}{2}, \quad E_{2,4} = \frac{\Delta}{2} \mp \frac{\gamma_I B_x}{2}, \tag{3.6}$$

which remain unchanged to first order in As/Δ . The expansion in Eq. (3.5) shows that perturbation theory in \hat{H}' remains valid as long as $As \ll \Delta$. The spectral representation for the nuclear susceptibility is [76]

$$\begin{aligned}
 \chi''_{I,yy}(\omega) &= \pi \sum_{i>j} (p_i - p_j) |\langle i | \hat{I}_y | j \rangle|^2 [\delta(\omega - (E_i - E_j)/\hbar) \\
 &\quad - \delta(\omega + (E_i - E_j)/\hbar)], \tag{3.7}
 \end{aligned}$$

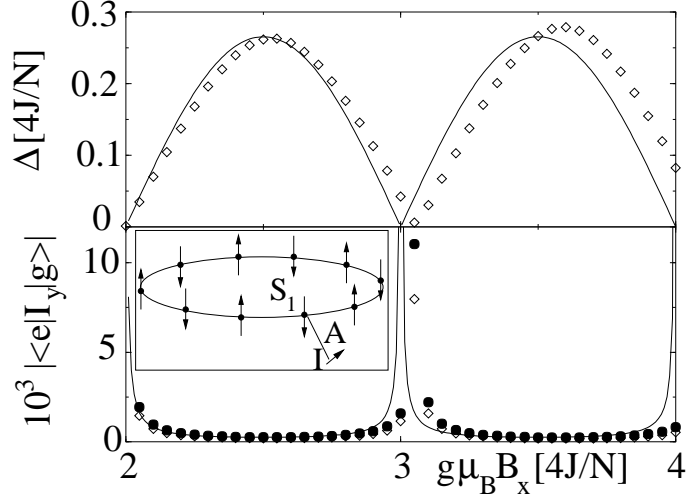


Figure 3.2: Comparison of the analytical result for Δ (upper panel) and $|\langle e|\hat{I}_y|g\rangle|$ (lower panel) with exact numerical results for a small system, $N = 4$, $s = 3/2$, $k_z = 0.2J$, and $A = 9 \times 10^{-5}J$. The numerical values (\diamond) for $|\langle e|\hat{I}_y|g\rangle|$ are well approximated by $As/2\Delta$ (solid line), with a small offset in B_x resulting from the shift of the magnetization steps when $k_z \neq 0$. For reference, the ratios $As/2\Delta$ with the numerical values for Δ are shown (\bullet) in the lower panel.

where p_i is the equilibrium probability for the system to be in state $|i\rangle$ and $i, j = 1, 2, 3, 4$. Only the matrix elements $|\langle 3|\hat{I}_y|1\rangle| = |\langle 4|\hat{I}_y|2\rangle| = 1/2$ and $|\langle 4|\hat{I}_y|1\rangle| = |\langle 3|\hat{I}_y|2\rangle| = As/2\Delta$ are finite, which directly proves Eq. (3.4).

We restricted the above analysis to the low-energy sector of the ferric wheel. To check this approximation, we have performed exact numerical diagonalization on a small antiferromagnetic ring with one nuclear spin of $I = 1/2$ coupled to one of the electron spins. For the small systems accessible by exact diagonalization, in this case $N = 4$, $s = 3/2$, and $k_z = 0.2J$, the field range for which the theoretical framework is applicable becomes rather small: $2J \ll \hbar h_x \ll 6J$. However, the numerical results (Fig. 3.2) for $\langle e|\hat{I}_y|g\rangle$ indicate that our analytical value $|\langle e|\hat{I}_y|g\rangle| = As/2\Delta$ entering Eq. (3.4) is a good approximation. Here, $|\langle e|\hat{I}_y|g\rangle|$ is shorthand for the matrix elements $|\langle 4|\hat{I}_y|1\rangle| = |\langle 3|\hat{I}_y|2\rangle|$ introduced above. For our parameters, the analytical value tends to overestimate $\langle e|\hat{I}_y|g\rangle$ by $\sim 30\%$ because, in reality, the matrix element $|\langle e|\hat{n}_z|g\rangle|$ is smaller than unity because of quantum fluctuations of the Néel vector around the potential minima.

3.1.2 Experimental realization

We turn next to a discussion of the experimental feasibility of measuring Δ by NMR. Because $As/\Delta \ll 1$, the intensity of the satellite peaks at $\omega = \pm\Delta/\hbar$ [Eq. (3.4)] is small compared to that of the main peaks at $\omega = \pm\gamma_I B_x/\hbar$. However, this satellite peak intensity may be increased significantly by tuning B_x close to one of the critical values B_x^c at which the magnetization of the AFMR jumps and $\Delta(B_x = B_x^c) = 0$. Note, however, that our theory only applies to high magnetic fields, $B_x > 7.7\text{T}$ for Fe_{10} .

Coherent tunneling of the Néel vector \mathbf{n} requires $\Delta \gtrsim \hbar\Gamma_{\text{dec}}$. An estimate of Γ_{dec} can be obtained from the typical energy scales of various interactions that lead to decoherence. Spin-phonon interactions are frozen out at low T . Nuclear dipolar ($0.1\text{mK}k_B$) and hyperfine ($1\text{mK}k_B$) interactions are significantly smaller than interring electron spin dipolar interactions (some $10\text{mK}k_B$). These numbers indicate that, in Fe_{10} , tunneling of \mathbf{n} is expected to be coherent for a wide range of $\Delta \ll \Delta_0$, where $\Delta_0 \simeq 2.18\text{K}k_B$ is the maximum tunnel splitting.

We consider first ^{57}Fe , with $\gamma_I = 0.18\mu_N$ [75]. For $T \simeq 2\text{K}$ and $B_x \sim 10\text{T}$, the relative intensity of the satellite peak at $\Delta = \Delta_0 = 2.18\text{K}k_B$ compared to the resonance at $\gamma_I B_x$ is $(As/\Delta)^2 \tanh(\beta\Delta/2)/\tanh(\beta\gamma_I B_x/2) \simeq 0.007$. This intensity, however, increases by a factor of 10 (100) for $\Delta = 0.1\Delta_0$ ($\Delta = 0.01\Delta_0$). For ^1H with $\gamma_I = 5.59\mu_N$ [75], and a typical value $As \simeq 0.1\text{mK}k_B$, the relative peak intensity is 2.05×10^{-7} ($\Delta = \Delta_0$), 2.25×10^{-6} ($\Delta = 0.1\Delta_0$), and 2.25×10^{-5} ($\Delta = 0.01\Delta_0$). However, the number of protons in the ring is much larger than that of NMR-active ^{57}Fe nuclei, $10 \lesssim N_{\text{H}}/N_{\text{Fe}} \lesssim 100$, depending on the doping with ^{57}Fe . Taking into account that the sensitivity of proton NMR is larger than that of Fe NMR by a factor of 3×10^4 [75], ^{57}Fe and proton NMR appear to be similarly appropriate for detecting the coherent tunneling of \mathbf{n} . The observation of the satellite peak in Eq. (3.4) is feasible, but still remains a challenging experimental task. The experiment must be conducted with single crystals of Fe_{10} (or a Fe_6 system with sufficiently large $k_z > 2J/(Ns)^2$) at high, tunable fields (10T) and low temperatures (2K). Moreover, because the field B_x at which Δ vanishes depends sensitively on the relative orientation of \mathbf{B} and the easy axis [60, 61], careful field sweeps are necessary to ensure that $\Delta/\Delta_0 \ll 1$ is maintained. Note that the NMR experiment suggested here could be more easily realized with nuclear spins exhibiting higher NMR sensitivity than ^{57}Fe .

We show now that, from NMR spectra, also an upper bound for Γ_{dec} can be extracted. The NMR resonance lines are broadened by the decoherence of the nuclear spin, with width Γ_I at $\pm\gamma_I B_x/\hbar$. The NMR resonances at $\omega = \pm\Delta/\hbar$ also involve correlation functions of \mathbf{n} , see (3.2). Thus the decoherence of the electron spin, Γ_{dec} , adds to the linewidth, and the width of the satellite peak, δ , is bounded by $\Gamma_I + \Gamma_{\text{dec}} < \delta$. Measurement of δ then provides an upper bound for Γ_{dec} , the decoherence rate of Néel vector tunneling. Further, $\hbar\Gamma_{\text{dec}} \simeq \Delta$

marks the transition from coherent to incoherent tunneling dynamics. Hence, if $\delta < \Delta/\hbar$ this would indicate unambiguously that quantum tunneling of the Néel vector is coherent. Note that the maximum peak height of a Lorentzian resonance line is $\mathcal{O}(1/\delta)$, so a large $\Gamma_{\text{dec}} (< \Delta/\hbar)$ would make detection of the satellite peak increasingly difficult.

3.1.3 ESR measurements in presence of hyperfine interactions

We show now that, in the presence of a hyperfine coupling \hat{H}' , the electron spin susceptibility of the ring, $\chi_{\alpha\alpha}(\omega)$, also exhibits signatures of a coherent tunneling of \mathbf{n} . This results from the fact that integration over the initial and final nuclear spin configurations causes the matrix elements $\langle e|\hat{\mathbf{S}}|g\rangle$ occurring in the spectral representation of $\chi_{\alpha\alpha}(\omega)$ [Eqs. (2.27) and (2.28)] to become finite. In the high field limit $h_x \gg \omega_0$, the matrix elements are

$$\begin{aligned} |\langle e|\hat{S}_y|g\rangle| &\simeq \frac{As}{2\hbar h_x} \frac{\Delta_0 \mathcal{S}}{4Nk_z s^2} |\cos(\pi N h_x/4J)|, \\ |\langle e|\hat{S}_z|g\rangle| &\simeq \frac{As}{2\hbar h_x}. \end{aligned} \quad (3.8)$$

For a small system ($N = 4$, $s = 3/2$), we have again confirmed the qualitative features of these results by exact diagonalization. It follows that $\chi''_{\alpha\alpha}(\omega \sim \Delta/\hbar) = \pi |\langle e|\hat{S}_\alpha|g\rangle|^2 \tanh(\beta\Delta/2)\delta(\omega - \Delta/\hbar)$ exhibits resonances at Δ/\hbar . Note that, in Eq. (3.8), the notation $|\langle e|\hat{S}_{y,z}|g\rangle|$ is, again, a schematic shorthand notation. More precisely, Eq. (3.8) specifies that, for $I_x = \pm 1/2$, to first order in perturbation theory in \hat{H}' ,

$$'\langle e, I_x|\hat{S}_z|g, I_x\rangle' = \frac{As}{2\hbar h_x}, \quad (3.9)$$

where

$$|g, I_x\rangle' = \left(1 + \frac{1}{-\Delta/2 + \gamma_I B_x I_x - \hat{H}_0} \hat{H}' \right) |g, I_x\rangle, \quad (3.10)$$

and similarly for $|e, I_x\rangle'$, is the energy eigenstates obtained in first order perturbation theory in \hat{H}' . In contrast to the matrix elements evaluated for the nuclear susceptibility, the first non-vanishing contribution in Eq. (3.8) requires to take into account energy eigenstates outside the ground state doublet of the AFMR.

A qualitative understanding of this result may be obtained in a classical vector model. A nuclear spin polarized along \mathbf{B} leads to an effective magnetic field $\mathbf{e}_x A/2g\mu_B$ acting only on \mathbf{s}_1 . In a classical description this hyperfine field

causes the total spin \mathbf{S} to acquire a component $\mathbf{n} As/2\hbar h_x$ along the Néel vector \mathbf{n} , and the coherent tunneling of \mathbf{n} now also results in an oscillation of the total spin \mathbf{S} . Again, the decoherence rate of these oscillations, and hence the linewidth of the ESR resonance, is bounded by Γ_{dec} . Note that $As/2\hbar h_x = 1.2 \times 10^{-4}$ for a single ^{57}Fe nucleus with $B_x = 10\text{T}$, so the ESR signal is very weak in this case.

However, our calculations apply to any impurity spin $\hat{\mathbf{j}}$, which interacts with a single electron spin only, $\hat{H}' = A\hat{\mathbf{s}}_1 \cdot \hat{\mathbf{j}}$. In particular, for an electronic $\hat{\mathbf{j}}$, A is typically 10^3 times larger than for a nuclear spin, and ESR techniques become a valuable tool for detecting the tunneling of the Néel vector. One advantage of this technique is that it is no longer necessary to have $\Delta/\Delta_0 \ll 1$ to obtain a large signal intensity, and thus the complete range of tunnel frequencies could be explored experimentally. Note that the experimentally accessible quantity is the susceptibility of the total spin $\hat{\mathbf{S}} + \hat{\mathbf{j}}$, with $\chi''_{\text{tot},\alpha\alpha}(\omega \sim \Delta/\hbar) = \pi |\langle e|\hat{S}_\alpha + \hat{j}_\alpha|g\rangle|^2 \tanh(\beta\Delta/2)\delta(\omega - \Delta/\hbar)$. As long as $As \ll \Delta$, $\langle e|\hat{j}_\alpha|g\rangle$ can be evaluated as for nuclear spins. Due to the different functional dependence of the matrix elements on h_x , the two contributions arising from $\hat{\mathbf{S}}$ and $\hat{\mathbf{j}}$ can be easily distinguished. Our calculations also apply to situations in which several impurity spins $\hat{\mathbf{j}}_i$ produce different net magnetic fields for the two sublattices of the AFMR. For illustration, we discuss two simple scenarios. We consider $N/2$ impurity spins $\hat{\mathbf{j}}_i$ ($j_i = 1/2$) coupled to $\hat{\mathbf{s}}_1, \hat{\mathbf{s}}_3, \dots$, $\hat{H}' = A \sum_{i=1}^{N/2} \hat{\mathbf{j}}_{2i-1} \cdot \hat{\mathbf{s}}_{2i-1}$. For $\hbar h_x \gg As, k_B T$, all $\hat{\mathbf{j}}_i$ align with the magnetic field \mathbf{B} . Since they all couple to one sublattice only, their net magnetic fields acting on $\hat{\mathbf{s}}_i$ add up, $|\langle e|\hat{S}_z|g\rangle| \simeq (N/2)As/2\hbar h_x$, leading to a $(N/2)^2$ -fold enhancement of the ESR-signal of a single impurity. In contrast, a single impurity $\hat{\mathbf{j}}$ coupled to both $\hat{\mathbf{s}}_1$ and $\hat{\mathbf{s}}_2$, $\hat{H}' = A\hat{\mathbf{j}} \cdot (\hat{\mathbf{s}}_1 + \hat{\mathbf{s}}_2)$, results in the same net magnetic field acting on both sublattices, and $\langle e|\hat{S}_z|g\rangle = 0$.

In conclusion, we have shown that NMR and ESR techniques can be used to measure both the tunnel splitting Δ and the decoherence rate Γ_{dec} in the AFMR. For Fe_{10} , we have shown that our proposal is within experimental reach. Our considerations apply to any AFMR described by \hat{H}_0 , Eq. (2.14), with some impurity spin coupled to one of the electron spins. Hence, the proposed schemes for detecting coherent Néel vector tunneling may prove useful for a wide class of molecular magnets.

3.2 Doped antiferromagnetic molecular rings

The reason for the experimental difficulties to detect Néel vector tunneling in AFMR's is that experimental probes such as magnetization and susceptibility measurements probe only the total spin of the molecule which, by symmetry,

remains unaltered upon tunneling of the Néel vector in the AFMR with translational invariance. If this symmetry is broken, e.g., by nuclear spins (Sec. 3.1), Néel vector tunneling gives rise to a resonance in the alternating current (AC) magnetic susceptibility of the total spin. Similarly, in ferrimagnets and antiferromagnets with uncompensated sublattice spins, in which Δ is still large, tunneling of \mathbf{n} leads to a signal in the AC susceptibility [24, 25, 26], provided that magnetic fields are small [11, 66, 77, 78]. Recent work [79] indicates that ferrimagnets exhibit a wealth of interesting tunnel scenarios also in finite magnetic fields.

Here, we study magnetic rings closely related to the AFMR's discussed in Sec. 2.2, the *modified AFMR's* in which one of the Fe^{3+} or Cr^{3+} ions has been replaced by an ion with spin s' to create an excess spin (Fig. 3.3). Various Cr_8 derivatives with this structure have been synthesized recently [80]. Starting from a microscopic model Hamiltonian,

$$\begin{aligned} \hat{H} = & J \sum_{i=2}^{N-1} \hat{\mathbf{s}}_i \cdot \hat{\mathbf{s}}_{i+1} + J'(\hat{\mathbf{s}}_1 \cdot \hat{\mathbf{s}}_2 + \hat{\mathbf{s}}_1 \cdot \hat{\mathbf{s}}_N) \\ & + \hbar \mathbf{h} \cdot \sum_{i=1}^N \hat{\mathbf{s}}_i - (k'_z \hat{s}_{1,z}^2 + k_z \sum_{i=2}^N \hat{s}_{i,z}^2), \end{aligned} \quad (3.11)$$

which also accounts for modified exchange coupling (J') and anisotropy (k'_z) constants due to doping, we calculate various thermodynamic quantities and spin correlation functions. In Eq. (3.11), $N = 10, 8,$ or 6 , $\mathbf{h} = g\mu_B \mathbf{B}/\hbar$, with \mathbf{B} the external magnetic field, and $g \simeq 2$ is the electron spin g factor. As we will show, the excess spin $\delta s = s' - s$ is strongly coupled to \mathbf{n} and hence is expected to modify both the thermodynamic properties and the spin dynamics of the AFMR. In contrast, for an impurity spin coupled weakly to the Néel vector (Sec. 3.2.3), the thermodynamic properties of the wheel remain essentially unaltered. For the modified AFMR's discussed here, Néel vector tunneling also leads to oscillations of the total spin which are observable in AC susceptibility or ESR measurements. Thermodynamic properties of antiferromagnetic systems with uncompensated sublattice spins have been studied in great detail for various anisotropy potentials and field configurations [81, 82]. One main advantage of the small, high-symmetry modified AFMR studied here is that the dependence of various thermodynamic quantities and spin correlation functions on the small number of microscopic parameters entering Eq. (3.11) can be evaluated analytically.

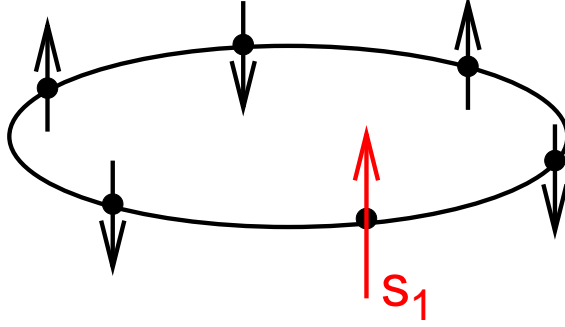


Figure 3.3: Schematic representation of the modified AFMR. The spin \mathbf{s}_1 of the original AFMR with spin quantum number s has been replaced by a spin with spin quantum number $s' \neq s$ in order to create an excess spin which traces the dynamics of the Néel vector.

3.2.1 A phenomenological model

In the modified AFMR's the symmetry of the sublattice Hamiltonian $\hat{H}_{0,\text{subl}}$ [Eq. (2.31)] under the exchange of the sublattices, $\hat{\mathbf{S}}_A \leftrightarrow \hat{\mathbf{S}}_B$, is broken. This makes them much more suitable for the observation of tunneling of \mathbf{n} . In this section we discuss the saddle-point, i.e., classical properties of the phenomenological sublattice model for the modified AFMR. We generalize earlier work [11, 66, 77, 78] to finite magnetic fields and show that, in contrast to systems with easy-plane anisotropy [79], in molecular rings with easy-axis anisotropy and finite excess spin, the total spin \mathbf{S} oscillates as \mathbf{n} tunnels.

Following Sec. 2.2.2, we introduce $\hat{\mathbf{S}}_A$ and $\hat{\mathbf{S}}_B$ as defined in Eq. (2.30). The Hamiltonian \hat{H} of the modified AFMR can thus be mapped onto a simpler version in terms of sublattice spins,

$$\begin{aligned} \hat{H}_{\text{subl}} = & \frac{4[(N-2)Js^2 + 2J's's']}{(Ns + 2\delta s)Ns} \hat{\mathbf{S}}_A \cdot \hat{\mathbf{S}}_B + \hbar \mathbf{h} \cdot (\hat{\mathbf{S}}_A + \hat{\mathbf{S}}_B) \\ & - \frac{2k_z}{N} \left[\frac{1 + 2(k'_z s'^2 - k_z s^2)/(Nk_z s^2)}{(1 + 2\delta s/Ns)^2} \hat{S}_{A,z}^2 + \hat{S}_{B,z}^2 \right], \end{aligned} \quad (3.12)$$

where $\delta s = s' - s$, $S_A = (N/2 - 1)s + s' = Ns/2 + \delta s$, and $S_B = Ns/2$. In the following, we assume the following inequalities:

$$|\delta s| \ll Ns, \quad (3.13)$$

$$|k'_z s'^2 - k_z s^2| \ll Nk_z s^2/2, Js, \quad (3.14)$$

$$2J's' \ll NJs, \quad (3.15)$$

where $J, J' > 0$. Equation (3.13) guarantees that the modified AFMR is an antiferromagnetic system with small excess spin, to which the theory of Néel vector tunneling applies. Both for Cr and Ga dopant ions ($|\delta s| = 1$ and $5/2$, respectively) in a ferric wheel, Eq. (3.13) is well satisfied. Equation (3.14) will allow us to treat the difference in sublattice anisotropies, $(k'_z s'^2 - k_z s^2)$, in perturbation theory. Typical values of k'_z and k_z are on the order of only $0.01J$, such that this condition holds for most systems of interest. Finally, Eq. (3.15) together with Eq. (3.13) assures that the ‘bulk’ parameters of an AFMR are only slightly altered by exchanging one single spin, such that the parameters of the undoped AFMR (Table 2.1) still determine whether the modified AFMR is in a quantum tunneling regime. However, as will be shown below, the excess spin $\delta s \neq 0$ leads to qualitative changes in both thermodynamic and dynamic quantities. We further assume

$$k_B T \ll \hbar \omega_0, \quad (3.16)$$

where $\omega_0 = s\sqrt{8Jk_z}/\hbar$, which allows us to restrict our attention to the low-energy sector of the AFMR, which consists of two tunnel-split states only.

We first discuss the classical vector model of Eq. (3.12) for $k_z = k'_z = 0$, but finite h_x . For an antiferromagnetic system with equal sublattice spins, the spins would lie close to the plane perpendicular to the field h_x . As sketched in Fig. 2.5, tilting of the spins leads to a gain in energy $N\hbar^2 h_x^2/8J$. However, for uncompensated sublattices, the configuration sketched in Fig. 3.4(a) provides an energy gain $|\delta s|\hbar h_x$ and hence is favorable for $\hbar h_x < |\delta s|8J/N = \hbar h_c$. Only for $h_x \gtrsim h_c$, the classical ground-state spin configuration is as sketched in Fig. 3.4(b). The energy is minimized if the projections of \mathbf{S}_A and \mathbf{S}_B onto the (y, z) -plane are antiparallel, such that $\mathbf{S} = \mathbf{S}_A + \mathbf{S}_B$ is parallel to \mathbf{B} . This picture remains valid for a system with easy-*plane* anisotropy and \mathbf{B} applied in the easy plane [79].

The scenario changes for easy-*axis* (\mathbf{e}_z) anisotropy and a magnetic field \mathbf{B} perpendicular to \mathbf{e}_z . Firstly, the anisotropy favors the spin configuration sketched in Fig. 3.4(b) over that in Fig. 3.4(a). The true classical ground-state spin configuration depends on the ratio $k_z/\hbar h_x$. More importantly, even for $h_x \gg h_c$, \mathbf{S} now has a component perpendicular to \mathbf{B} . The reason for this is that for $\delta s \neq 0$ or $k'_z s'^2 - k_z s^2 \neq 0$, Eq. (3.12) is no longer invariant under exchange of \mathbf{S}_A and \mathbf{S}_B if $k_z \neq 0$. Because of Eqs. (3.14) and (3.15), the components S_y and S_z of the total spin can be evaluated perturbatively. With the polar angle ϕ parameterizing the projection of \mathbf{S}_A onto the (y, z) -plane, to leading order in δs and $(k'_z s'^2 - k_z s^2)/2Js$ we obtain

$$\begin{pmatrix} S_y \\ S_z \end{pmatrix} \simeq \left(\delta s \frac{\omega_0^2}{\hbar^2} + \frac{k'_z s'^2 - k_z s^2}{2Js} \right) \sin^2 \phi \begin{pmatrix} \cos \phi \\ \sin \phi \end{pmatrix}. \quad (3.17)$$

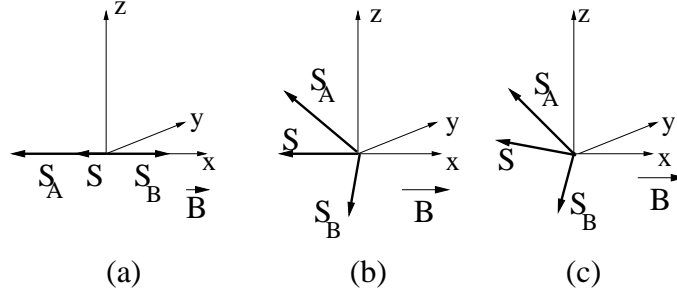


Figure 3.4: Classical ground-state spin configurations (schematically) of an antiferromagnetic system with excess spin in a magnetic field. (a) $k_z = k'_z = 0$ and $h_x < h_c = |\delta s|8J/N\hbar$. (b) $h_x > h_c$ and $k_z = k'_z = 0$. (c) $h_x > h_c$. Now, the finite anisotropies $k_z, k'_z \neq 0$ lead to a finite component S_z perpendicular to the magnetic field \mathbf{B} .

As is evident from Eq. (3.17), finite S_y or S_z can be caused by $\delta s \neq 0$ or $k'_z s'^2 - k_z s^2 \neq 0$, i.e., excess spin or unequal effective anisotropies for \mathbf{S}_A and \mathbf{S}_B .

According to Eq. (3.13), the modified AFMR is an antiferromagnetic system with small excess spin which is expected to exhibit spin tunneling dynamics qualitatively similar to the AFMR, as indicated by the close formal analogy between Eqs. (2.31) and (3.12). For magnetic fields

$$\max[\hbar\omega_0, |\delta s|8J/N] \ll \hbar h_x \ll 4Js, \quad (3.18)$$

the sublattice spin vectors \mathbf{S}_A and \mathbf{S}_B lie close to the (y, z) -plane. Due to the easy-axis anisotropy, configurations with \mathbf{S}_A and \mathbf{S}_B close to the z -axis are energetically favorable. It is noteworthy that the condition $h_x \gg \omega_0$ is not indispensable for quantum tunneling of \mathbf{n} , but only assures that a tunnel scenario remains applicable for a wider range of k_z (Sec. 2.2.1). In contrast, $\hbar h_x \gg |\delta s|8J/N$ guarantees that there are two energetically degenerate, macroscopically distinct spin configurations between which spin tunneling may take place [79] and hence, in general, will shift the range of magnetic fields in which a tunneling scenario as discussed in the present context is valid. Henceforth, we will always assume that B_x is large enough to satisfy Eq. (3.18). For sufficiently large k_z , the two-state model for the low energy sector of the system outlined in Sec. 2.2 then still applies. As Eq. (3.17) indicates, the modified AFMR exhibits one important novel feature: as \mathbf{n} tunnels between \mathbf{e}_z and $-\mathbf{e}_z$ ($\phi = \pi/2$ and $\phi = 3\pi/2$, respectively), the z -component of the total spin, S_z , oscillates between $S_0 = (\delta s \omega_0^2/h_x^2 + (k'_z s'^2 - k_z s^2)/2Js)$ and $-S_0$.

3.2.2 Thermodynamics of the modified antiferromagnetic molecular rings

In order to quantify the statements on Néel vector tunneling in modified AFMR's, we now develop a semiclassical theory of the modified AFMR. In this section, we discuss thermodynamic quantities such as the magnetization M_x and specific heat c_v . While our theory treats the spins semiclassically, we give the explicit dependence on the microscopic parameters of \hat{H} [Eq. (3.11)]. To this end we evaluate the partition function Z , thus generalizing the procedure reviewed in Sec. 2.2 to systems with $k'_z \neq k_z$, $J' \neq J$, and $\delta s \neq 0$. The most significant change is that, for $\delta s \neq 0$, the staggering [Eq. (2.15)] must be modified in order to account for $s_1^2 = s'^2$. The ansatz

$$\begin{aligned} \mathbf{s}_1 &= s' \mathbf{n} + \frac{s'}{s} \mathbf{l}, \\ \mathbf{s}_i &= (-1)^{i+1} s \mathbf{n} + \mathbf{l} \quad \forall i \neq 1 \end{aligned} \quad (3.19)$$

is equivalent to the assumption that spins within sublattices A and B are ferromagnetically coupled [11, 49, 50, 66, 77, 78]. The results for the magnetization M_x and susceptibilities obtained from this ansatz turn out to be in good agreement with numerical exact diagonalization (see below and Sec. 3.2.3) as long as $|J'/J - 1| \ll 1$. We restrict our considerations to this case first and discuss further limiting cases $J' \ll J$ and $J' \gg J$ in Sec. 3.2.4.

As for the AFMR [65], at low temperatures spatial variations of the Néel field \mathbf{n} and the fluctuations \mathbf{l} around it are suppressed in small ring system. With the coherent spin states defined in Eq. (3.19) [47],

$$Z = \int \mathcal{D}\mathbf{n} \mathcal{D}\mathbf{l} \delta(\mathbf{n} \cdot \mathbf{l}) e^{-S[\mathbf{n}, \mathbf{l}]/\hbar}, \quad (3.20)$$

where

$$\begin{aligned} S[\mathbf{n}, \mathbf{l}] &= -i\hbar \left(s' \omega[\mathbf{n} + \frac{1}{s} \mathbf{l}] + s \sum_{i=2}^N \omega[(-1)^{i+1} \mathbf{n} + \frac{1}{s} \mathbf{l}] \right) \\ &\quad + \int_0^{\beta\hbar} d\tau H[\mathbf{n}, \mathbf{l}]. \end{aligned} \quad (3.21)$$

Here,

$$\begin{aligned} H[\mathbf{n}, \mathbf{l}] &= 2[(N-2)J + 2\frac{s'}{s}J']\mathbf{l}^2 + \hbar(N + \frac{\delta s}{s})\mathbf{h} \cdot \mathbf{l} \\ &\quad - [(N-1)k_z s^2 + k'_z s'^2]n_z^2 + \frac{2}{s}(k_z s^2 - k'_z s'^2)n_z l_z \\ &\quad + \delta s \hbar \mathbf{h} \cdot \mathbf{n} \end{aligned} \quad (3.22)$$

is the classical energy of a given spin configuration determined by \mathbf{n} and \mathbf{l} . The small term $[(N-1)k_z + k'_z]l_z^2$ has already been neglected. The first term in Eq. (3.21) is the Berry-phase term, where $\omega[\Omega]$ denotes the area traced out by some vector $\Omega(\tau)$ on the unit sphere. Here, we use the south pole gauge (i.e. $\omega[\Omega(\tau) \equiv -\mathbf{e}_x] = 0$). Expanding the Berry-phase term to leading order in \mathbf{l} with the parametrization Eq. (2.17) yields

$$-\int_0^{\beta\hbar} d\tau \left[i\delta s \dot{\phi}(1 + \cos\theta) + i\left(N + \frac{\delta s}{s}\right)(\mathbf{n} \times \dot{\mathbf{n}}) \cdot \mathbf{l} \right]. \quad (3.23)$$

The first term is due to the fact that, for $\delta s \neq 0$, the Berry-phase terms of the antiferromagnetically ordered components $s'\omega[\mathbf{n}] + s\sum_{i=2}^N \omega[(-1)^{i+1}\mathbf{n}] = \int d\tau (Ns\dot{\phi} + \delta s\dot{\phi}(1 + \cos\theta))$ do not add to an integer multiple of 2π [51, 83].

Carrying out the Gaussian integral over \mathbf{l} we obtain $Z = \int \mathcal{D}\mathbf{n} \exp(-\int_0^{\beta\hbar} d\tau L[\mathbf{n}]/\hbar)$, with a Euclidean Lagrangean

$$\begin{aligned} L[\mathbf{n}] = & \frac{N\hbar^2}{8\tilde{J}} [-(\mathbf{h} + h_A n_z \mathbf{e}_z - i\mathbf{n} \times \dot{\mathbf{n}})^2 \\ & + ((\mathbf{h} + h_A n_z \mathbf{e}_z) \cdot \mathbf{n})^2 - \tilde{\omega}_0^2 n_z^2] \\ & + \delta s \hbar [\mathbf{h} \cdot \mathbf{n} - i\dot{\phi}(1 + \cos\theta)], \end{aligned} \quad (3.24)$$

where

$$\begin{aligned} \frac{\tilde{J}}{N} &= \frac{(N-2)J + 2s'J'/s}{(N + \delta s/s)^2}, \\ h_A &= \frac{2(k_z s^2 - k'_z s'^2)}{(N + \delta s/s)s\hbar}, \\ \tilde{\omega}_0^2 &= \frac{8\tilde{J}}{N} [(N-1)k_z s^2 + k'_z s'^2]. \end{aligned} \quad (3.25)$$

Equation (3.24) is the analogue of Eq. (2.16) for the AFMR. A finite excess spin δs of the modified AFMR leads to two significant changes in $L[\mathbf{n}]$. Firstly, the typical energy scales of the system are slightly renormalized, $J \rightarrow \tilde{J}$ and $\omega_0 \rightarrow \tilde{\omega}_0$, even for $J' = J$ and $k'_z = k_z$. More importantly, L acquires an additional term due to the Zeeman energy and Berry phase of the uncompensated spin $\delta s \mathbf{n}$. For all cases of experimental interest, because of Eq. (3.14) we have $h_A \ll \tilde{\omega}_0 \ll h_x$. The h_A -dependent terms in Eq. (3.24) hence lead only to minor modifications of the thermodynamic properties of the modified AFMR compared to the AFMR, but feature in the dynamics.

Again, we consider a magnetic field $\mathbf{B} = B_x \mathbf{e}_x$ in the ring plane. We will show now that, for $h_x \neq 0$, \mathbf{n} and hence the excess spin no longer trace a

tunneling path in the (y, z) -plane. With the parameterization in Eq. (2.17),

$$\begin{aligned} L[\phi, \theta] \simeq & \frac{N\hbar^2}{8\tilde{J}} [-(h_x - i\dot{\phi})^2 - \tilde{\omega}_0^2 \sin^2 \phi] - i\hbar \delta s \dot{\phi} \\ & + \frac{N\hbar^2}{8\tilde{J}} \left[\dot{\theta}^2 + \cos^2 \theta \left((h_x - i\dot{\phi})^2 + \tilde{\omega}_0^2 \sin^2 \phi \right) \right. \\ & \left. + 2 \cos \theta (h_x - i\dot{\phi}) \left(\delta s \frac{4\tilde{J}}{N\hbar} + h_A \sin^2 \theta \sin^2 \phi \right) \right]. \end{aligned} \quad (3.26)$$

The timescales for the dynamics of ϕ and θ separate because of Eq. (3.18), and we can again invoke the adiabatic approximation used in Sec. 2.2.1. θ oscillates in a slowly varying harmonic potential with the potential minimum at θ_0 , where

$$\cos \theta_0 = -\frac{h_x - i\dot{\phi}}{(h_x - i\dot{\phi})^2 + \tilde{\omega}_0^2 \sin^2 \phi} \left(\frac{4\tilde{J}}{N\hbar} \delta s + h_A \sin^2 \phi \right). \quad (3.27)$$

Corrections to the adiabatic approximation are beyond the order of the present calculation. Equation (3.27) shows that finite $\delta s \neq 0$ or $h_A \neq 0$ leads to a shift in the saddle-points of the Lagrangean $L[\phi, \theta]$ away from $\theta_0 = \pi/2$ because, then, $\mathbf{S}_A - \mathbf{S}_B$ no longer lies in the (y, z) -plane [Fig. 3.4(c)]. Expanding Eq. (3.26) to second order in $\vartheta = \theta - \theta_0$ and carrying out the Gaussian integral over ϑ , we obtain a ϕ -dependent effective Lagrangean

$$\begin{aligned} L[\phi] = & \frac{N\hbar^2}{8\tilde{J}} [-(h_x - i\dot{\phi})^2 - \tilde{\omega}_0^2 \sin^2 \phi] - i\hbar \left(\delta s + \frac{1}{2} \right) \dot{\phi} \\ & + \hbar \frac{h_x}{2} + \mathcal{O}(\tilde{\omega}_0^2/h_x, Nh_A\tilde{\omega}_0/8\tilde{J}). \end{aligned} \quad (3.28)$$

Comparison with the corresponding Lagrangean for $\delta s = 0$ [Eq. (2.19)] shows that, to leading order in the excess spin δs and anisotropy field h_A , the only effect of an excess spin is to introduce an additional topological phase $-i\delta s \dot{\phi}$. In particular, in contrast to the case $h_x = 0$ discussed in earlier work on tunneling in ferrimagnets, [11, 12, 66, 77, 78] the potential barrier and hence the real part of the tunnel action is only slightly altered by the excess spin. This is due to the fact [79] that, for $\hbar h_x > |\delta s|8J/N$ [Eq. (3.18)], the system is in the antiferromagnetic regime in which the tunnel splitting is only slightly modified by the excess spin. Note that Eq. (3.28) is formally identical to Eq. (2.19), which provides a rigorous proof of the statement that the modified AFMR also may exhibit tunneling of \mathbf{n} for sufficiently large anisotropy, as already claimed on basis of physical arguments at the end of Sec. 3.2.1.

Using the same techniques as for the AFMR with compensated sublattice spins, for the partition function we find

$$Z = 2 \exp \left[\beta \left(\frac{N\hbar^2}{8\tilde{J}} h_x^2 - \hbar \frac{h_x + \tilde{\omega}_0}{2} \right) \right] \cosh \left(\frac{\beta \tilde{\Delta}}{2} \right), \quad (3.29)$$

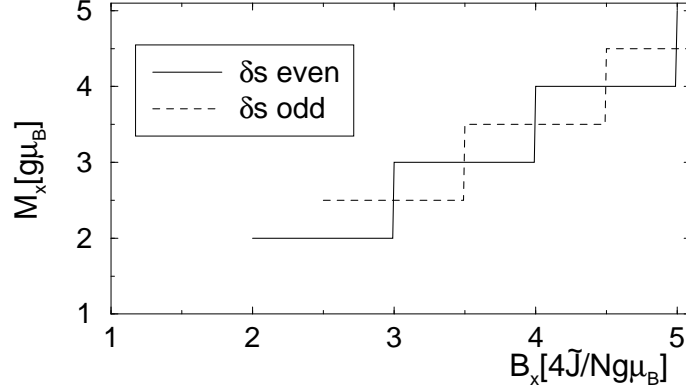


Figure 3.5: Schematic plot of the ground-state magnetization of a modified AFMR with integer (—) and half-integer (- -) δs , respectively.

with the tunnel splitting

$$\tilde{\Delta}(h_x) = \tilde{\Delta}_0 \left| \sin \pi \left(\frac{N\hbar}{4\tilde{J}} h_x + \delta s \right) \right|, \quad (3.30)$$

where $\tilde{\mathcal{S}}/\hbar = N\tilde{\omega}_0/2\tilde{J}$ and $\tilde{\Delta}_0 = 8\hbar\tilde{\omega}_0\sqrt{\tilde{\mathcal{S}}/2\pi\hbar}\exp(-\tilde{\mathcal{S}}/\hbar)$. From Eq. (3.29) it is also straightforward to derive all thermodynamic quantities of interest. In particular, for the free energy F , the magnetization M_x , and the specific heat c_v we obtain

$$F = \hbar \frac{\tilde{\omega}_0 + h_x}{2} - \frac{N\hbar^2}{8\tilde{J}} h_x^2 - \frac{1}{\beta} \ln \cosh \left(\frac{\beta\tilde{\Delta}}{2} \right), \quad (3.31)$$

$$M_x = (g\mu_B) \left[\frac{N\hbar h_x}{4\tilde{J}} - \frac{1}{2} + \frac{1}{2\hbar} \frac{\partial \tilde{\Delta}}{\partial h_x} \tanh \left(\frac{\beta\tilde{\Delta}}{2} \right) \right], \quad (3.32)$$

$$c_V = k_B \left(\frac{\beta\tilde{\Delta}}{2} \right)^2 \cosh^{-2} \left(\frac{\beta\tilde{\Delta}}{2} \right). \quad (3.33)$$

The most significant change in the thermodynamic properties of the modified AFMR is that, for half-integer δs , the zeros of $\tilde{\Delta}$ and hence the magnetization steps are shifted by a magnetic field $2\tilde{J}/Ng\mu_B$, i.e., by half of a magnetization plateau, compared to the unmodified AFMR (Fig. 3.5). The magnetization plateaus then lie at half-integer spin values. At low T , the specific heat c_v exhibits a characteristic Schottky anomaly, with a peak at $T \simeq 0.4\tilde{\Delta}/k_B$.

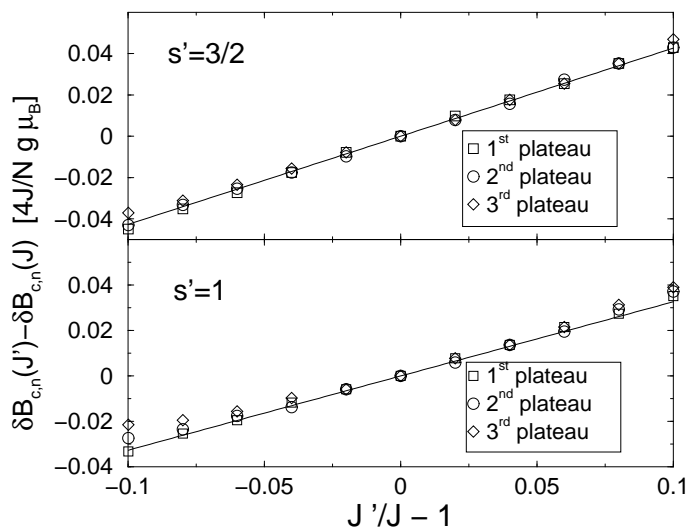


Figure 3.6: Comparison of exact diagonalization (symbols) and analytical (—) results for the difference in plateau width, $\delta B_{c,n}(J') - \delta B_{c,n}(J = J)$, as function of $J' - J$ for $\delta s = -1/2$ (upper panel) and $\delta s = -1$ (lower panel). $N = 4$, $s = 2$, $k_z = k'_z = 0.1J$. The numerical error of the data points, $\pm 0.002 \times 4J/Ng\mu_B$, is smaller than the symbol size.

The width of the magnetization plateaus, $\delta B_{c,n} = B_{c,n+1} - B_{c,n} = 4\tilde{J}/Ng\mu_B$, where $B_{c,n}$ is the field at which the magnetization M_x exhibits the n^{th} step, is a quantity which is accessible in experiments and from which J' can be inferred. Our theory predicts

$$\delta B_{c,n}(J') - \delta B_{c,n}(J = J) = 8 \frac{s'/s}{(N + \delta s/s)^2} \frac{(J' - J)}{g\mu_B}. \quad (3.34)$$

In Fig. 3.6 we compare the functional dependence predicted by Eq. (3.34) with the results of exact diagonalization on small rings, $N = 4$, $s = 2$, $s' = 3/2$ (upper panel) and $s' = 1$ (lower panel), respectively, for $|J'/J - 1| \leq 0.1$. The absolute value of $\delta B_{c,n}$ deviates from $4\tilde{J}/Ng\mu_B$ by terms of order $\tilde{\omega}_0^2/h_x^2$, which is beyond the precision of our result Eq. (3.28). Hence, we compare exact diagonalization and analytical results only for $\delta B_{c,n}(J') - \delta B_{c,n}(J)$, for which this shift nearly cancels. The exact diagonalization results are in good agreement with the analytical result. The deviations for $|J'/J - 1| \gtrsim 0.1$ signal the breakdown of our ansatz in Eq. (3.19) for J' significantly different from J (see Sec. 3.2.4 below).

We show next that although, for a given direction of \mathbf{n} , the total spin \mathbf{S} acquires a component perpendicular to the field \mathbf{B} , the magnetization $M_\alpha = 0$ still

vanishes for $\alpha = y, z$. We define the fields $m_\alpha(\tau) = \delta \int d\tau L[\mathbf{n}] / \delta(\hbar h_\alpha(\tau))|_{h_\alpha=0}$ such that $M_\alpha = -(g\mu_B) \int \mathcal{D}\mathbf{n} m_\alpha(\tau) e^{-\int d\tau L/\hbar} / Z$. Using Eq. (3.26), we obtain

$$\begin{aligned} m_z &= \frac{N\hbar}{4\tilde{J}} [-h_A n_z (1 - n_z^2) \\ &\quad + h_x n_x n_z + i(\mathbf{n} \times \dot{\mathbf{n}})_z] + \delta s n_z \\ &\simeq -\frac{N\hbar}{4\tilde{J}} h_A \sin \phi + \delta s \frac{\tilde{\omega}_0^2}{(h_x - i\dot{\phi})^2} \sin^3 \phi \\ &\quad + i \frac{N\hbar}{4\tilde{J}} \dot{\theta}_0 \cos \phi + \mathcal{O}(\vartheta), \end{aligned} \quad (3.35)$$

with θ_0 defined in Eq. (3.27). Note that the classical value for m_z at the saddle points of the path integral, $\phi = \pi/2$ and $3\pi/2$, respectively, coincides with the value derived from the classical vector model in Sec. 3.2.1, as it should. Because $m_z(\phi + \pi) = -m_z(\phi)$ while the Lagrangean remains invariant for $\phi \rightarrow \phi + \pi$, $M_y = M_z = 0$ for arbitrary h_x . In particular, at $T = 0$, $M_z = 0$ indicates that the ground-state is not a state with definite direction of \mathbf{n} , but rather a coherent superposition of such states, $(|\uparrow\rangle + |\downarrow\rangle)/\sqrt{2}$, as expected for a system which shows coherent Néel vector tunneling.

3.2.3 Dynamics of the modified antiferromagnetic molecular rings

As we have shown above, the effective action $L[\phi]$ of the modified AFMR [Eq. (3.28)] is formally identical to that of the AFMR [Eq. (2.19)]. In particular, for large anisotropy k_z , such that $\tilde{\mathcal{S}}/\hbar \gg 1$, the modified AFMR is in the quantum tunneling regime. In this section, we evaluate explicitly the spin susceptibilities $\chi_{\alpha\alpha}(\tau)$ for the modified AFMR.

In order to motivate this, we first calculate χ_{zz} using the results of the classical vector model (Sec. 3.2.1). For \mathbf{n} along \mathbf{e}_z or $-\mathbf{e}_z$, the z -component of the total spin vector is finite, $S_z = \pm S_0$, where $S_0 = \delta s \omega_0^2 / h_x^2 + (k'_z s'^2 - k_z s^2) / 2Js$. For $\mathbf{n}(t=0) = \mathbf{e}_z$, the coherent tunneling of \mathbf{n} then results in an oscillating $S_z(t) = S_0 \cos(\tilde{\Delta}t/\hbar)$, such that the Fourier transform of the (real-time) susceptibility exhibits an absorption pole $\chi''_{zz}(\omega \simeq \tilde{\Delta}/\hbar) = \pi |S_0|^2 \tanh(\beta\tilde{\Delta}/2) \delta(\omega - \tilde{\Delta}/\hbar)$.

Generalizing the procedure for the AFMR (Sec. 2.2.2) to $\delta s \neq 0$, we calculate the quantum corrections to this result from [84]

$$\begin{aligned} \chi_{zz}(\tau) &= (g\mu_B)^2 \frac{N\hbar}{4\tilde{J}} (1 - \langle \sin^2 \phi \rangle) \delta(\tau) \\ &\quad + (g\mu_B)^2 \frac{1}{Z} \int \mathcal{D}\mathbf{n} e^{-\int_0^{\beta\hbar} d\tau L[\mathbf{n}]/\hbar} m_z(\tau) m_z(0), \end{aligned} \quad (3.36)$$

with $m_z(\tau)$ given in Eq. (3.35). As for the undoped AFMR, the correlations of the ϑ -terms in $m_z(\tau)$ give rise to a strongly peaked term $(g\mu_B)^2 N\hbar\delta(\tau)\langle\sin^2\phi\rangle/4\tilde{J}$. We then find

$$\begin{aligned}\chi_{zz}(\tau) &= (g\mu_B)^2 \frac{N\hbar}{4\tilde{J}} \delta(\tau) \\ &+ (g\mu_B)^2 \frac{1}{Z} \int \mathcal{D}\phi e^{-\int_0^{\beta\hbar} d\tau L[\phi]/\hbar} \left(-\frac{N\hbar h_A}{4\tilde{J}} \sin\phi(\tau) \right. \\ &\left. + \delta s \frac{\tilde{\omega}_0^2}{h_x^2} \sin^3\phi(\tau) \right) \left(-\frac{N\hbar h_A}{4\tilde{J}} \sin\phi + \delta s \frac{\tilde{\omega}_0^2}{h_x^2} \sin^3\phi \right).\end{aligned}\quad (3.37)$$

Terms proportional to $\cos\phi$ in m_z lead only to small contributions of order $\exp(-\tilde{S}/\hbar)$ to $|\langle e|\hat{S}_z|g\rangle|$. This allows us to neglect the term $i\dot{\theta}_0 \cos\phi$ [Eq. (3.35)]. In stark contrast to the AFMR, the path integral in Eq. (3.37) gives rise to terms proportional to $\exp(\pm\tilde{\Delta}|\tau|/\hbar)$ such that, upon Fourier transform, the susceptibility in Matsubara representation contains terms $1/(i\omega_n \pm \tilde{\Delta}/\hbar)$. The path integral is most easily evaluated in a Hamiltonian description. We requantize the field ϕ and use an effective two-state Hamiltonian to evaluate the matrix elements. Inserting the expression for h_A , we find (see Appendix A.2 for further details)

$$\begin{aligned}|\langle e|\hat{S}_z|g\rangle| &= \left| \frac{N(k'_z s'^2 - k_z s^2)}{2\tilde{J}s(N + \delta s/s)} \left(1 - \frac{\tilde{J}}{N\hbar\tilde{\omega}_0} \right) \right. \\ &\quad \left. + \delta s \frac{\tilde{\omega}_0^2}{h_x^2} \left(1 - 3\frac{\tilde{J}}{N\hbar\tilde{\omega}_0} \right) \right|,\end{aligned}\quad (3.38)$$

$$\begin{aligned}\chi''_{zz}(\omega \simeq \tilde{\Delta}/\hbar) &= \pi(g\mu_B)^2 |\langle e|\hat{S}_z|g\rangle|^2 \\ &\quad \times \tanh\left(\frac{\beta\tilde{\Delta}}{2}\right) \delta(\omega - \tilde{\Delta}/\hbar).\end{aligned}\quad (3.39)$$

Equations (3.38) and (3.39) are the main results of this section.

For $\delta s = -5/2$ or -1 (for Ga and Cr dopants in a ferric wheel, respectively), $|\langle e|\hat{S}_z|g\rangle|$ can be of order 0.1 even for $h_x \gtrsim 3\tilde{\omega}_0$. For $k_B T \lesssim \tilde{\Delta}$ the susceptibility of the modified AFMR then exhibits a resonance at $\omega = \pm\tilde{\Delta}/\hbar$ which is accessible in AC magnetic susceptibility or ESR measurements. The terms $\tilde{J}/N\hbar\tilde{\omega}_0 = 1/(2\tilde{S}/\hbar)$ in $|\langle e|\hat{S}_z|g\rangle|$ are quantum corrections to the classical result derived at the beginning of this section.

So far we have ignored decoherence of the spin tunneling, which is crucial for the notion of macroscopic quantum coherence. The condition $\Gamma_{\text{dec}} \simeq \tilde{\Delta}/\hbar$, where Γ_{dec} is the electron spin decoherence rate, marks the transition from coherent to incoherent tunneling dynamics. As is evident from the classical

vector model discussed in Sec. 3.2.1, S_z follows the tunneling dynamics of \mathbf{n} . In particular, for a single modified AFMR, the decay rate of $|\langle n_z(t)n_z \rangle|$ for an AFMR prepared in state $|\uparrow\rangle = (|g\rangle + |e\rangle)/\sqrt{2}$ at $t = 0$, Γ_{dec} , is also the decay rate of $|\langle S_z(t)S_z \rangle|$. For $\Gamma_{\text{dec}} \neq 0$, the δ -peak in Eq. (3.39) is then broadened into a Lorentzian of width Γ_{dec} . In experiments carried out on an ensemble of modified AFMR's, inhomogeneous broadening (e.g. due to crystal defects or nuclear spins) adds to the width of the resonance peaks. The experimentally determined linewidth of the absorption and emission peaks provides an upper limit for Γ_{dec} . This should allow one to settle the experimentally unresolved problem of whether true quantum coherence is established in AFMR's.

Finally we compare our result for the transition matrix element $|\langle e|S_z|g\rangle|$ entering Eq. (3.39) with results obtained from exact diagonalization on small rings for a wide range of parameters (Figs. 3.7, 3.8, and 3.9). For simplicity, we assume $J' = J$. In the range of validity of our theory [Eq. (3.18)], for $\delta s \neq 0$ (Figs. 3.7 and 3.9), the agreement of exact diagonalization (\diamond) with analytic results ($—$) is both qualitatively and quantitatively convincing. The small oscillating features seen in the exact results are due to tunneling corrections $\mathcal{O}(\exp[-\tilde{S}/\hbar])$ to $|\langle e|S_z|g\rangle|$, which were neglected in Eq. (3.38). For Fig. 3.8, where $\delta s = 0$, our theory makes the correct qualitative prediction that $|\langle e|S_z|g\rangle|$ depends only weakly on h_x , but overestimates the matrix element. However, due to the smallness of the matrix element for $\delta s = 0$, the discrepancy arises from terms neglected in the derivation of Eq. (3.28). The significantly different qualitative features of Fig. 3.8 compared to Figs. 3.7 and 3.9 arise from the fact that $\delta s = 0$ in Fig. 3.8. The different functional dependence of $|\langle e|S_z|g\rangle|$ on h_x for the two cases $\delta s \neq 0$ and $\delta s = 0$ is well understood within the theoretical framework presented here [Eq. (3.38)]. The very large difference in matrix element magnitude illustrates the importance of looking at doped rings in experiment.

We conclude this section by remarking that, for finite excess spin δs , the second transverse susceptibility $\chi''_{yy}(\omega)$ also has an absorption pole at $\omega = \tilde{\Delta}/\hbar$. However, since \mathbf{e}_y is a hard axis, the spectral weight of this pole is significantly smaller than that of $\chi''_{zz}(\omega)$, such that Néel vector tunneling in the modified AFMR's can be more easily detected by probing the latter quantity.

3.2.4 Thermodynamics and spin dynamics for $J'/J \gg 1$ and $J'/J \ll 1$

The deviations of the exact diagonalization results from our theoretical predictions shown in Fig. 3.6 indicate that, for $J'/J \ll 1$ or $J'/J \gg 1$, the theory developed in Sec. 3.2.2 is no longer immediately applicable. Indeed, results obtained by exact diagonalization for the ground-state magnetization M_x in small

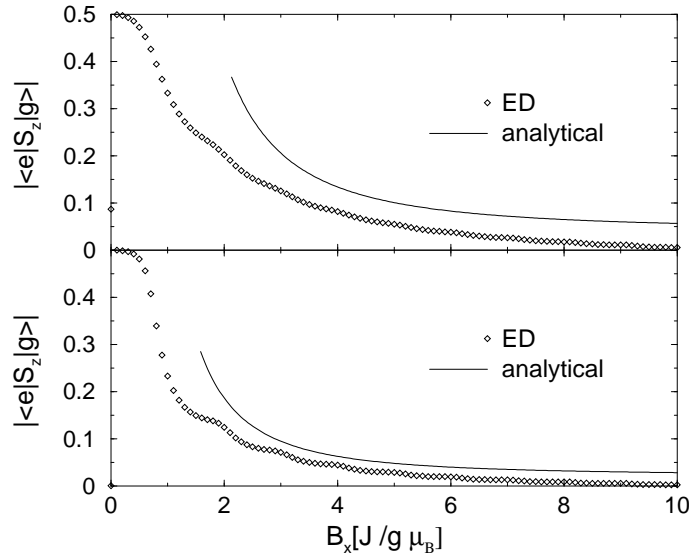


Figure 3.7: Transition matrix element $|\langle e|S_z|g\rangle|$ for small rings ($N = 4$) with $J' = J$, $s = 5/2$, $s' = 2$. In the upper panel, $k_z = k'_z = 0.1$. In the lower panel, $k_z = k'_z = 0.055J$ is chosen such that $\tilde{S}/\hbar \simeq 3.3$ as for Fe_{10} . The analytical result (—) is shown for $\max[\hbar\tilde{\omega}_0, |\delta s|8J/N] < \hbar h_x < 4Js$. Due to Eq. (3.18), our theory is rigorously valid only for fields much larger than $\max[\hbar\tilde{\omega}_0, |\delta s|8J/N]$ and much smaller than $4Js$.

rings ($N = 4$, $s = 2$, and $s' = 3/2$) (Fig. 3.10) show that one of the main results of Sec. 3.2.2, that M_x exhibits a series of equally spaced magnetization steps, does not hold any more. As we will show below, this is because our ansatz Eq. (3.19) needs to be modified for J' significantly different from J . In this section we show that, for the limiting cases of $J' \gg J$ or $J' \ll J$, the modified AFMR can be mapped onto the problem discussed in the preceding sections. We discuss the qualitative features of M_x for these systems and show that coherent tunneling of \mathbf{n} also results in coherent oscillations of the total spin.

$J' \ll J$: In this limit, \mathbf{s}_1 decouples from all other spins and aligns antiparallel to \mathbf{B} for $\hbar h_x \gtrsim J's$. The remaining spins $\mathbf{s}_2, \mathbf{s}_3, \dots, \mathbf{s}_N$ form an open spin chain, as sketched in Fig. 3.11(a). The Lagrangean of an open spin chain with an odd number of spins can also be mapped onto Eq. (3.28), with $\delta s = s$ and slightly renormalized $\tilde{J} = JN(N-2)/(N-1)^2$. We predict that M_x has the following features:

- $M_x \gtrsim g\mu_B(s' + s)$ for $2J's \ll \hbar h_x$.

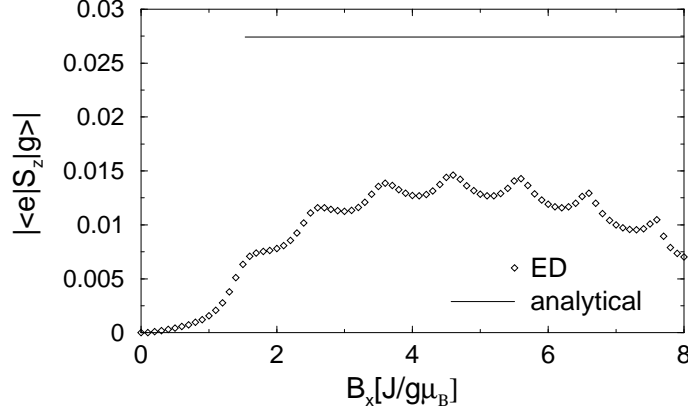


Figure 3.8: Transition matrix element $|\langle e|S_z|g\rangle|$ for a small ring ($N = 4$) with $J' = J$, $s = s' = 2$, i.e., $\delta s = 0$, but $k'_z = 1.5k_z$ and, hence, $h_A \neq 0$. Again, $k_z = 0.0655J$ is chosen such that $\tilde{S}/\hbar \simeq 3.3$, as for Fe_{10} . The analytical result (—) is shown for $\max[\hbar\tilde{\omega}_0, |\delta s|8J/N] < \hbar h_x < 4Js$. See also caption of Fig. 3.7.

- For $\max[\hbar\tilde{\omega}_0, s8\tilde{J}/N] \ll \hbar h_x \ll 4\tilde{J}s$, M_x exhibits a series of equally spaced magnetization steps with plateau width $\delta B_{c,n} = 4\tilde{J}/Ng\mu_B$. Depending on whether δs is half-integer or integer, the plateaus correspond to states with half-integer or integer total spin, respectively.

$J' \gg J$: In this limit, the spins \mathbf{s}_N , \mathbf{s}_1 and \mathbf{s}_2 are strongly coupled. In a semiclassical picture, \mathbf{s}_1 aligns antiparallel to \mathbf{s}_N and \mathbf{s}_2 and the three spins act as one single spin $|2s - s'|$ coupled to \mathbf{s}_3 and \mathbf{s}_{N-1} with exchange constant J [Fig. 3.11(b)]. For simplicity, we assume $s' < 2s$. Then, for $\hbar h_x \ll J'(s - \delta s + 1)$, \hat{H} can be mapped onto a Hamiltonian of the form Eq. (3.11) with $N \rightarrow N - 2$, $J' \rightarrow J$, $k'_z \rightarrow (k'_z s'^2 + 2k_z s^2)/(2s - s')^2$, and $s' \rightarrow 2s - s' = s - \delta s$. Because all $N - 2$ exchange couplings in the new Hamiltonian are identical, the theory developed in Secs. 3.2.2 and 3.2.3 remains applicable. In particular, for the ground-state magnetization M_x we make the following predictions:

- For $\max[\hbar\tilde{\omega}_0, |\delta s|8J/(N-2)] \ll \hbar h_x \ll 4Js$, M_x exhibits a series of equally spaced magnetization steps with $\delta B_{c,n} \simeq 4J/(N-2)g\mu_B$. Depending on whether δs is half-integer or integer, the plateaus correspond to states with half-integer or integer total spin, respectively.
- For $\hbar h_x \gtrsim J'(s - \delta s + 1)$, the Zeeman energy is sufficiently large to destroy the antiferromagnetic configuration of \mathbf{s}_N , \mathbf{s}_1 , and \mathbf{s}_2 . This results in a series of additional magnetization steps with spacing J' .

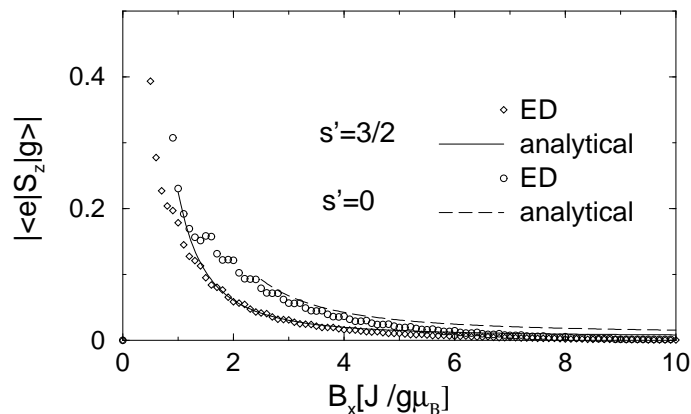


Figure 3.9: Transition matrix element $|\langle e|S_z|g\rangle|$ obtained with the phenomenological sublattice Hamiltonian [Eq. (3.12)] for Fe_{10} with one $s = 5/2$ substituted by (a) a dopant with $s' = 3/2$ (e.g. Cr) (numerical data \diamond , analytical prediction —), and (b) a dopant with $s' = 0$ (e.g. Ga) (numerical data \circ , analytical prediction - -). Note that, in this case, the numerical data is not obtained from exact diagonalization of Eq. (3.11), but rather of Eq. (3.12). For simplicity, we assumed $J' = J$ and $k'_z = k_z = 0.0088J$. The analytical results (— and - -) are shown for $\max[\hbar\tilde{\omega}_0, |\delta s|8J/N] < \hbar h_x < 4Js$. See also caption of Fig. 3.7.

Note that a similar argument also applies if $J' < 0$. In this case, the three spins \mathbf{s}_N , \mathbf{s}_1 , and \mathbf{s}_2 are ferromagnetically coupled and align parallel. Again, the system can be mapped onto a smaller ring (as in Fig. 3.11b), where now $s' \rightarrow 2s + s'$. The magnetization curve resembles the one shown in the upper panel of Fig. 3.10. In Fig. 3.10, exact diagonalization results for small rings with $N = 4$, $s = 2$, $s' = 3/2$ are displayed. The qualitative features agree with all of the above predictions.

We conclude that even the qualitative features of M_x allow one to estimate the parameter J' of a modified AFMR. Even more importantly, as we have shown, also for $J' \ll J$ and $J' \gg J$ the modified AFMR can be mapped onto the Lagrangean [Eq. (3.24)] of a system which exhibits quantum tunneling of \mathbf{n} . In all cases discussed above, the quantum tunneling of \mathbf{n} leads to coherent oscillations of the total spin \mathbf{S} , and thus can be observed in AC magnetic susceptibility or ESR measurements.

3.2.5 Discussion

The theory described in Secs. 3.2.2, 3.2.3, and 3.2.4 allowed us to derive explicit expressions for both thermodynamic quantities [Eqs. (3.32) and (3.33)] and

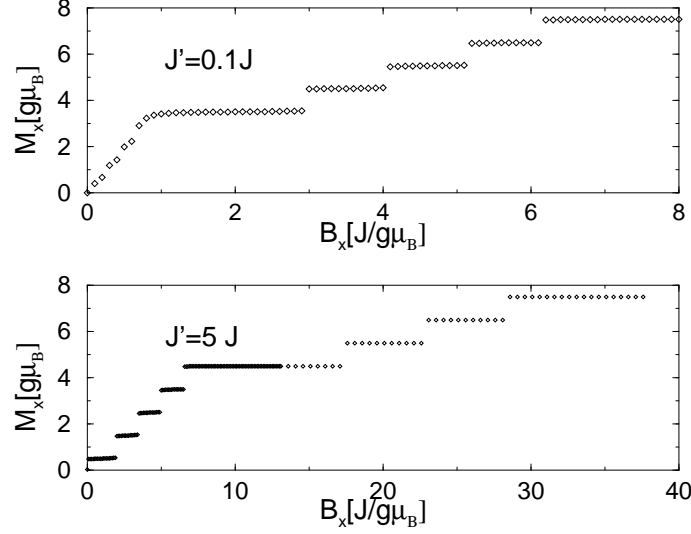


Figure 3.10: $M_x(B_x)$ at $T = 0$ for a small system with $J' \ll J$ (upper panel) or $J' \gg J$ (lower panel). Here, $N = 4$, $s = 2$, $s' = 3/2$, $k_z = k'_z = 0.1$.

the susceptibility χ''_{zz} [Eqs. (3.38) and (3.39)] of modified AFMR's. In order to establish a connection with experimental issues, we now outline the steps necessary to detect coherent Néel vector tunneling. For simplicity we restrict our considerations to Fe_{10} with Ga ($\delta s = -5/2$) or Cr ($\delta s = -1$) dopants, and assume $J' \simeq J$.

For finite excess spin δs , the two energetically degenerate spin configurations required for coherent spin tunneling as discussed in the present work certainly exist if $\hbar h_x \gg |\delta s|8J/N$ [Eq. (3.18)]. This tunneling regime is well within experimental reach for Cr dopants ($B_x \gg 9\text{T}$), but not for Ga dopants ($B_x \gg 23\text{T}$). Note that also the anisotropy energy favors a spin configuration as sketched in Fig. 3.4(c) such that the condition $\hbar h_x \gg |\delta s|8J/N$ can be relaxed. Consequently, also for Ga dopants a tunneling scenario is feasible. For Cr dopants ($s' \neq 0$), however, the two new parameters J' and k'_z introduced in \hat{H} [Eq. (3.11)] must first be determined in order to characterize the ring system.

Both J' and k'_z can be obtained from the measurement of two independent thermodynamic quantities, such as the ground-state magnetization and tunnel splitting. A schematic plot of the ground-state magnetization for integer δs (\circ) is shown in Fig. 3.5. Although the magnetization steps are smeared out at finite temperature, for $T \lesssim 1\text{K}$, the magnetization step spacing $\delta B_{c,n}$ still can be measured with high accuracy [55]. With $\delta B_{c,n} = 4\tilde{J}/Ng\mu_B$ and Eq. (3.25), this allows one to determine J' . The on-site anisotropy k'_z can be obtained from $\tilde{\Delta}$,

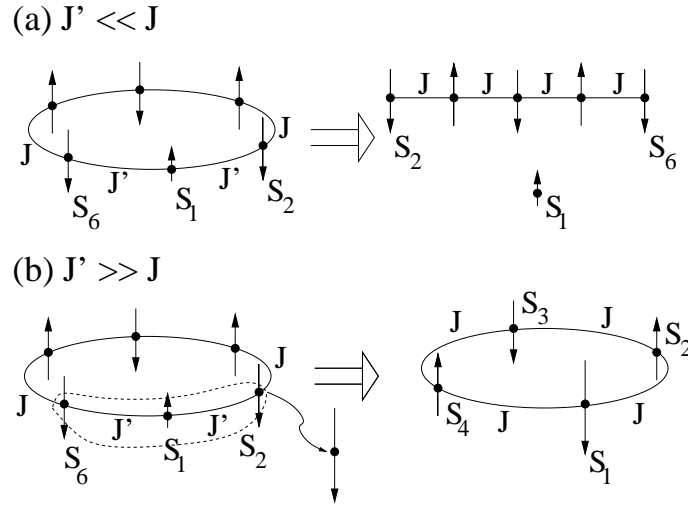


Figure 3.11: (a) For $J' \ll J$, \mathbf{s}_1 decouples from all other spins and the modified AFMR can be mapped onto an open spin chain excluding \mathbf{s}_1 . (b) For $J' \gg J$, \mathbf{s}_N , \mathbf{s}_1 , and \mathbf{s}_2 are strongly coupled and can be described as one single spin. The Hamiltonian of the ring then maps onto that of a modified AFMR with $J' = J$.

which depends sensitively on the tunnel action $\tilde{S} \propto \sqrt{(N-1)k_z s^2 + k'_z s'^2}$ and hence on k'_z . The tunnel splitting $\tilde{\Delta}$ (and hence k'_z) is accessible either in AC magnetic susceptibility or ESR measurements [Eq. (3.39)], or in measurements of thermodynamic quantities, such as c_v . Torque magnetometry is another experimental technique which has been used to determine the anisotropy constant with quasi-spectroscopic accuracy [60].

Once J' and k'_z are known, Eq. (3.39) determines both the position and the spectral weight of the resonance in $\chi''_{zz}(\omega)$ which arises from coherent quantum tunneling of \mathbf{n} . The characteristic functional dependence of $\tilde{\Delta}$ [Eq. (3.30)] and $|\langle e|S_z|g\rangle|^2$ [Eq. (3.38)] on h_x predicted by our theory can be checked experimentally. Finally, it is noteworthy that, although $\tilde{\Delta}$ can be determined from thermodynamic quantities, the key problem of macroscopic quantum coherence is the measurement of the decoherence rate Γ_{dec} which is accessible only in dynamic quantities, such as AC susceptibilities.

So far, we have considered AFMR's with only one dopant ion. As we have shown in the preceding sections, thermodynamic and dynamic quantities of doped AFMR's may differ significantly from those of undoped AFMR's. In the large samples investigated experimentally, doping will usually lead to a random distribution both of the number of dopant ions and of their position relative to the direction of the magnetic field. However, the random distribution of

impurities does not invalidate the above considerations. The choice of a low impurity concentration results in a large majority of the AFMR's containing no dopants or having only one dopant ion, which allows one to extract the system parameters of the singly doped AFMR's. When intraring dipolar interactions make a significant contribution to the effective uniaxial anisotropy k_z , doping with only one ion changes the effective anisotropy from uniaxial to biaxial. The theoretical framework presented above can be readily extended to account for biaxial anisotropies. Because the original uniaxial anisotropy dominates the biaxial correction, the altered tunnel splittings $\tilde{\Delta}_i$ in a singly doped AFMR with dopant at site i have a magnitude similar to Δ for the undoped AFMR, and a separation which is small by comparison. Thus AC susceptibility or ESR measurements can be expected to observe signals corresponding to reversals of the total spin accompanying Néel vector tunneling, and governed by the frequencies $\tilde{\Delta}_i$.

3.2.6 Spin quantum tunneling in ferritin

The theoretical framework developed above is quite general and applies to other systems besides AFMR's. In particular, the results of the classical sublattice model (Sec. 3.2.1) can be easily extended to different systems. In order to illustrate this, we now discuss natural horse-spleen ferritin and artificial magnetoferritin, in which spin quantum tunneling has already been studied experimentally [24, 25, 26] and theoretically [66, 77, 78, 79, 85]. The experiments were carried out in the presence of small static magnetic fields ($B_x \lesssim 10^{-6}\text{T}$). In this regime, $B_x \neq 0$ leads to an energy bias between the states $|\uparrow\rangle$ and $|\downarrow\rangle$, and tunneling is suppressed for increasing B_x .

As shown in Ref. [79], for sufficiently large field, $\hbar h_x \sim |\delta s| 8J/N$, there are again two energetically degenerate spin configurations between which spin quantum tunneling may take place. In natural horse-spleen ferritin [85], $J \simeq 200\text{K}$ and $\delta s/N \simeq 0.05$. For a system with uniaxial hard axis anisotropy, $\hat{H}_{an,z} = k_z \sum_i \hat{s}_{i,z}^2$, the tunnel barrier and hence the tunnel action can be effectively controlled over a wide range of parameters by varying the magnetic field B_x applied in the easy plane [79]. Tunneling in the plane perpendicular to \mathbf{B} gives rise to a topological phase acquired by the spins [11, 12, 48, 86]. A drawback of the setup considered in Ref. [79] is that, for uniaxial hard axis anisotropy, spin tunneling leaves the total spin \mathbf{S} invariant if \mathbf{B} is applied perpendicular to the hard axis. Similarly to the AFMR with equal sublattice spins, spin tunneling cannot be observed in AC magnetic susceptibility measurements.

However, experiments show that, in addition to the strong hard-axis anisotropy, ferritin also exhibits a second weak hard-axis anisotropy $\hat{H}_{an,y} = k_y \sum_i \hat{s}_{i,y}^2$, where $k_y/k_z \simeq 10^{-3}$ [85]. In self-sustaining films of natural horse-spleen ferritin, the hard axis \mathbf{e}_z is perpendicular to the film [26]. In the simplest

experimental setup, interference of different spin tunneling paths then could be explored if a field $\mathbf{B} = B_z \mathbf{e}_z$ is applied along the hard axis. As long as $\hbar h_z \ll N k_z s^2 / \delta s$ ($\simeq 10\text{K}$ for horse-spleen ferritin), due to the large anisotropy energy the spins remain confined to the film plane such that there are again two energetically degenerate spin configurations $|\uparrow\rangle$ and $|\downarrow\rangle$. Tunneling takes place in the plane perpendicular to \mathbf{B} , with a tunnel splitting

$$\Delta = \Delta_0 \left| \cos \pi \left(S_{\text{tot}} + \frac{N\hbar}{4J} h_z \right) \right|, \quad (3.40)$$

where $\Delta_0 \simeq 5 \times 10^{-5} \text{K} k_B$ and the total staggered spin is $S_{\text{tot}} \simeq 2.5 \times 4500$ for natural horse-spleen ferritin. Δ is periodic as a function of B_z , with a period $\delta B_z = 4J/Ng\mu_B$ ($\simeq 0.13\text{T}$ for natural horse-spleen ferritin). The advantage of this tunnel scenario is that quantum tunneling of \mathbf{n} also results in a tunneling of the excess spin δs , and hence leads to a large resonance peak in the susceptibility per ferritin molecule, i.e.,

$$\chi''_{xx}(\omega \simeq \Delta/\hbar) \simeq \frac{1}{2} \pi (\delta s)^2 \tanh \left(\frac{\beta \Delta}{2} \right) \delta(\omega - \Delta/\hbar). \quad (3.41)$$

The factor $1/2$ takes into account the random distribution of easy axes in the film plane. Due to the spread in particle number, the total staggered spin of the system can be either integer or half-integer. Hence, one will observe two different tunnel splittings varying with h_z as $\Delta = \Delta_0 |\cos(\pi N \hbar h_z / 4J)|$ and $\Delta = \Delta_0 |\sin(\pi N \hbar h_z / 4J)|$. An experimental confirmation of this behavior would provide further strong evidence that the resonance observed in AC susceptibility measurements in ferritin [24, 25, 26] represents coherent macroscopic spin quantum tunneling. The period of the oscillations of Δ as function of the applied field B_z would allow one to estimate the total number of tunneling spins.

3.2.7 Conclusion

The antiferromagnetic ring systems discussed here, modified AFMR's which are already available to experimentalists, combine the advantages of antiferromagnetic and ferromagnetic molecular magnets. The tunnel splitting $\tilde{\Delta}$ is sufficiently large that quantum coherence between macroscopically different states is established. Tunneling of the Néel vector \mathbf{n} also leads to a tunneling of the total spin \mathbf{S} , thus making the spin dynamics in modified AFMR's accessible to experiment. We have considered the simplest realistic model Hamiltonian \hat{H} [Eq. (3.11)] for a system in which, for example, one of the Fe ions of a ferric wheel is exchanged by Cr or Ga. We showed that the additional parameters entering \hat{H} can be inferred from equilibrium quantities such as the magnetization. Moreover, for a wide range of parameters, the system still exhibits macroscopic

quantum coherence in the form of coherent tunneling of \mathbf{n} . Finally, we calculated spin correlation functions of the modified AFMR and showed that tunneling of \mathbf{n} can indeed be observed in AC magnetic susceptibility or ESR experiments, which allow one to measure both the tunnel splitting $\tilde{\Delta}$ and an upper bound for the decoherence rate Γ_{dec} . Hence these measurements are appropriate to verify experimentally that Néel vector tunneling in AFMR's is coherent.

Our analysis has been based on spin coherent-state path integrals which lead to a nonlinear sigma-model description for the modified AFMR. The main advantage of this technique over exact diagonalization is that thermodynamic and dynamic quantities can be evaluated for a realistic system size. In addition, an intuitive physical understanding of the spin dynamics (quantum tunneling of \mathbf{n}) is obtained. A drawback of the analytical approach chosen is that it naturally requires approximations as discussed in Sec. 2.3. Corrections to our results, in particular $1/s$ -corrections, may become appreciable for the parameters of the AFMR's. However, our analytical results for $|\langle e|\hat{S}_z|g\rangle|$ agree well with exact diagonalization results obtained for small systems. For the parameter range explored in exact diagonalization, deviations from our theoretical predictions become significant mainly if s' is small ($s' = 1/2$ or 1), where the ansatz Eq. (3.19) fails due to large quantum fluctuations of $\hat{\mathbf{s}}_1$. Although numerical work on rings with $N = 6, 8,$ and 10 is challenging, some results have been obtained for the spin correlation functions in the undoped AFMR's (Sec. 2.3) where translational invariance reduces the dimension of the matrices which must be diagonalized. A similar analysis for the real parameters of doped AFMR's is desirable, but presently challenging for realistic systems because both spin symmetry and translational invariance are broken and the matrices that must be diagonalized are large.

Our results also have important implications for undoped ferric wheels. Recent torque, c_v , and proton $1/T_1$ -measurements [87] on single crystals of various Fe_6 compounds show that these AFMR's could exhibit physics beyond the Hamiltonian Eq. (2.14). One important future step in explaining the new experimental data will be to clarify to which extent the observed phenomena can be attributed to inhomogeneous level broadening. The theoretical framework presented here allows one to calculate analytically the inhomogeneous level broadening resulting from a random distribution of single exchange couplings J' and on-site anisotropies k'_z which could be a consequence of lattice defects in Fe_6 crystals. Indeed, recent work on Mn_{12} suggests that lattice distortions [88] and a distribution of anisotropy energies and g factors [89, 90] could account for the observed broad distribution of tunneling rates in Mn_{12} .

Finally, we stress once more that the Hamiltonian \hat{H} [Eq. (3.11)] discussed here is a simple model Hamiltonian, which still leads to fascinating novel features in the physical properties of the modified AFMR's. However, as discussed

in Sec. 3.2.5, realistic systems might require modification of Eq. (3.11). Generalization of the present approach to more complicated anisotropies is, however, straightforward.

Chapter 4

Quantum computing with spin cluster qubits

We show next that spin clusters with antiferromagnetic intracluster exchange coupling and a finite excess spin allow one to define a qubit. During the past years, the discovery of several powerful quantum algorithms [91] has triggered substantial research efforts aiming at the implementation of a quantum computer in a physical system. The main difficulty is that qubits must be prepared, manipulated, and read out with high fidelity while decoherence is required to remain small [92]. Solid-state implementations of qubits exploit the versatility of nanoscale fabrication, but suffer from decoherence times which are usually shorter than in many quantum optics proposals [93]. Electron [4, 34, 94] and nuclear [95, 35] spins have been identified as promising candidates for qubits in a solid state system. The main advantage of electron or nuclear spins is that they are natural two state systems and that decoherence times for the spin degree of freedom [36, 96] are usually larger than for charge degrees of freedom.

Here we show that a wide variety of spin clusters are promising candidate systems for qubits [97]. Qubits formed by several spins have so far mainly been discussed in the context of exchange-only quantum computing [98, 99, 100], coherence-preserving qubits [101], and quantum computing schemes in which the requirements on the control of exchange interactions between spins are relaxed [102]. However, all these schemes require control at the single-spin level, either with local magnetic fields [102] or exchange interactions [98, 101]. For the spin clusters considered here, control for both magnetic fields and exchange interactions is required only on the length scale of the spin cluster diameter. Initialization and readout of the spin cluster is achieved with the methods developed for single spins [4, 34]. The main advantage of spin clusters is that the requirements on spatial control can be traded for gate operation times.

Any quantum computation can be decomposed into a sequence of one- and

two-qubit quantum gates [103]. For a single-spin qubit, the \hat{s}_z eigenstates $|\uparrow\rangle$ and $|\downarrow\rangle$ are identified as logical basis states $|0\rangle$ and $|1\rangle$, respectively [4, 34]. The phase shift gate can then be realized by a magnetic field $B_z(t)$ and the one-qubit rotation gate U_{rot} by a transverse field $B_x(t)$ which rotates $|\uparrow\rangle$ into $|\downarrow\rangle$ and vice versa. More generally, the equations

$$\langle 0|\hat{H}'|0\rangle = \langle 1|\hat{H}'|1\rangle \text{ and } \langle 1|\hat{H}'|0\rangle \neq 0 \quad (4.1)$$

constitute a sufficient condition that a Hamiltonian \hat{H}' induces the unitary time evolution required for U_{rot} . For single spins, $\hat{H}' = g\mu_B B_x(t)\hat{s}_x$ fulfills Eq. (4.1). Similarly, an exchange interaction $\hat{H}_* = J_*\hat{\mathbf{s}}_1 \cdot \hat{\mathbf{s}}_2$ generates the unitary time evolution required for the square-root of SWAP gate [4] because, in the two-qubit product basis,

$$\langle 10|\hat{H}_*|01\rangle \neq 0. \quad (4.2)$$

In contrast to a single spin $s = 1/2$, clusters formed by n_c coupled spins are not intrinsically two-state systems. In order to prove that a logical qubit can be defined in terms of the energy eigenstates of a spin cluster we will (a) identify spin clusters with a ground state doublet $\{|0\rangle, |1\rangle\}$ separated from the next excited state by an energy gap Δ ; (b) identify Hamiltonians \hat{H}' and \hat{H}_* which satisfy Eqs. (4.1) and (4.2) and, hence, allow one to generate a universal set of quantum gates; and (c) quantify leakage for the spin cluster qubit. In particular, the evaluation of the matrix elements in Eqs. (4.1) and (4.2) and the quantification of excitation out of the computational basis (leakage) requires a detailed characterization of the states $\{|0\rangle, |1\rangle\}$ which is, in general, nontrivial.

This chapter is organized as follows. In Sec. 4.1 we discuss the computational basis states for spin-1/2 chains and show that a qubit can be defined in terms of the energy eigenstates of an antiferromagnetic chain. We derive analytical expressions for the matrix elements in Eqs. (4.1) and (4.2) for various anisotropies and spatially varying intracenter exchange interaction. Section 4.2 discusses the insensitivity of spin cluster qubits to the details of interactions within the cluster, such as the relative placement of spins and the exchange strengths. In Sec. 4.3, spins with spin quantum numbers larger than 1/2 are discussed. In Sec. 4.4, we draw our conclusions.

4.1 Spin chains

For simplicity, we first consider a spin cluster qubit formed by a spin chain,

$$\hat{H} = \sum_{i=1}^{n_c-1} f_j [J_{\perp}(\hat{s}_{j,x}\hat{s}_{j+1,x} + \hat{s}_{j,y}\hat{s}_{j+1,y}) + J_z\hat{s}_{j,z}\hat{s}_{j+1,z}] \quad (4.3)$$

where n_c is odd and $J_\perp, J_z > 0$. The real numbers $f_j > 0$ account for a spatial variation of the exchange interaction, and $J_\perp f_j$ ($J_z f_j$) denotes the transverse (longitudinal) exchange interaction between sites j and $j + 1$.

4.1.1 Isotropic spin chains

For electron spins in quantum dots, the nearest neighbor exchange interaction is usually of the Heisenberg form [34], $J = J_\perp = J_z$. We first consider $f_j \equiv 1$,

$$\hat{H} = J \sum_{j=1}^{n_c-1} \hat{\mathbf{S}}_j \cdot \hat{\mathbf{S}}_{j+1} \quad (4.4)$$

with $J > 0$. Note that this is an open spin chain; a closed spin chain would have a fourfold degenerate ground state multiplet for odd n_c that would make it unsuitable for representing a single qubit. Because the intracluster exchange interaction J is time independent and no external control is required, J can be adjusted already during sample growth.

Spin chains have been studied in great detail during the past decades [104, 105, 106]. The theoretical description of the antiferromagnetic spin chain Eq. (4.4) is particularly challenging because the classical Néel ordered state is not an energy eigenstate and quantum fluctuations of the spins are pronounced. We define the operator of total spin,

$$\hat{S}_\alpha = \sum_{j=1}^{n_c} \hat{S}_{j,\alpha} \quad (4.5)$$

for $\alpha = x, y, z$. Energy eigenstates can be labeled according to their quantum numbers of total spin $\hat{\mathbf{S}}$ and the z -component of total spin, \hat{S}_z , because

$$[\hat{H}, \hat{\mathbf{S}}^2] = [\hat{H}, \hat{S}_z] = 0. \quad (4.6)$$

Due to the antiferromagnetic exchange interaction, states in which the total spin of the chain is minimized are energetically most favorable [107]. For even n_c , the minimum possible spin is $S = 0$, and the system has a nondegenerate ground state. In contrast, for odd n_c , there is a ground state doublet (Fig. 4.1). This parity effect is well known for thermodynamic quantities [108]. The energy gap Δ separating the ground state doublet from the next excited state,

$$\Delta \simeq \frac{J\pi}{2} k_{\min} \sim \frac{J\pi^2}{2n_c}, \quad (4.7)$$

can be estimated from the lower bound of the des Cloiseaux-Pearson spectrum and the minimum wave vector $k_{\min} = \pi/n_c$ [109]. Henceforth, we will restrict our attention to spin chains with odd n_c .

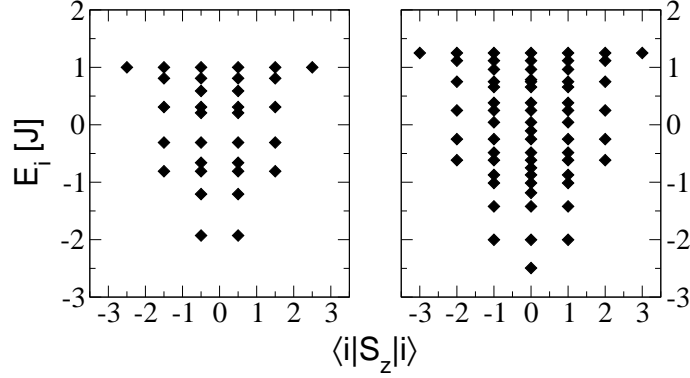


Figure 4.1: Energy spectrum of an isotropic spin chain with $n_c = 5$ (left panel) and $n_c = 6$ (right panel). Energy eigenstates are sorted according to their quantum numbers of \hat{S}_z and their eigenenergies.

The requirements on a candidate system for qubits include initialization of the quantum computer, a universal set of quantum gates, decoherence times long compared to gate operation times, and readout of the qubit [92].

Definition of the spin cluster qubit

For the chain with an odd number of sites [Fig. 4.2(a)], we define the spin cluster qubit in terms of the $S = 1/2$ ground state doublet by

$$\begin{aligned}\hat{S}_z|0\rangle &= \frac{\hbar}{2}|0\rangle, \\ \hat{S}_z|1\rangle &= -\frac{\hbar}{2}|1\rangle.\end{aligned}\quad (4.8)$$

The states $\{|0\rangle, |1\rangle\}$ do not in general have a simple representation in the single-spin product basis, but rather are complicated superpositions of $n_c!/[(n_c - 1)/2]![(n_c + 1)/2]!$ states [Figs. 4.2(b) and (c)] as evidenced by the local magnetization density [Fig. 4.2(d)]. The largest amplitude in this superposition corresponds to the Néel ordered states $|\uparrow\rangle_1|\downarrow\rangle_2\cdots|\uparrow\rangle_{n_c}$ ($|0\rangle$) and $|\downarrow\rangle_1|\uparrow\rangle_2\cdots|\downarrow\rangle_{n_c}$ ($|1\rangle$), respectively. For example, for the simplest nontrivial spin cluster qubit with $n_c = 3$,

$$\begin{aligned}|0\rangle &= \frac{2}{\sqrt{6}}|\uparrow\rangle_1|\downarrow\rangle_2|\uparrow\rangle_3 - \frac{1}{\sqrt{6}}|\uparrow\rangle_1|\uparrow\rangle_2|\downarrow\rangle_3 \\ &\quad - \frac{1}{\sqrt{6}}|\downarrow\rangle_1|\uparrow\rangle_2|\uparrow\rangle_3,\end{aligned}\quad (4.9)$$

and $|1\rangle$ is obtained by flipping all spins. For $n_c = 9$, the Néel configuration has only a 20% probability; the remaining 80% represent quantum fluctuations [see Figs. 4.2(b) and (c)].

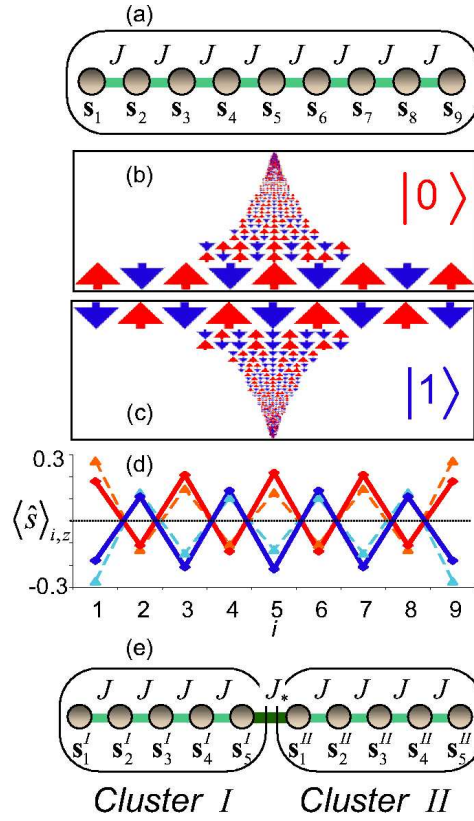


Figure 4.2: Spin cluster qubit. (a) The energy eigenstates of an antiferromagnetic spin chain with an odd number of sites define the spin cluster qubit. (b) Wave function of $|0\rangle$ in the single-spin product basis for $n_c = 9$. The size of each configuration is proportional to the probability of finding the corresponding product state in $|0\rangle$. (c) Similar to (b) but for state $|1\rangle$. (d) Spin density $\langle \psi | \hat{s}_{i,z} | \psi \rangle$ for $|\psi\rangle = |0\rangle$ and $|\psi\rangle = |1\rangle$ (solid lines) for constant intrachain exchange interaction. Dashed lines indicate the corresponding data for a spatially varying intrachain exchange $f_j = \sin(\pi j/n_c)$. (e) Spin cluster qubits are coupled by a switchable interchain exchange interaction $J_*(t)$.

In spite of their complicated representation in the single-spin product basis, $|0\rangle$ and $|1\rangle$ are in many respects very similar to the states $|\uparrow\rangle$ and $|\downarrow\rangle$ of a single spin and, hence, define the computational basis for universal quantum computing with *spin cluster qubits*. The reason for this is that $\{|0\rangle, |1\rangle\}$ belong to one $S = 1/2$ doublet such that

$$\hat{S}^-|0\rangle = \hbar|1\rangle, \quad \hat{S}^+|1\rangle = \hbar|0\rangle, \quad (4.10)$$

where $\hat{S}^\pm = \hat{S}_x \pm i\hat{S}_y$ are the spin ladder operators of the spin chain.

Initialization

Initialization of the spin cluster qubit can be achieved by cooling in a magnetic field with $g\mu_B B_z \ll \Delta$ to temperatures $T \ll g\mu_B B_z/k_B$. The spin cluster will relax to $|0\rangle$ within the spin relaxation time.

Quantum Gate operation

The one-qubit phase shift gate U_ϕ , one-qubit rotation gate U_{rot} , and CNOT gate U_{CNOT} constitute a universal set of quantum gates. According to Eq. (4.10), a magnetic field that is constant over the spin cluster qubit acts on the states of the spin cluster qubit in the same way as on a single-spin qubit. Constant magnetic fields B_z (B_x) effect the one-qubit phase shift (one-qubit rotation) quantum gate without leakage because, due to quantum mechanical selection rules, we have $\langle i|\hat{\mathbf{S}}|0\rangle = \langle i|\hat{\mathbf{S}}|1\rangle = 0$ for any state $|i\rangle \neq |0\rangle, |1\rangle$ outside the ground state doublet. Because $|0\rangle$ and $|1\rangle$ are degenerate and separated from the next excited state by Δ , one-qubit quantum gates can be realized with high fidelity also by any spatially varying magnetic field for which $|\langle 1|\sum_{j=1}^{n_c} g_j \mu_B B_{j,x} \hat{s}_{j,x}|0\rangle| \neq 0$ (U_{rot}) and $\langle 0|\sum_{j=1}^{n_c} g_j \mu_B B_{j,z} \hat{s}_{j,z}|0\rangle \neq 0$ (U_ϕ), respectively. Here, g_j is the electron spin g factor at site j . Such spatially varying fields can potentially cause leakage. However, if $|g_j \mu_B B_j|/\Delta \ll 1$ and if all B_j are switched on and off adiabatically, i.e., on time scales long compared to \hbar/Δ , the quantum gate fidelity is close to 100% as we will discuss in detail in Sec. 4.1.3.

For the CNOT gate, one requires an exchange interaction \hat{H}_* between one or several spins of neighboring spin cluster qubits I and II which can be switched on and off, for example, by electrical gates [4]. The simplest case is an exchange interaction between the outermost spins of neighboring clusters [Fig. 4.2(e)], $\hat{H}_* = J_*(t)\hat{\mathbf{s}}_{n_c}^{\text{I}} \cdot \hat{\mathbf{s}}_1^{\text{II}}$. More generally, any \hat{H}_* of the form

$$\hat{H}_* = J_*(t)\hat{\mathbf{s}}_{n_c}^{\text{I}} \cdot \hat{\mathbf{s}}_1^{\text{II}} + J_*(t) \sum_{j=1}^{n_c-1} (v_j^{\text{I}} \hat{\mathbf{s}}_j^{\text{I}} \cdot \hat{\mathbf{s}}_{j+1}^{\text{I}} + v_j^{\text{II}} \hat{\mathbf{s}}_j^{\text{II}} \cdot \hat{\mathbf{s}}_{j+1}^{\text{II}}). \quad (4.11)$$

translates into an isotropic coupling also in the two-qubit product basis. Here, the factors v_j allow for a spatial variation of the intracluster exchange interactions during gate operation, where $|v_j| < 1$ and $|J_*| \ll J$ is the limit relevant for experiments. \hat{H}_* will in general not only couple states within the two-qubit product basis $\{|00\rangle, |01\rangle, |10\rangle, |11\rangle\}$, but will also lead to leakage. As long as $J_*(t)$ changes adiabatically and $|J_*(t)| \ll \Delta$ for all times, leakage remains small. It should be noted that this adiabaticity condition also holds for single electrons in quantum dots where, however, the energy gap Δ is usually larger than for the spin cluster qubit. The action of \hat{H}_* can then be described by an effective Hamiltonian in the two-qubit product basis,

$$\begin{aligned} \hat{H}_* = & J_{*z}(t)\hat{S}_z^I\hat{S}_z^{II} + \frac{J_{*\perp}(t)}{2}(\hat{S}^{I+}\hat{S}^{II-} + \hat{S}^{I-}\hat{S}^{II+}) \\ & + J_o(t)\mathbf{1}, \end{aligned} \quad (4.12)$$

where the roman numbers label the spin clusters, and

$$\begin{aligned} J_{*z}(t) &= 4J_*(t)|_I\langle 0|\hat{s}_{n_c,z}^I|0\rangle_I||_{II}\langle 0|\hat{s}_{1,z}^{II}|0\rangle_{II}|, \\ J_{*\perp}(t) &= 4J_*(t)|_I\langle 1|\hat{s}_{n_c,x}^I|0\rangle_I||_{II}\langle 1|\hat{s}_{1,x}^{II}|0\rangle_{II}|, \\ J_o(t) &= J_*(t)[_I\langle 0|\sum_{j=1}^{n_c-1}v_j^I\hat{\mathbf{s}}_j^I\cdot\hat{\mathbf{s}}_{j+1}^I|0\rangle_I \\ &\quad +_{II}\langle 0|\sum_{j=1}^{n_c-1}v_j^{II}\hat{\mathbf{s}}_j^{II}\cdot\hat{\mathbf{s}}_{j+1}^{II}|0\rangle_{II}]. \end{aligned} \quad (4.13)$$

For the derivation of Eq. (4.12), see Appendix B.1.

Because, for the isotropic chain,

$${}_I\langle 0|\hat{s}_{n_c,z}^I|0\rangle_I = |{}_I\langle 1|\hat{s}_{n_c,x}^I|0\rangle_I|, \quad (4.14)$$

the coupling \hat{H}_* is isotropic also in the two-qubit product basis and acts on the states $|0\rangle$ and $|1\rangle$ of neighboring spin chains *in the same way as an isotropic exchange interaction between two single spins*. This illustrates the most significant advantage of the spin cluster qubits over single spin qubits – that *it is sufficient to control magnetic fields and exchange interactions on a scale of the spin cluster diameter*. For the linear spin cluster qubit, this length scale is n_c times larger than the original qubit. Two-qubit quantum gates can be effected even with a more general class of coupling Hamiltonians \hat{H}_* . For example, couplings between several spins of cluster I to several spins of cluster II, such as $\hat{H}_* = J_*\sum_{i=1}^{n_c}\hat{\mathbf{s}}_i^I\cdot\hat{\mathbf{s}}_i^{II}$, are permitted and even lead to a decrease of the CNOT gate operation time because the coupling of several spins in the microscopic Hamiltonian leads to an increased effective coupling between the clusters.

For the special cases $J_{*z} = J_{*\perp}$ and $J_{*\perp} = 0$ in Eq. (4.12), an explicit pulse sequence for the CNOT gate has been derived previously in Refs. [4, 110]. We define the unitary time evolution operator $U_*(\pi/2) = \hat{T}_t \exp\left(-i \int dt \hat{H}_*/\hbar\right)$, with $-\int dt J_{*\perp}(t)/\hbar = \pi/2$. Here, \hat{T}_t is the time ordering operator. Then, more generally,

$$U_{\text{CNOT}} \sim e^{-i\pi S_y^{\text{II}}/2} e^{i2\pi \mathbf{n}_1 \cdot \mathbf{S}^{\text{I}}/3} e^{i2\pi \mathbf{n}_2 \cdot \mathbf{S}^{\text{II}}/3} U_*(\pi/2) \\ \times e^{i\pi S_y^{\text{I}}/2} U_*(\pi/2) e^{-i\pi S_x^{\text{I}}/2} e^{-i\pi S_x^{\text{II}}/2} e^{i\pi S_y^{\text{II}}/2} \quad (4.15)$$

is the CNOT gate for an arbitrary effective XXZ-coupling Hamiltonian [Eq. (4.12)] if $J_{*\perp} \neq 0$, where $\mathbf{n}_1 = (1, -1, 1)/\sqrt{3}$ and $\mathbf{n}_2 = (1, 1, -1)/\sqrt{3}$.

The gate operation time for $U_*(\pi/2)$ is limited from below by $h/16J_*|\langle 1|\hat{s}_{n_c,x}^{\text{I}}|0\rangle_{\text{I}}||\langle 1|\hat{s}_{1,x}^{\text{II}}|0\rangle_{\text{II}}|$, where J_* is the maximum value of the inter-cluster exchange coupling. Matrix elements such as $|\langle 1|\hat{s}_{n_c,x}^{\text{I}}|0\rangle_{\text{I}}|$ decrease with increasing n_c , which leads to an increase in gate operation time. For realistic parameters and small n_c (see Sec. 4.1.6 below), J_* is limited by experimental constraints rather than the condition $J_* \ll \Delta$. Then, the increase in gate operation time compared to single-spin qubits is $1/(4|\langle 1|\hat{s}_{n_c,x}^{\text{I}}|0\rangle_{\text{I}}||\langle 1|\hat{s}_{1,x}^{\text{II}}|0\rangle_{\text{II}}|)$ and depends only on the matrix elements of the spin operators. Similarly, for a given magnetic field, the increase of the time required for a one-qubit rotation depends only on the matrix elements $|\langle 1|\hat{s}_{j,x}|0\rangle|$.

Decoherence

For spin clusters, decoherence usually is faster than for single spins. The scaling of the decoherence time τ_ϕ with system size depends on the microscopic decoherence mechanism. For electron spins in quantum dots, fluctuating fields and nuclear spins have been identified as dominant sources [4, 34, 111, 112]. In order to obtain analytical estimates for the scaling of τ_ϕ with n_c , we restrict our analysis to a heuristic model in which decoherence is effected by a fluctuating classical field,

$$\hat{H}^B = b(t)\hat{S}_z. \quad (4.16)$$

The decoherence rate is obtained from [113]

$$\frac{1}{\tau_\phi} = \pi \sum_{|k\rangle \neq |0\rangle} |\langle k|\hat{S}_z|0\rangle|^2 C(E_k - E_0) \\ + \pi \sum_{|k\rangle \neq |1\rangle} |\langle k|\hat{S}_z|1\rangle|^2 C(E_k - E_1) \\ + \pi(\langle 0|\hat{S}_z|0\rangle - \langle 1|\hat{S}_z|1\rangle)^2 C(0), \quad (4.17)$$

where

$$C(E) = \frac{1}{2\pi} \int_{-\infty}^{\infty} dt e^{iEt/\hbar} \langle b(t)b(0) \rangle \quad (4.18)$$

is the spectral density of the random field in Eq. (4.16). Because of Eq. (4.8), we find that the decoherence rate $1/\tau_\phi = \pi C(0)$ is independent of n_c . This can be traced back to the fact that only the total magnetic moment couples to the fluctuating field and the magnetic moment $\pm g\mu_B/2$ of the spin cluster qubit is identical to the one of a single spin. For a non-diagonal coupling $\hat{H}^B = b(t)\hat{S}_x$, from Eq. (4.17) we find $1/\tau_\phi = \pi C(0)/2$.

Decoherence due to the coupling to nuclear spins is a complicated theoretical problem in its own right [111, 112]. In order to obtain an estimate for the scaling of the decoherence time with spin cluster size, we only consider fluctuating classical fields acting independently on each site of the spin cluster,

$$\hat{H}^B = \sum_{j=1}^{n_c} b_j(t) \hat{s}_{j,z}, \quad (4.19)$$

where $\langle b_i(t)b_j(0) \rangle \propto \delta_{ij}$. For Gaussian white noise with

$$\langle b_i(t)b_j(0) \rangle = 2\pi\gamma^B \delta_{ij} \delta(t), \quad (4.20)$$

the decoherence rate $1/\tau_\phi$ then scales linearly with n_c .

Readout

Readout of the spin cluster qubit could be achieved by readout of all spins within the cluster [37]. Because $\langle 0 | \sum_{i=1}^{n_c} \hat{s}_{i,z} | 0 \rangle = \hbar/2$ and $\langle 1 | \sum_{i=1}^{n_c} \hat{s}_{i,z} | 1 \rangle = -\hbar/2$, this will allow one to unambiguously determine the state of the cluster qubit. However, the state of the cluster determines the local spin density at each site [Fig. 4.2(d)], and a probabilistic readout is possible also by measurement of single spins only. For example, for $n_c = 9$, if the measurement of the central spin of the chain yields $+\hbar/2$, the spin cluster qubit has been in state $|0\rangle$ with a probability of 70%. A selective readout of several spins of the spin cluster qubit would also reduce the requirements on the readout sensitivity. For example, the sublattice spin $\langle 0 | \hat{s}_{1,z} + \hat{s}_{3,z} + \hat{s}_{5,z} + \hat{s}_{7,z} + \hat{s}_{9,z} | 0 \rangle \simeq \hbar$ for $n_c = 9$ is twice as large as the total magnetic moment $\langle 0 | \hat{S}_z | 0 \rangle$ and could be measured after separating the electron spins at even and odd sites of the cluster.

4.1.2 Varying exchange constants

The formation of a spin cluster qubit from an odd number of antiferromagnetically coupled spins requires little control over intracluster exchange constants.

Although both the energy gap Δ and matrix elements such as $\langle 1|\hat{s}_{j,x}|0\rangle$ depend on the spatial variation of exchange constants, the general principle of assembling several spins into a cluster qubit remains valid.

In order to demonstrate the robustness of our spin cluster qubit against a variation of exchange constants, we return to the isotropic spin chain but now allow for varying f_j in Eq. (4.3). Because the isotropic spin chain still exhibits a $S = 1/2$ ground state doublet [107], quantum computing is possible as discussed for $f_j \equiv 1$ in Sec. 4.1.1. From an experimental point of view, a priori knowledge of the factors f_j is not necessary for quantum computing. Rather, the relevant matrix elements such as $|\langle 1|\hat{s}_{j,x}|0\rangle|$ can be determined experimentally. Similarly, a quantum computer could even be assembled from spin cluster qubits which are not identical.

If the exchange constants can be controlled during sample growth, the properties of the spin cluster qubit can be engineered to a certain extent. For clusters with centrosymmetric exchange constants, the time required to perform the square-root of swap gate $U_*(\pi/2)$ for given J_* increases with $1/|\langle 0|\hat{s}_{1,z}|0\rangle|^2$. For $n_c = 9$ and $f_j \equiv 1$, $|\langle 0|\hat{s}_{1,z}|0\rangle| \simeq 0.18$ corresponding to an increase in the gate operation time for $U_*(\pi/2)$ by a factor $(0.5/0.18)^2 \simeq 7.7$ compared to the single-spin qubit for given J_* . However, by tuning the outermost couplings to small values,

$$\lim_{f_1=f_{n_c-1} \rightarrow 0} |\langle 0|\hat{s}_{1,z}|0\rangle| = 1/3. \quad (4.21)$$

This corresponds to an increase in the gate operation time for $U_*(\pi/2)$ by a factor 2.3 compared to the single-spin qubit for given J_* .

We next prove Eq. (4.21). The local spin density in the energy eigenstates of Eq. (4.3) depends sensitively on spatial variations of the exchange interaction [Fig. 4.2(b)]. Whereas for $f_j \equiv 1$ (solid lines) the magnetization density in each of the sublattices increases toward the center of the chain [114], the opposite behavior is observed for an exchange interaction $f_j = \sin(j\pi/n_c)$ (dashed lines). In the limit $f_1 = f_{n_c-1} \rightarrow 0$, the increase of local spin density toward the ends of the chain can be understood quantitatively. The ground state doublet of the spin cluster qubit can be constructed explicitly from the ground state doublet $\{|0\rangle_{n_c-2}, |1\rangle_{n_c-2}\}$ of the chain with the outermost spins removed. For Jf_1 much smaller than the energy gap Δ_{n_c-2} of the chain formed by the $n_c - 2$ central spins, the coupling of the outermost spins can be treated perturbatively. For a centrosymmetric chain with $f_j = f_{n_c-j}$, from the ansatz

$$\begin{aligned} |0\rangle &= \alpha_1 |\uparrow\rangle|1\rangle_{n_c-2}|\uparrow\rangle + \alpha_2 |\uparrow\rangle|0\rangle_{n_c-2}|\downarrow\rangle \\ &\quad + \alpha_3 |\downarrow\rangle|0\rangle_{n_c-2}|\uparrow\rangle + \mathcal{O}(Jf_1/\Delta_{n_c-2}) \end{aligned} \quad (4.22)$$

we find $(\alpha_1, \alpha_2, \alpha_3) = (2, -1, -1)/\sqrt{6}$ for the ground state of the chain with n_c spins and, hence, Eq. (4.21).

4.1.3 Leakage

We next discuss in more detail the one qubit rotation gate induced by a transverse magnetic field in order to quantify leakage.

Because $\hat{S}_x|0\rangle = (\hbar/2)|1\rangle$ and $\hat{S}_x|1\rangle = (\hbar/2)|0\rangle$, a magnetic field that is uniform over the spin cluster acts on the spin cluster qubit in the same way as on a single spin $s = 1/2$. In particular, the Hamiltonian

$$\hat{H}' = g\mu_B B_x(t)\hat{S}_x \quad (4.23)$$

induces a coherent rotation from $|0\rangle$ to $|1\rangle$ without leakage, as implied by quantum mechanical selection rules. The gate operation time for a rotation by ϕ is determined by $\int_0^t dt' g\mu_B B_x(t')/\hbar = \phi$ and is identical to the one for single spins. In contrast, the one-qubit rotation effected by a spatially varying magnetic field

$$\hat{H}' = \sum_{j=1}^{n_c} g_j\mu_B B_{j,x}(t)\hat{s}_{j,x} \quad (4.24)$$

will in general lead to leakage because of finite matrix elements $\langle i|\hat{H}'|0\rangle \neq 0$ and $\langle i|\hat{H}'|1\rangle \neq 0$ coupling the computational basis to higher excited states $|i\rangle \neq |0\rangle, |1\rangle$. The adiabatic theorem guarantees that leakage remains small if the Fourier transform of $B_{j,x}$ vanishes for frequencies larger than Δ/\hbar . Even if this adiabaticity requirement is not met, admixing of higher excited states to $\{|0\rangle, |1\rangle\}$ is controlled by the parameters $g_j\mu_B B_{j,x}/\Delta$ and remains small if $|g_j\mu_B B_{j,x}| \ll \Delta$ for all j .

In the following, we concentrate on $n_c = 5$ spins. As shown in Fig. 4.3(a) and Fig. 4.4, a magnetic field constant over the cluster coherently rotates $|0\rangle$ into $|1\rangle$. This is also evidenced by the in-phase rotation of all spins. In order to illustrate that also a spatially inhomogeneous field can induce the one-qubit rotation with high gate fidelity, we now consider a magnetic field $B_{3,x}$ acting only on the central spin ($j = 3$) of the cluster. The field is switched on instantaneously at $t = 0$. For $t > 0$, the time evolution is then governed by the sum of the time-independent Hamiltonian of the spin cluster, \hat{H} , and the Zeeman Hamiltonian $\hat{H}' = g\mu_B B_{3,x}\hat{s}_{3,x}$. In Fig. 4.4(a), for an initial state $|\psi(t=0)\rangle = |0\rangle$, we plot the projection of the state $|\psi(t)\rangle$ onto the qubit basis states for $g\mu_B B_{3,x}/J = 0.1$ (dashed line, coinciding with the solid line on this scale) and 0.5 (dashed-dotted line), respectively. The time evolution is obtained by numerical integration of the Schrödinger equation. For small $g\mu_B B_{3,x} \ll \Delta \simeq 0.72J$, the spatially inhomogeneous field rotates $|0\rangle$ into $|1\rangle$ with high fidelity. The gate fidelity $|\langle 1|U_{\text{rot}}|0\rangle|^2$ decreases from 99.8% ($g\mu_B B_x/J = 0.1$) to 93.4% for $g\mu_B B_x = 0.5J$, where the typical energy scale of \hat{H}' becomes comparable to Δ . Here, $U_{\text{rot}} = \hat{T}_t \exp\left(-i \int_0^{t_{\text{max}}} dt (\hat{H} + \hat{H}')/\hbar\right)$ with $t_{\text{max}} = \hbar/(4|\langle 1|\hat{s}_{x,3}|0\rangle|g\mu_B B_x)$ describes the time evolution during a π -rotation.

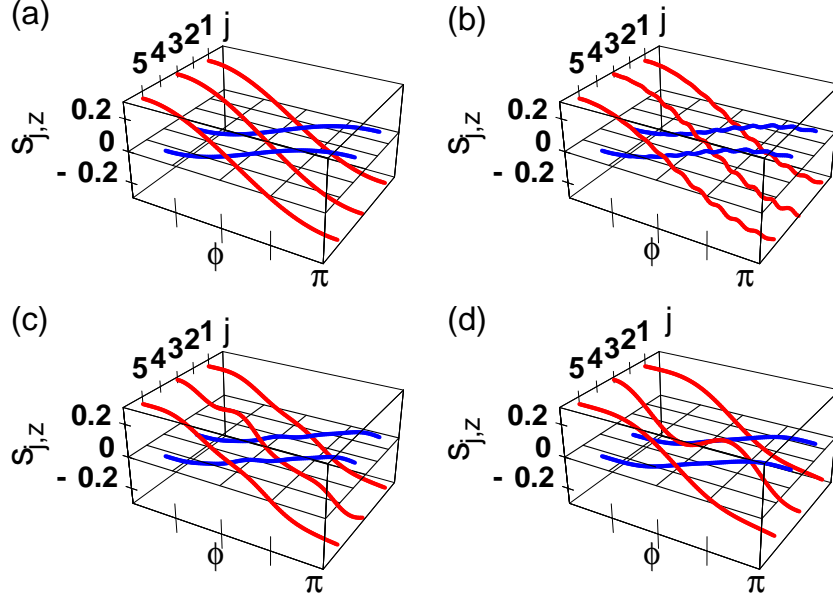


Figure 4.3: Local spin density for all sites j of a spin chain with $n_c = 5$ as a function of time ($\phi \propto t$) during the one-qubit rotation gate. (a) A magnetic field constant over the cluster, $\hat{H}' = g\mu_B B_x \hat{S}_x$, coherently rotates $|0\rangle$ into $|1\rangle$ without leakage. Here, $\phi = g\mu_B B_x t/\hbar$. The coherent rotation is evidenced by the in-phase rotation of all spins. (b)–(d) An inhomogeneous magnetic field, $\hat{H}' = g\mu_B B_{3,x} \hat{s}_{3,x}$, effects the one-qubit rotation gate with high gate fidelity if $|g\mu_B B_{3,x}| \ll \Delta$. Here, $\phi = g\mu_B B_{3,x} t(2|\langle 1|\hat{s}_{3,x}|0\rangle|)/\hbar$. The gate fidelity decreases from 99.8% to 93.4% and 78.5% for increasing $g\mu_B B_{3,x} = 0.1J$ (b), $0.5J$ (c), and $1J$ (d), respectively. In the local spin density, leakage is evidenced by high-frequency oscillations of neighboring spins, i.e., the excitation of magnons.

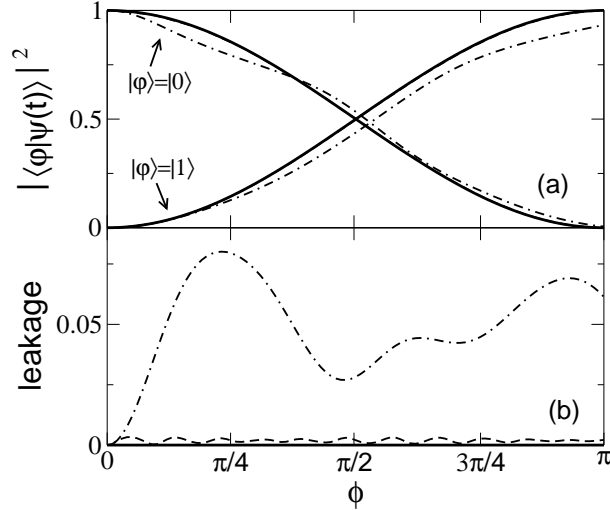


Figure 4.4: Time evolution of a state $|\psi(t)\rangle$ with $|\psi(0)\rangle = |0\rangle$ during the one-qubit rotation induced by a spatially constant magnetic field (solid line) and a magnetic field acting only on the central spin of the cluster (dashed and dashed-dotted lines) for $n_c = 5$ as a function of time, $\phi \propto t$. The constant magnetic field effects the quantum gate with 100% fidelity. In order to illustrate the effect of leakage with increasing Zeeman energy for a spatially inhomogeneous field, $\hat{H}' = g\mu_B B_{3,x} \hat{s}_{3,x}$, we assume that \hat{H}' is switched on instantaneously at $t = 0$. (a) For $g\mu_B B_{3,x} = 0.1J$ (dashed line), the inhomogeneous magnetic field still effects the one-qubit rotation with 99.8% fidelity. (b) Leakage out of the computational basis, $1 - (|\langle 0 | \psi(t) \rangle|^2 + |\langle 1 | \psi(t) \rangle|^2)$, remains smaller than 0.3%. In contrast, for $g\mu_B B_{3,x} = 0.5J$ (dashed-dotted lines), i.e., comparable to $\Delta \simeq 0.72J$, the fidelity is only 93.4% and leakage is of order 7%.

The decrease in gate fidelity with increasing $B_{3,x}$ can be understood from the local spin densities [Figs. 4.3(b) – (d)]. Although only the central spin is acted on by $B_{3,x}$, for $|g\mu_B B_{3,x}| \ll \Delta$ all spins of the spin cluster corotate with the central spin due to the exchange field. The condition $|g\mu_B B_{3,x}| \ll \Delta$ guarantees that the externally induced rotation of the central spin is sufficiently slow that all spins of the chain corotate in phase. For $|g\mu_B B_{3,x}|$ of order Δ , the rotation of the central spin induced by $B_{3,x}$ is too fast for the remaining spins of the chain to follow in phase [see, e.g., Fig. 4.3(c) for short times, $\phi \ll 1$]. The spins of the chain no longer rotate in phase and magnons are excited [Fig. 4.4(b)]. Quantum gate operation probes the spin dynamics in real time and, hence, may provide new insight into the low-energy physics of spin chains.

That leakage is controlled by the parameter $|g\mu_B B_{3,x}|/\Delta$ can be traced back to the existence of a ground state doublet. In contrast, for a chain with ferromagnetic exchange coupling $J < 0$ in Eq. (4.4), the ground state has degeneracy $n_c + 1$. Although a computational basis could be defined also in terms of a subset of the ground state multiplet for $J < 0$, due to the $n_c + 1$ -fold degeneracy the system is more prone to leakage than the antiferromagnetic systems considered here.

We next quantify leakage for the CNOT gate with the sequence given in Eq. (4.15) by numerical integration of the Schrödinger equation for two spin-cluster qubits with $n_c = 3$ and constant intracluster exchange interaction J . Magnetic fields are assumed to be constant over the clusters, and the clusters are coupled by $\hat{H}_* = J_*(t)\hat{\mathbf{S}}_3^I \cdot \hat{\mathbf{S}}_1^H$. For simplicity, we consider the case that magnetic fields and J_* are switched instantaneously from 0 to finite values $B = 0.1J/g\mu_B$ and $J_* = 0.1J$, respectively. The projections of a two-qubit product state $|\psi(t)\rangle$ onto each of the four basis states during the pulse sequence in Eq. (4.15) are shown in Fig. 4.5 for the initial states $|\psi(0)\rangle = |00\rangle$ and $|\psi(0)\rangle = |10\rangle$. The probabilities and phases (not shown) prove that, indeed, $|00\rangle \rightarrow |00\rangle$ and $|10\rangle \rightarrow |11\rangle$ with a high efficiency. Leakage induced by \hat{H}_* is small for $J_* \ll \Delta$ because all spins in the clusters corotate although \hat{H}_* only couples the outermost spins. For the parameters chosen for Fig. 4.5, leakage due to instantaneous switching of $J_*(t)$ is 0.7% for the complete sequence.

4.1.4 XY-like chains

We next turn to anisotropic chains, $J_\perp \neq J_z$. For odd n_c , the spectrum still exhibits a ground state doublet of \hat{S}_z eigenstates with eigenvalues $\pm\hbar/2$, respectively. However, $\hat{\mathbf{S}}^2$ is no longer a good quantum number. Both for $J_\perp \gg J_z$ (XY-like systems) and $J_\perp \ll J_z$ (Ising-like systems), $|0\rangle$ and $|1\rangle$ can be explicitly constructed.

We first consider the XY model, $J_z = 0$ in Eq. (4.3). By the Jordan-Wigner transformation [47], the XY chain is mapped onto a system of noninteracting

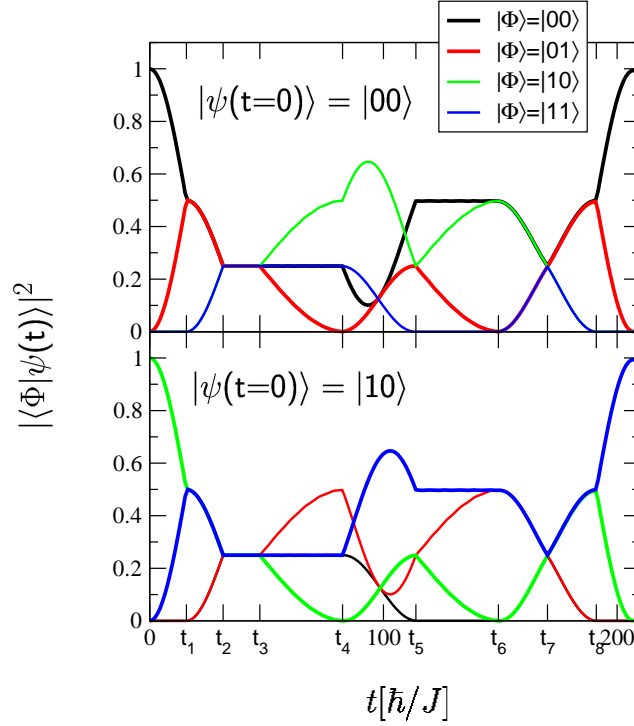


Figure 4.5: CNOT gate for two small spin cluster qubits ($n_c = 3$) obtained by numerical integration of the Schrödinger equation [see Fig. 4.2(e)]. The plotted probabilities and the phases (not displayed) show that (a) $|00\rangle \rightarrow |00\rangle$ and (b) $|10\rangle \rightarrow |11\rangle$. We have chosen a pulse sequence [Eq. (4.15)] with instantaneous switching (at times t_i), $B = 0.1J/g\mu_B$, and $J_* = 0.1J$. Leakage due to instantaneous switching (0.7% for our parameters) can be reduced by decreasing J_* and B .

spinless fermions on a lattice with spatially varying hopping amplitudes,

$$\hat{H} = -\frac{J_{\perp}}{2} \sum_{j=1}^{n_c-1} f_j (\hat{\psi}_{j+1}^{\dagger} \hat{\psi}_j + \hat{\psi}_j^{\dagger} \hat{\psi}_{j+1}), \quad (4.25)$$

where

$$\hat{\psi}_j = \exp \left[i\pi \sum_{k=1}^{j-1} \left(\hat{s}_{k,z} + \frac{1}{2} \right) \right] \hat{s}_j^{-} \quad (4.26)$$

annihilates a Jordan-Wigner fermion at site j . The problem is thus reduced to calculating the one-particle eigenenergies and eigenstates of Eq. (4.25). The one-particle Hamiltonian has $(n_c - 1)/2$ pairs of states with negative and positive energy $\mp E_i$, respectively, which are related to each other by staggering of the wave function,

$$\mathbf{e}_i^{\pm} = (e_{i,1}, \pm e_{i,2}, e_{i,3}, \pm e_{i,5}, \dots), \quad (4.27)$$

where $e_{i,j}$ are real numbers. In addition, there is one eigenstate

$$\mathbf{e}_0 \propto \left(1, 0, -\frac{f_1}{f_2}, 0, \frac{f_1 f_3}{f_2 f_4}, 0, \dots, \pm \frac{f_1 f_3 \dots f_{n_c-2}}{f_2 f_4 \dots f_{n_c-1}} \right) \quad (4.28)$$

with energy eigenvalue 0. The ground state doublet of the XY chain corresponds to the lowest $(n_c - 1)/2$ and $(n_c + 1)/2$ Jordan-Wigner fermion levels filled. Similarly to the spin chain with isotropic exchange interaction, one-qubit gates can be realized by magnetic fields $B_z(t)$ and $B_x(t)$. By numerical exact diagonalization of small spin chains ($n_c = 9$), we have shown that $|\langle 1 | \hat{S}_x | 0 \rangle|$ remains of order 1/2 for various set of f_j [e.g., $f_j \equiv 1$, $f_j = \sin(j\pi/n_c)$], such that the operation time for the one-qubit rotation gate is only limited by \hbar/Δ . An isotropic interqubit coupling Hamiltonian of the form Eq. (4.11) still translates into the effective Hamiltonian in Eq. (4.12). With Eqs. (4.27) and (4.28), from the completeness relation $\sum_{i=1}^{(n_c-1)/2} (e_{i,j}^{+2} + e_{i,j}^{-2}) + e_{0,j}^2 = 1$ for $j = 1, \dots, n_c$ and $\hat{s}_{j,z} = \hat{\psi}_j^{\dagger} \hat{\psi}_j - 1/2$, one can calculate all matrix elements entering the effective coupling Hamiltonian Eq. (4.12),

$$\langle 0 | \hat{s}_{1,z} | 0 \rangle = \frac{e_{0,1}^2}{2}, \quad (4.29)$$

$$|\langle 1 | \hat{s}_{1,x} | 0 \rangle| = \frac{e_{0,1}}{2}, \quad (4.30)$$

where $e_{0,1}$ is the first component of the normed one-particle eigenstate defined in Eq. (4.28). In particular, for $f_j \equiv 1$, $\langle 0 | \hat{s}_{1,z} | 0 \rangle = 1/(n_c + 1)$ and $|\langle 1 | \hat{s}_{1,x} | 0 \rangle| = 1/\sqrt{2(n_c + 1)}$. Due to the anisotropy of the intrachain exchange interaction, \hat{H}_{*} (which is isotropic in the single-spin operators) translates into an effective

XXZ-Hamiltonian in the two-qubit product basis. Nevertheless, the CNOT gate can still be realized according to Eq. (4.15). For the anisotropic chain, a magnetic field applied along an axis \mathbf{n} translates into a rotation around the axis $(n_x, n_y, n_z/2|\langle 1|\hat{S}_x|0\rangle|)$ in the Hilbert space spanned by $\{|0\rangle, |1\rangle\}$,

$$\begin{aligned}\hat{H}' &= g\mu_B B \mathbf{n} \cdot \hat{\mathbf{S}} \\ &\simeq g\mu_B B |\langle 1|\hat{S}_x|0\rangle| [n_x(|0\rangle\langle 1| + |1\rangle\langle 0|)/2 \\ &\quad + n_y i(|1\rangle\langle 0| - |0\rangle\langle 1|)/2] \\ &\quad + g\mu_B B n_z (|0\rangle\langle 0| - |1\rangle\langle 1|)/2.\end{aligned}\tag{4.31}$$

A one-qubit rotation around an arbitrary axis hence requires appropriate rescaling of \mathbf{B} . For example, the rotation corresponding to $\exp(i2\pi\mathbf{n}_1 \cdot \mathbf{S}^I/3)$ [Eq. (4.15)] for the isotropic chain can be achieved by applying a magnetic field $B = B_0(1 + 2/(2|\langle 1|\hat{S}_x|0\rangle|)^2)^{1/2}/\sqrt{3}$ along the axis $\propto (1, -1, 2|\langle 1|\hat{S}_x|0\rangle|)$ for a time $2\pi\hbar/3g\mu_B B_0$. For given J_* and B , the CNOT gate operation time increases at most linearly with n_c .

4.1.5 Ising-like chains

In the Ising limit $J_z \gg J_\perp$ the ground state doublet

$$\begin{aligned}|0\rangle &= |\uparrow\rangle_1 |\downarrow\rangle_2 \dots |\uparrow\rangle_{n_c} + \mathcal{O}(J_\perp/J_z), \\ |1\rangle &= |\downarrow\rangle_1 |\uparrow\rangle_2 \dots |\downarrow\rangle_{n_c} + \mathcal{O}(J_\perp/J_z)\end{aligned}\tag{4.32}$$

is separated from the next excited state by an n_c -independent $\Delta \sim J_z \min(f_j)$. In perturbation theory in J_\perp/J_z , for $f_j \equiv 1$, the matrix elements

$$\begin{aligned}|\langle 1|\hat{S}_x|0\rangle| &\simeq \frac{n_c + 1}{4} \left(\frac{2J_\perp}{J_z}\right)^{(n_c-1)/2}, \\ |\langle 1|\hat{s}_{1,x}|0\rangle| &\simeq \frac{1}{2} \left(\frac{2J_\perp}{J_z}\right)^{(n_c-1)/2}\end{aligned}\tag{4.33}$$

decrease exponentially with system size because \hat{S}_x and $\hat{s}_{1,x}$ only flip one spin within the chain. Expanding the states $|0\rangle$ and $|1\rangle$ in powers of J_\perp/J_z it follows that finite matrix element of $\hat{s}_{1,x}$ and \hat{S}_x between $|0\rangle$ and $|1\rangle$ occur only in order $(n_c - 1)/2$ in J_\perp/J_z [115]. Even for medium sized chains $n_c \gtrsim 9$ and $J_\perp/J_z < 0.2$, an isotropic interqubit coupling Hamiltonian \hat{H}_* translates into an effective Hamiltonian Eq. (4.12) of Ising form (Fig. 4.6). Because of the long gate operation times implied by Eq. (4.33) for the one-qubit rotation and, in particular, the CNOT gate, only quantum computing schemes which require a small number of such operations [116] appear feasible.

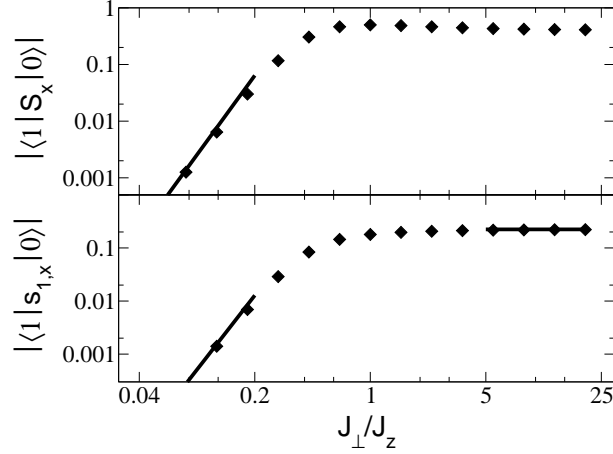


Figure 4.6: Transition matrix elements $|\langle 1|\hat{S}_x|0\rangle|$ and $|\langle 1|\hat{s}_{1,x}|0\rangle|$ as a function of exchange anisotropy ($J_\perp \neq J_z$). The matrix elements determine gate operation times for the one-qubit rotation and CNOT gate. Diamonds show numerical results obtained for $n_c = 9$ and constant exchange interaction, $f_j \equiv 1$ in Eq. (4.3), in comparison with analytical results (solid lines) [see Eq. (4.33)].

In Fig. 4.6, for a chain with $n_c = 9$, we compare our analytical results (solid lines) for the matrix elements $|\langle 1|\hat{S}_x|0\rangle|$ and $|\langle 1|\hat{s}_{1,x}|0\rangle|$ as functions of anisotropy with exact diagonalization for the chain with $f_j \equiv 1$ (symbols). Because matrix elements of order unity imply quantum gate operation times comparable to single spins, the results in Fig. 4.6 show that universal quantum computing based on a sequence of one-qubit rotation and CNOT gates is feasible for a wide range of spin cluster qubits.

4.1.6 Experimental realization

We illustrate the advantages of a spin cluster qubit formed by $n_c = 5$ spins $s = 1/2$ in a one-dimensional array of quantum dots with diameter $d \simeq 50$ nm. For realistic parameters [34] ($J \simeq 10 Kk_B$, $J_* \simeq 2.3 Kk_B$, $g\mu_B B \simeq 0.7 Kk_B$) and a magnetic field which decreases from its maximum values B_x at the central site of the chain to $0.2B_x$ at sites $j = 2, 4$, the operation time for one-qubit gates increases by a factor $1/2|\langle 1|0.2\hat{s}_{2,x} + \hat{s}_{3,x} + 0.2\hat{s}_{4,x}|0\rangle| \simeq 2.2$ compared to a single spin. The operation time for the square-root of SWAP gate is increased by a factor of $1/(2|\langle 0|\hat{s}_{1,z}|0\rangle|)^2 \simeq 4$ compared to the single-spin qubit. However, the operation time for the CNOT gate as defined in Eq. (4.15) is mainly determined by the single-qubit operations of the sequence. Hence, for the minimum operation time of the CNOT gate we find 386 ps for spin clusters instead of 165 ps for single spins. The decrease of decoherence time strongly depends on the mi-

microscopic origin of decoherence. From the heuristic argument in Sec. 4.1.1 we find that the decoherence rate due to globally fluctuating magnetic fields does not scale with n_c and is equal to the one of the single-spin qubit. Decoherence caused by fluctuating local fields scales linearly with n_c . For a spin cluster qubit with $n_c = 5$, we estimate that the number of quantum gates which can be performed during the decoherence time decreases by at most a factor of 10 compared to the single-spin qubit. However, in contrast to single-spin qubits, magnetic fields and exchange constants must be controlled only over length scales $n_c d = 250$ nm and $2n_c d = 500$ nm, respectively instead of $d = 50$ nm. This would allow one to control the exchange between neighboring clusters optically [94]. Note that, for the small clusters analyzed here, Δ is so large that neither adiabaticity nor the requirement that the Zeeman energy and J_* be small compared to Δ provides a serious restriction on quantum gate operation times.

4.2 Spin clusters in $d > 2$

So far, our considerations have been restricted to spin chains. The main ideas discussed above apply to a much larger class of antiferromagnetic systems with uncompensated sublattices. We illustrate next that quantum gates are feasible also if spins $s = 1/2$ are arranged in a two- or three-dimensional cluster. For definiteness, we restrict our attention to an isotropic exchange interaction $J > 0$.

4.2.1 Bipartite lattices

We first consider an odd number of spins arranged on a bipartite lattice with the number of sublattice sites differing by 1, for example, a rectangular lattice with $L_1 \times L_2$ sites, where $L_{1,2}$ are odd. This two-dimensional lattice exhibits a ground state doublet [107]. Similarly to the spin chain, the computational basis $\{|0\rangle, |1\rangle\}$ can be defined in terms of the \hat{S}_z -eigenstates of the ground state doublet. Here, $\hat{\mathbf{S}}$ is the operator of total spin of the two-dimensional array. From a spin-wave ansatz for the elementary excitations, the energy gap Δ separating the ground state doublet from the next excited state can be estimated as

$$\Delta \simeq \frac{J\pi}{\min(L_1, L_2)}. \quad (4.34)$$

Because the characteristic features of the ground state doublet carry over from the one- to the two-dimensional spin cluster qubit, quantum computing with two-dimensional spin arrays on bipartite lattices is possible with the techniques discussed in Sec. 4.1.1. Gate operation times are determined by the matrix elements $|\langle 0|\hat{s}_{j,z}|0\rangle| = |\langle 1|\hat{s}_{j,x}|0\rangle|$. For the 3×3 -lattice shown in Fig. 4.7(a),

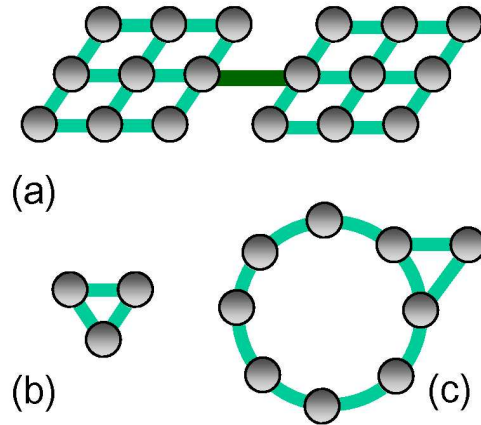


Figure 4.7: Two-dimensional spin clusters. Each dot represents a single-spin qubit. (a) The spin cluster qubit scheme is readily extended from spin chains to any bipartite lattice. (b) Spin arrays with frustrated bonds have a highly degenerate ground state (fourfold degeneracy for three spins). (c) If the frustrated bonds are part of a larger array, the high degeneracy is usually lifted and a ground state doublet remains.

from exact diagonalization we find $\langle 0 | \hat{s}_{j,z} | 0 \rangle = 0.15$ for sites j in the center of the edges, $\langle 0 | \hat{s}_{j,z} | 0 \rangle = 0.23$ for sites j at the corners, and $\langle 0 | \hat{s}_{j,z} | 0 \rangle = 0.17$ for the central site of the cluster. Similarly to the spin chain, the ground state doublet is robust against a spatial variation in the exchange constants as long as all exchange constants remain antiferromagnetic.

4.2.2 Geometrically frustrated systems

For non-bipartite lattices, a ground-state doublet is not guaranteed to emerge. The simplest example is the geometrically frustrated system of three spins $s = 1/2$ shown in Fig. 4.7(b),

$$\begin{aligned} \hat{H} &= J(\hat{\mathbf{s}}_1 \cdot \hat{\mathbf{s}}_2 + \hat{\mathbf{s}}_1 \cdot \hat{\mathbf{s}}_3 + \hat{\mathbf{s}}_2 \cdot \hat{\mathbf{s}}_3) \\ &= \frac{J}{2} \left(\hat{\mathbf{S}}^2 - \frac{9}{4} \right), \end{aligned} \quad (4.35)$$

which has a fourfold degenerate ground state with energy eigenvalue $E = -0.75J$. The eigenstates can be chosen as

$$\begin{aligned}
 |0\rangle &= (|\uparrow\uparrow\downarrow\rangle - |\uparrow\downarrow\uparrow\rangle)/\sqrt{2}, \\
 |1\rangle &= (|\downarrow\uparrow\downarrow\rangle - |\downarrow\downarrow\uparrow\rangle)/\sqrt{2}, \\
 |2\rangle &= (2|\uparrow\uparrow\downarrow\rangle - |\downarrow\uparrow\downarrow\rangle - |\downarrow\downarrow\uparrow\rangle)/\sqrt{6}, \\
 |3\rangle &= (2|\downarrow\uparrow\uparrow\rangle - |\uparrow\uparrow\downarrow\rangle - |\uparrow\downarrow\uparrow\rangle)/\sqrt{6}.
 \end{aligned} \tag{4.36}$$

As demonstrated in Ref. [117], these states could still define a logical qubit robust against certain sources of decoherence. However, quantum gate operation would always require control over single exchange interactions or local magnetic fields and exclude quantum computing with control parameters which vary slowly in space.

Geometrical frustration does, however, not in general rule out the existence of a ground state doublet. In the more generic case that geometrically frustrated bonds are part of a larger system [Fig. 4.7(c)] or the exchange constants in Fig. 4.7(b) are not all equal, a ground state doublet emerges. In this case, the logical states of the spin cluster qubit again can be defined in terms of the \hat{S}_z eigenstates of the ground state doublet and quantum gate operation is possible with magnetic fields and exchange constants varying slowly over the cluster. For systems as shown in Fig. 4.7(c), in which some bonds are frustrated, Δ is usually smaller than in the case of bipartite lattices. For example, for Fig. 4.7(c), $\Delta = 0.157J$ compared to $\Delta = 0.991J$ for Fig. 4.7(a). According to the adiabaticity requirement, the small gap limits gate operation times more severely for the system in Fig. 4.7(c).

4.2.3 Experimental realization

Because spin cluster qubits emerge also in two-dimensional regular spin arrays, spin cluster qubits can be arranged in a plane if the positions of single spins can be controlled as, e.g., for lateral quantum dots [Fig. 4.7(a)]. For a spin cluster qubit formed by $L \times L = n_c$ quantum dots, $\Delta \propto 1/L$. Decoherence due to globally fluctuating fields does not increase with n_c , whereas independent local Gaussian noise gives rise to a decoherence rate $1/\tau_\phi \propto n_c$. Two-dimensional spin cluster qubits are hence particularly interesting for qubits in which decoherence is induced mainly by global rather than local fluctuating fields.

More importantly, a spin cluster qubit can be defined even for a wide range of systems in which the positions and exchange constants cannot be accurately controlled. For P atom electron spins in a Si matrix, because of rapid oscillations of the exchange coupling between atoms at large distances, placement of atoms with lattice spacing precision is required for single-spin qubits [118]. Without this precision, the exchange interaction at large distances vanishes

with a probability of 50%. In contrast, for spin cluster qubits formed by a small number (e.g. three) of P dopants located close to each other, the spin defining the logical state of the qubit is delocalized over the cluster. The effective exchange coupling between neighboring qubits obtained by integration of the exchange interaction over the clusters is finite with a high probability. Because the intracenter exchange interaction at small distances varies strongly with distance [118], for a random arrangement of three spins, the exchange couplings will differ with high probability and the system is not frustrated. Rather, in general a ground state doublet exists.

4.3 Larger spins

So far, our considerations have been restricted to clusters formed by spins $s = 1/2$. We next consider antiferromagnetic systems with larger spins $s > 1/2$.

4.3.1 Antiferromagnetic molecular clusters

Only very recently it has been shown theoretically that Grover's algorithm can be implemented with ferromagnetic molecular magnets using a unary encoding [38]. In view of universal quantum computing, ferromagnetic clusters such as the molecular magnets Mn_{12} and Fe_8 [119] suffer from the large net spin which usually means large matrix elements coupling the spin to the environment and, hence, short decoherence times.

In contrast, in antiferromagnetic systems such as the antiferromagnetic molecular rings discussed in Chapters 2 and 3, the spins couple such that they form a small total magnetic moment. Antiferromagnetic clusters which have unequal sublattice magnetization, will in general have a ground state multiplet rather than the singlet found for systems with compensated sublattice spins. Several antiferromagnetic molecular magnets comprised of spins with quantum numbers larger than $1/2$ have been synthesized to date [55, 56, 57, 58, 59] including several compounds with uncompensated sublattice spins [80]. As a paradigm, we consider systems with isotropic exchange coupling J , but allow for an easy or hard axis single-spin anisotropy,

$$\hat{H} = J\hat{\mathbf{s}}_1 \cdot \hat{\mathbf{s}}_2 + k_z(\hat{s}_{1,z}^2 + \hat{s}_{2,z}^2). \quad (4.37)$$

Here, s_1 and $s_2 = s_1 \pm 1/2$ are the spin quantum numbers of the two sublattices, respectively, $J > 0$ is an effective exchange constant, and k_z the single ion anisotropy. Equation (4.37) has a ground state doublet $\{|0\rangle, |1\rangle\}$ of $\hat{S}_z = \hat{s}_{1,z} + \hat{s}_{2,z}$ eigenstates with eigenvalues $\pm\hbar/2$, respectively. Because $[\hat{S}_z, \hat{H}] = 0$ for the Hamiltonian Eq. (4.37), the logical qubit basis states have an expansion of the

form (for $s_2 = s_1 - 1/2$)

$$\begin{aligned}
|0\rangle &= \sum_{m_1=-s_1+1}^{s_1} \alpha_{m_1} |m_1, 1/2 - m_1\rangle \\
&= \alpha_{-s_1+1} | -s_1 + 1, s_1 - 1/2\rangle \\
&\quad + \alpha_{-s_1+2} | -s_1 + 2, s_1 - 3/2\rangle + \dots \\
&\quad + \alpha_{s_1} |s_1, -s_1 + 1/2\rangle
\end{aligned} \tag{4.38}$$

in terms of the spin product basis. For $s_{1,2} \gg 1$, analytical expressions can be derived both for the action of a magnetic field (one-qubit rotation gate) and for the action of an interqubit coupling Hamiltonian (two-qubit gates) between clusters I and II,

$$\hat{H}_* = J_*(t) \hat{\mathbf{s}}_2^I \cdot \hat{\mathbf{s}}_1^II, \tag{4.39}$$

within a coherent state path integral formalism [47, 120]. We only state the main results of our calculations here. Further details are given in Appendix B.2.

4.3.2 Hard axis systems

For strong hard axis anisotropy, $k_z > 0$ and $k_z s_{1,2}^2/J \gg 1$, the spins \mathbf{s}_1 and \mathbf{s}_2 lie close to the (x, y) -plane for both states of the ground state doublet. A large contribution in the expansion Eq. (4.38) comes from the states $|m_1 = 0\rangle|m_2 = 1/2\rangle$ and $|m_1 = 0\rangle|m_2 = -1/2\rangle$, respectively. For illustration, for $s_1 = 3$, $s_2 = 5/2$, and $k_z/J = 0.2$, by numerical diagonalization of Eq. (4.37), we find

$$\begin{aligned}
|0\rangle &= 0.25 \left| 3, -\frac{5}{2} \right\rangle - 0.41 \left| 2, -\frac{3}{2} \right\rangle \\
&\quad + 0.52 \left| 1, -\frac{1}{2} \right\rangle - 0.52 \left| 0, \frac{1}{2} \right\rangle \\
&\quad + 0.42 \left| -1, \frac{3}{2} \right\rangle - 0.24 \left| -2, \frac{5}{2} \right\rangle.
\end{aligned} \tag{4.40}$$

The state $|1\rangle$ is obtained by $|m_1, m_2\rangle \rightarrow |-m_1, -m_2\rangle$ on the right hand side of Eq. (4.40). In agreement with the semiclassical theory, a major contribution to $\{|0\rangle, |1\rangle\}$ comes from states with small m_1 and m_2 .

In the following, we restrict our attention to systems with large anisotropy, $k_z(s_1^2 + s_2^2)/J \gg 1$. Then, $\Delta \simeq J$ (Appendix B.2) and

$$\begin{aligned}
|\langle 1 | \hat{S}_x | 0 \rangle| &= 1/4, \\
|\langle 1 | \hat{s}_{1,x} | 0 \rangle| &= s_1/2, \\
|\langle 1 | \hat{s}_{2,x} | 0 \rangle| &= s_2/2.
\end{aligned} \tag{4.41}$$

In particular, Eq. (4.39) translates into the effective Hamiltonian

$$\hat{H}_* = J_* |\langle 0 | \hat{s}_{1,z} | 0 \rangle| |\langle 0 | \hat{s}_{2,z} | 0 \rangle| \begin{pmatrix} 1 & 0 & 0 & 0 \\ 0 & -1 & 0 & 0 \\ 0 & 0 & -1 & 0 \\ 0 & 0 & 0 & 1 \end{pmatrix} + \frac{J_* s_1 s_2}{2} \begin{pmatrix} 0 & 0 & 0 & 0 \\ 0 & 0 & 1 & 0 \\ 0 & 1 & 0 & 0 \\ 0 & 0 & 0 & 0 \end{pmatrix} \quad (4.42)$$

in the two-qubit product basis. As discussed in Sec. 4.1.1, the CNOT gate can be realized with a unitary time evolution governed by this effective qubit coupling of the XXZ-form.

Matrix elements of order unity in Eq. (4.41) show that, for example, a magnetic field B_x efficiently rotates the state $|0\rangle$ into $|1\rangle$. This is not a priori evident given the rather complicated representation of the ground state doublet in the single-spin product basis [Eq. (4.38)]. The large matrix elements arise because, for both $|0\rangle$ and $|1\rangle$, the spins lie close to the (x, y) -plane in the hard axis system.

4.3.3 Easy axis systems

For $k_z < 0$, configurations with spins aligned along the z -axis are energetically favorable. We restrict our attention to systems with large anisotropy, $4|k_z|(s_1^2 + s_2^2)/J \gg 1$. Because a transition from $|0\rangle$ to $|1\rangle$ requires a rotation of both spins through a large energy barrier, from the theory of spin quantum tunneling in antiferromagnetic systems [49, 50] we find that $|\langle 1 | \hat{S}_x | 0 \rangle|$, $|\langle 1 | \hat{s}_{1,x} | 0 \rangle|$, $|\langle 1 | \hat{s}_{2,x} | 0 \rangle| \propto \exp(-\sqrt{8|k_z|(s_1^2 + s_2^2)/J}) \ll 1$ are exponentially small. Similarly to a spin chain in the Ising limit (Sec. 4.1.5), the easy axis system is a candidate for quantum computing schemes as suggested in Ref. [116].

The analytical results for the matrix elements discussed here are compared with numerical exact diagonalization for $s_1 = 7$ in Fig. 4.8. We find good agreement with our semiclassical results.

4.3.4 Experimental realization

Single molecule electrical switches [121, 122, 123, 124] have nourished hopes that, in the future, it will be possible to down-scale computers to the level at which bits or qubits are represented by single molecules. The results in Secs. 4.3.2 and 4.3.3 show that, in such bottom-up approaches aiming at a

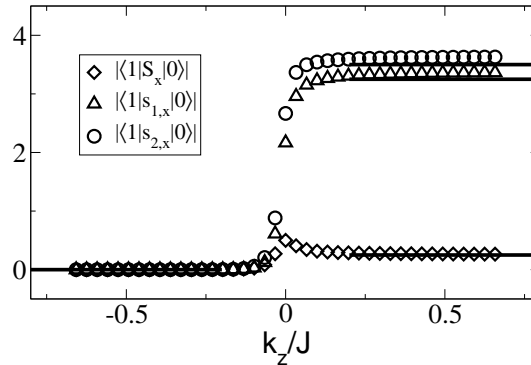


Figure 4.8: Matrix elements of spin operators of a qubit formed by two spins with spin quantum numbers $s_1 = 7$ and $s_2 = 6.5$. Numerical data (symbols) obtained from exact diagonalization are in good agreement with analytical results (solid lines).

universal quantum computer, control is not required at the level of single atom spins but only on the scale of molecule spins. In particular, molecular magnetic clusters with an effective spin $S = 1/2$ define a qubit. One-qubit quantum gates could be effected, for example, by a magnetic tip as used in magnetic force microscopy [125]. The spatial resolution of these techniques currently lies in the range of 10 – 100 nm [126] and approaches the typical size of molecular magnetic clusters [119].

Control of the exchange interaction between molecules is challenging. As has been demonstrated recently [122, 123], the electrical conductivity of individual molecules can be switched between two states in a controlled way. By connecting molecular magnetic clusters by reversible redox switches one could also switch intercluster exchange paths. Alternatively, if the relative position of molecular magnetic clusters can be controlled, the intercluster exchange interaction can be switched on and off via the overlap of electron orbital wave functions by moving clusters relative to each other.

4.4 Conclusion

In conclusion, we have shown that quantum computing is possible with a wide variety of clusters assembled from antiferromagnetically coupled spins which form an effective total spin $S = 1/2$. For arrays of spins $s = 1/2$, the existence of a spin cluster qubit requires little control over the placement and intracuster coupling of the spins and the spatial dimension of the array. This remains true for a wide range of systems with uncompensated sublattice spins differing by

1/2. We have shown explicitly that, for the spin cluster qubit, initialization, quantum gate operation, and readout are possible with the techniques proposed and analyzed for single spins. The scaling of the decoherence time with system size strongly depends on the microscopic decoherence mechanism. Spin cluster qubits are particularly promising in situations where decoherence is induced mainly by globally fluctuating fields during quantum gate operation and the decoherence rate of the spin cluster qubit is comparable to that of a single-spin qubit. The main advantage of spin clusters compared to single spins is that requirements on local control of magnetic fields and exchange interactions can be traded for longer gate operation times. We have illustrated the feasibility and advantages of spin cluster qubits for arrays of quantum dots, P dopants in a Si matrix, and molecular magnetic clusters.

In contrast to single spins, spin clusters are not intrinsically two-state systems and leakage during quantum gate operation must be accounted for. For the one-qubit rotation gate, we have shown that leakage is small if the magnetic field which induces the rotation is switched on and off adiabatically or if the Zeeman energy remains small compared to Δ .

Finally, we note that, because any qubit can be mapped onto a spin $s = 1/2$, the results presented here do not only apply to quantum computing proposals based on spin degrees of freedom but to any quantum computing scheme. More specifically, for any qubit for which methods for initialization, quantum gate operation, quantum error correction, and readout have been identified, a cluster qubit can be formed by coupling several qubits. For the cluster qubit, initialization, quantum gate operation, quantum error correction, and readout are possible using the same techniques as for the original qubit.

Chapter 5

Transport of magnetization

Transport of magnetization in various magnetic systems has received considerable attention both theoretically and experimentally [127, 128, 129, 130]. A spatially varying magnetic field gives rise to a current of magnetic dipoles [129, 130], similar to the transport of electric charge driven by an electric field. Here we consider insulating magnets described by a spin Hamiltonian, where magnetization is transported by excitations such as magnons and spinons without transport of charge. Theoretical work on such systems has so far been focused on the long-wavelength limit for magnets with translational invariance [129, 131, 132, 133].

In contrast, we propose to investigate magnetization transport in systems with broken translational invariance [134]. In particular, we consider a quasi one-dimensional system of finite length, e.g., a spin chain sandwiched between two bulk magnets which act as reservoirs for magnetization, where the magnetic field gradient is non-zero only over the system. Then, the magnetization current is determined by the spin *conductance* G which remains finite in the ballistic limit due to the contact resistance between the reservoirs and the system, in analogy to electronic transport in mesoscopic systems [41]. This is in stark contrast to the spin conductivity which diverges in the ballistic limit due to translational invariance [129, 131, 132, 133]. Here, we derive the spin conductance G for both ferromagnetic and antiferromagnetic systems.

This chapter is organized as follows. In Sec. 5.1, we show that, for ferromagnetic systems, magnetization transport can be viewed as transmission of magnons and the conductance is temperature dependent. For the antiferromagnetic spin-1/2 chain, the conductance has a value of order $(g\mu_B)^2/h$, where g is the gyromagnetic ratio and μ_B the Bohr-magneton (Sec. 5.2). In Sec. 5.3, we discuss experimental implications of our results. In particular, spin currents produce an electric field which allows one to measure G . We discuss magnetization transport in an external electric field and show that phenomena analogous to the Hall effect exist (Sec. 5.4).

5.1 Ferromagnetic systems

We first discuss a system with isotropic ferromagnetic exchange interaction in a magnetic field $\mathbf{B}(\mathbf{x}_i) = B_i \mathbf{e}_z$. The spins occupy the sites \mathbf{x}_i of a simple d -dimensional lattice with lattice constant a ,

$$\hat{H} = J \sum_{\langle ij \rangle} \hat{\mathbf{s}}_i \cdot \hat{\mathbf{s}}_j + g\mu_B \sum_i B_i \hat{s}_{i,z}, \quad (5.1)$$

with $J < 0$. Here, $\hat{\mathbf{s}}_i$ is the spin operator of the spin with spin quantum number s at \mathbf{x}_i , and $\langle ij \rangle$ denotes nearest neighbor sites. For low temperatures, Eq. (5.1) can be diagonalized by introducing magnon operators which describe small fluctuations of the spins around \mathbf{e}_z [47]. Following the standard procedure, we introduce magnon creation and annihilation operators defined in terms of the spin ladder operators $\hat{s}_i^\pm = \hat{s}_{i,x} \pm i\hat{s}_{i,y}$ by

$$\begin{aligned} \hat{s}_i^+ &= \hat{b}_i^\dagger \left(\sqrt{2s - \hat{b}_i^\dagger \hat{b}_i} \right), \\ \hat{s}_i^- &= \left(\sqrt{2s - \hat{b}_i^\dagger \hat{b}_i} \right) \hat{b}_i, \\ \hat{s}_{i,z} &= -s + \hat{b}_i^\dagger \hat{b}_i. \end{aligned} \quad (5.2)$$

For spatially constant $B_i = B > 0$, the elementary excitations of the extended system are plane spin waves,

$$\hat{H} \simeq -\frac{Ns^2|J|}{2} + \sum_{\mathbf{k}} \epsilon_{\mathbf{k}} \hat{b}_{\mathbf{k}}^\dagger \hat{b}_{\mathbf{k}}, \quad (5.3)$$

where N is the total number of sites in the lattice and

$$\hat{b}_{\mathbf{k}} = \frac{1}{\sqrt{N}} \sum_i e^{-i\mathbf{k} \cdot \mathbf{x}_i} \hat{b}_i \quad (5.4)$$

is the destruction operator of a magnon with wave vector \mathbf{k} . The magnon dispersion relation is [2]

$$\epsilon_{\mathbf{k}} \simeq g\mu_B B + |J|sa^2k^2. \quad (5.5)$$

Most importantly for the subsequent discussion of magnetization currents, a magnon carries a magnetic moment $-g\mu_B \mathbf{e}_z$. For temperatures $T \ll g\mu_B B/k_B$, the magnon density is small and noninteracting-magnon theory is valid for all d .

We now consider a set-up for a magnetization transport measurement as sketched in Fig. 5.1(a). A spin chain extends from $x = -L/2$ to $L/2$ and is

suspended between two large three-dimensional reservoirs, R1 and R2. $L \gg a$ is sufficiently small that magnons propagate ballistically through the chain. The reservoirs narrow adiabatically toward the chain [“transition region” in Fig. 5.1(a)]. The system is still described by Eq. (5.1), with the sites \mathbf{x}_i occupying a bounded region in space [Fig. 5.1(a)]. A small spatially varying magnetic field $\delta B(x)\mathbf{e}_z$ with $\delta B(x) = -\Delta B/2$ ($\Delta B/2$) for $x < -L/2$ ($x > L/2$) is superimposed on the offset field $B\mathbf{e}_z$ for $t > 0$ [Fig. 5.1(b)]. For $|x| < L/2$, $\delta B(x)$ interpolates smoothly between the values $\pm\Delta B/2$ in the reservoirs. The field gradient results in a magnetization current I_m from R1 to R2. In linear response theory, I_m can be expressed in terms of the spin conductivity $\sigma(x, x', \omega)$,

$$I_m(x, \omega) = \int dx' \sigma(x, x', \omega) \partial_{x'} \delta B(x', \omega). \quad (5.6)$$

To calculate $I_m(x, \omega)$, knowledge of σ for $x, x' \in [-L/2, L/2]$ is sufficient because $\partial_{x'} \delta B(x', \omega) = 0$ inside the reservoirs. For a quasi one-dimensional system, due to the continuity equation, σ is related to the susceptibility χ by $\sigma(q, \omega) = -i\omega\chi(q, \omega)/q^2$. We only discuss transport of the z -component of magnetization driven by a magnetic field along \mathbf{e}_z . The corresponding indices are omitted for brevity, i.e., $\chi_{zz} \rightarrow \chi$. In the noninteracting-magnon approximation,

$$\chi(q, \omega) = -\frac{(g\mu_B)^2}{\hbar} \int_{-\infty}^{\infty} \frac{dk}{2\pi} \frac{n_B(\epsilon_{k+q}) - n_B(\epsilon_k)}{(\epsilon_{k+q} - \epsilon_k)/\hbar + \omega + i0}. \quad (5.7)$$

Here, $n_B(\epsilon) = 1/(\exp(\beta\epsilon) - 1)$ is the Bose distribution function and $\beta = 1/k_B T$. In the limit $\omega \rightarrow 0$ of a static field, from Eq. (5.7) we find that $\lim_{\omega \rightarrow 0} \sigma(x, x', \omega) = (g\mu_B)^2 n_B(g\mu_B B)/h$ is independent of x and x' . Integrating over x' in Eq. (5.6), we find that the magnetization current in the system

$$I_m(x) = \frac{(g\mu_B)^2}{h} n_B(g\mu_B B) \cdot \Delta B = G \cdot \Delta B \quad (5.8)$$

is constant and only depends on the difference of magnetic fields in the reservoirs, ΔB . Although magnetization is transported ballistically, the spin *conductance* G remains finite because of the contact resistance for magnons between reservoirs and system, similar to the related phenomenon in charge transport [41]. On a technical level, because of the interface between the reservoirs and the system, translational invariance is broken such that the x' -integration in Eq. (5.6) extends only over the system and I_m remains finite.

In ferromagnetic systems, the magnetization current is carried by magnons. This allows us to reproduce Eq. (5.8) from the Landauer-Büttiker approach [41]. The field difference ΔB switched on at $t = 0$ results in a shift of the magnon energies ϵ in the reservoirs [Eq. (5.5)] and of the magnon distribution functions $n_B(\epsilon)$ [Fig. 5.1(c)]. Note that the magnon distribution functions are only shifted

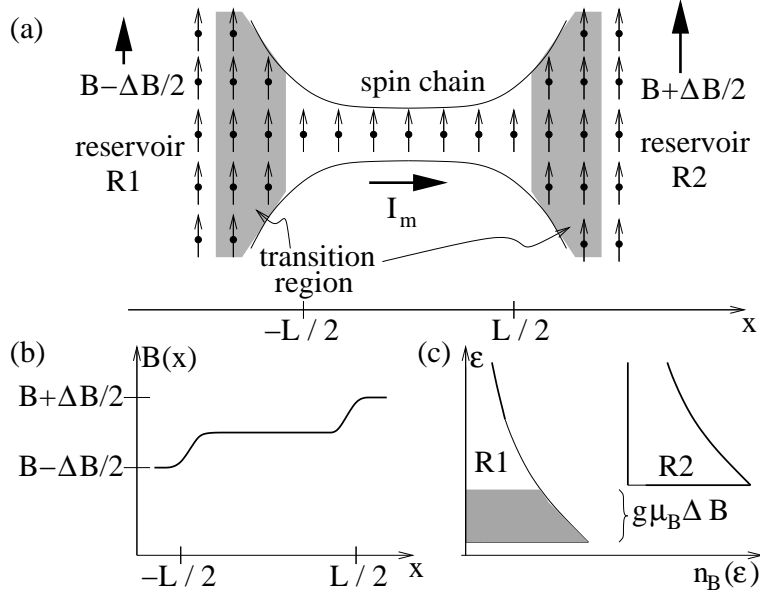


Figure 5.1: (a) Proposed experimental set-up for the measurement of a magnetization current I_m . (b) A magnetic field difference ΔB between the two bulk systems gives rise to $I_m = G \cdot \Delta B$. (c) ΔB shifts the Bose functions $n_B(\epsilon)$ in the reservoirs R1, R2. Magnons with energies ϵ within the shaded region in R1 are not transmitted to R2.

but do not relax to the equilibrium distributions corresponding to the new field. Hence, a nonequilibrium situation is established. The magnetization in the reservoirs relaxes toward the new equilibrium values by magnetization transport from R1 to R2, i.e., the magnetization current I_m . All magnons incident on the spin chain from R2 are transmitted into R1. For the clean system considered here, the magnon transmission coefficient is unity. In contrast, magnons with $\epsilon \in [g\mu_B(B - \Delta B/2), g\mu_B(B + \Delta B/2)]$ are not transmitted from R1 to R2. This results in a net magnetization transport current

$$\begin{aligned}
 I_m &= g\mu_B \int_0^{g\mu_B \Delta B} d\epsilon v(\epsilon) \rho(\epsilon) n_B(\epsilon + g\mu_B B) \\
 &\simeq \frac{(g\mu_B)^2}{h} n_B(g\mu_B B) \cdot \Delta B = G \cdot \Delta B,
 \end{aligned} \tag{5.9}$$

where $v(\epsilon) = \partial_{k_x} \epsilon_{k_x} / \hbar$ is the magnon velocity and $\rho(\epsilon) = 1/hv(\epsilon)$ is the magnon density of states in the spin chain. This result obtained from the Landauer-Büttiker approach for magnons agrees with the calculation using response functions, Eq. (5.8). Equation (5.8) remains valid for $g\mu_B \Delta B \ll k_B T \ll g\mu_B B$. The requirement that $g\mu_B \Delta B$ be the smallest energy scale guarantees the validity of linear response theory while $k_B T \ll g\mu_B B$ ensures that the magnon

density remains much smaller than $1/a$ and noninteracting magnon theory is applicable.

If the system connecting R1 and R2 consists of several chains with finite interchain exchange J' , magnetization can be transported by each of the transverse modes which act as independent transport channels. For the conductance, we find $G = (g\mu_B)^2 \sum_{k_\perp} n_B(g\mu_B B + \epsilon_{k_\perp})/h$, where ϵ_{k_\perp} is the energy of the transverse magnon mode. For a wire with square cross section, width W , and interchain spacing a , $\epsilon_{k_\perp} \simeq J'S(\pi a/W)^2(n_y^2 + n_z^2)$, where $n_y, n_z = 1, \dots, \lfloor W/a \rfloor$ label the transverse modes.

To contrast these results with charge transport between two Fermi-liquid reservoirs, we note the following. The offset field B leads to an energy gap $g\mu_B B$ in the magnon spectrum. Thus, magnetization transport requires thermal excitation of magnons across the gap and G is strongly temperature dependent. In the range of validity of noninteracting magnon theory, $T \ll g\mu_B B/k_B$, $G \ll (g\mu_B)^2/h$. At $T = 0$, $G = 0$ because the system and the reservoirs are in the spin-polarized ground state. This is in contrast to the charge conductance which remains usually finite at $T = 0$ [41]. Note that, although the spin conductance G of the ferromagnet depends on the offset magnetic field B and the temperature, it is universal in the sense that it is independent of the exchange interaction J , the spin quantum number s , and the lattice spacing a .

The Hamiltonian Eq. (5.1) describes a perfect system for which the transmission probability for magnons is unity. We next show that the magnetization current is strongly reduced by impurities in the system. For definiteness, we consider the perturbation $\hat{H}' = g\mu_B B_{\text{imp}} \hat{s}_{0,z}$ which describes a static magnetic impurity field B_{imp} that acts only on a single spin, \hat{s}_0 [Fig. 5.2(a)]. Such a perturbation is effected, for example, by a static spin which is coupled to \hat{s}_0 by an exchange coupling. The single magnon Hamiltonian then reads

$$\hat{h} = -|J|sa^2\partial_x^2 + g\mu_B B + aV_0\delta(x), \quad (5.10)$$

where $V_0 = g\mu_B B_{\text{imp}}$ is the scattering potential for magnons created by the impurity magnetic field [Fig. 5.2(b)]. For a magnon incident on the potential $aV_0\delta(x)$ with an energy $g\mu_B B + \epsilon$, the transmission amplitude calculated from Eq. (5.10) is $t(\epsilon) = 1/(1 - iV_0/\sqrt{4|J|S\epsilon})$ [135] and the transmission probability becomes

$$T(\epsilon) = \frac{1}{1 + (V_0^2/4|J|S\epsilon)}. \quad (5.11)$$

The magnetization current then follows from

$$I_m = \frac{g\mu_B}{h} \int_0^{g\mu_B \Delta B} d\epsilon n_B(\epsilon + g\mu_B B) T(\epsilon). \quad (5.12)$$

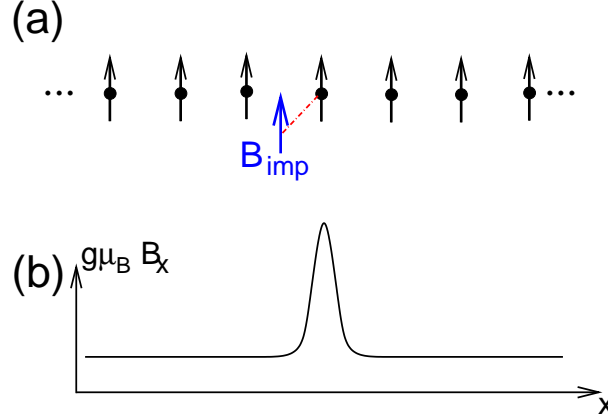


Figure 5.2: (a) Model system in which the transmission probability for magnons is smaller than unity. A static impurity spin is coupled to one spin of the system, \hat{s}_0 , and creates a local Zeeman field $g\mu_B B_{\text{imp}}$. (b) In the continuum limit, the local magnetic field translates into a potential barrier $g\mu_B B_{\text{imp}} a\delta(x)$ for magnons.

In particular, if ΔB remains the smallest energy scale of the problem, $\Delta B \ll (g\mu_B B_{\text{imp}})^2/4|J|s$, with $T(\epsilon) \propto \epsilon$ for all current carrying modes we find that

$$I_m = \frac{(g\mu_B)^2}{h} n_B (g\mu_B B) \frac{2|J|s g\mu_B}{(g\mu_B B_{\text{imp}})^2} (\Delta B)^2 \quad (5.13)$$

increases with $(\Delta B)^2$, i.e., the linear spin conductance vanishes for $\Delta B \rightarrow 0$. This strong dependence of the magnetization current I_m on the scattering potential can be traced back to the fact that the magnetization current is carried by magnons with low energies, $\epsilon \leq g\mu_B \Delta B$ [Fig. 5.1(c)], for which the transmission probability is strongly energy dependent. This is in stark contrast to the charge conductance for electrons which is reduced by the transmission probability for an electron incident at the Fermi energy ϵ_F . The transmission probability only depends on ϵ_F and the barrier height V_0 of the scattering potential but not on the applied potential bias, and the charge conductance remains finite.

5.2 Antiferromagnetic systems

As we show next, magnetization transport in antiferromagnets is significantly different from ferromagnets but similar to charge transport in Fermi liquids. In an antiferromagnetic chain with half-integer spin the elementary excitations are massless and we will show that $G \neq 0$ even at $T = 0$. The spin-1/2 chain is believed to capture the essential features [136, 137, 138, 139]. Thus, we now

consider a spin-1/2 chain with isotropic antiferromagnetic exchange interaction $J > 0$ in Eq. (5.1) suspended between two antiferromagnetic reservoirs. The analysis including the result in Eq. (5.19) remains valid also for anisotropic spin-1/2 chains which show Luttinger liquid behavior. For $t > 0$, a magnetic field $B(x)$ is applied along \mathbf{e}_z such that $B(x) = -\Delta B/2$ ($\Delta B/2$) for $x < -L/2$ ($x > L/2$). By a Jordan-Wigner transformation and subsequent bosonization, the spin chain can be mapped onto a Luttinger liquid (spinless fermions). Then, at $T = 0$, the Euclidean Lagrangean flows into a massless free theory under renormalization group [136, 137, 139],

$$L = \int dx \frac{K}{2} \left[\frac{1}{v} (\partial_\tau \phi)^2 + v (\partial_x \phi)^2 \right], \quad (5.14)$$

where $K = 2$, $v = (\pi/2)Ja/\hbar$, and the homogeneous part of \hat{s}_z is identified with $\partial_x \phi / \sqrt{\pi}$. The imaginary-time spin conductivity is [140]

$$\sigma(q, \omega_n) = (g\mu_B)^2 \frac{v}{\pi\hbar K} \frac{\omega_n}{\omega_n^2 + v^2 q^2}. \quad (5.15)$$

However, in order to calculate G for the inhomogeneous system, it is not sufficient to evaluate the limit $\omega \rightarrow 0$ of $\sigma(q, \omega)$ because the elementary excitations change on propagation from the reservoirs (magnons) through the chain (spinons). Following the related analysis for charge transport through a Luttinger liquid coupled to Fermi leads [141], we model the transition from a three-dimensional ordered antiferromagnetic state to the spin chain by spatially varying $K(x)$ and $v(x)$ in the Lagrangean Eq. (5.14). For simplicity, we assume that $K(x)$ and $v(x)$ change discontinuously from the values of the spin chain to the ones of a bulk antiferromagnet at $x = \pm L/2$ [Fig. 5.3(a)]. The values K_b and v_b in the bulk region are chosen such that Eq. (5.14) correctly reproduces the dynamic susceptibility of a three-dimensional antiferromagnetically ordered state. From the nonlinear sigma model description [84], we estimate $v_b \simeq \sqrt{3}Ja/\hbar$ and $K_b \simeq 4\sqrt{3}/\pi$. The spin conductance then follows from

$$G = \frac{(g\mu_B)^2}{\pi\hbar} \lim_{\omega_n \rightarrow 0} \omega_n G_{\phi\phi}(x, x', \omega_n) \quad (5.16)$$

where the time ordered Green's function

$$G_{\phi\phi}(x, x', \omega_n) = \int_0^\infty d\tau e^{-i\omega_n\tau} \langle T_\tau \phi(x, \tau) \phi(x', 0) \rangle, \quad (5.17)$$

must be evaluated for the *inhomogeneous* system including the transition regions [141]. For given $x' \in [-L/2, L/2]$, $G_{\phi\phi}(x, x', \omega_n)$ is obtained from the ansatz

$$G_{\phi\phi}(x, x', \omega_n) = a \exp\left(\frac{\omega_n x}{v(x)}\right) + b \exp\left(-\frac{\omega_n x}{v(x)}\right) \quad (5.18)$$

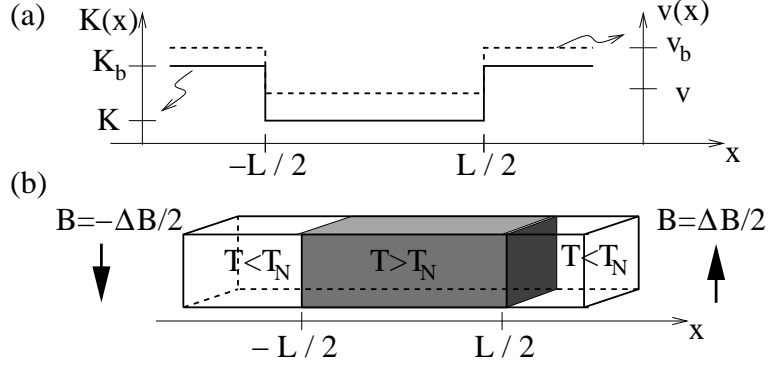


Figure 5.3: (a) The transition from the three-dimensional antiferromagnetically ordered bulk to the spin-1/2 chain is modelled by spatially varying $K(x)$ (solid line) and $v(x)$ (dashed line) in Eq. (5.14). (b) Set-up for a transport measurement in an antiferromagnetic system.

for the four regions $x < -L/2$, $-L/2 < x < x'$, $x' < x < L/2$, and $L/2 < x$. The coefficients a and b are determined by the boundary conditions that $G_{\phi\phi}(x, x', \omega_n)$ and $K(x)v(x)\partial_x G_{\phi\phi}(x, x', \omega_n)$ are continuous at $x = \pm L/2$, $G_{\phi\phi}(x, x', \omega_n)$ is continuous at $x = x'$, and $K(x)v(x)\partial_x G_{\phi\phi}(x, x', \omega_n)|_{x=x'+0} - K(x)v(x)\partial_x G_{\phi\phi}(x, x', \omega_n)|_{x=x'-0} = 1$ by definition of the Green's function. The boundary conditions for the spin current are automatically satisfied by evaluating Eq. (5.17). In particular, the requirement that $K(x)v(x)\partial_x G_{\phi\phi}(x, x', \omega_n)$ is continuous at $x = \pm L/2$ assures magnetization current conservation at the transition from the antiferromagnetic reservoir to the spin chain. We find that $\lim_{\omega_n \rightarrow 0} \omega_n G_{\phi\phi}(x, x', \omega_n) = 1/2 K_b$ is independent of x , x' and of the parameters K and v of the spin chain. The spin conductance at $T = 0$,

$$G = \frac{(g\mu_B)^2}{hK_b}, \quad (5.19)$$

depends only on the parameter K_b of the bulk system. Note that the conductance G is universal in the sense that it does not depend on the parameters of the spin chain. Rather, also spin chains with anisotropic exchange couplings that flow into a massless free theory, Eq. (5.14), would exhibit the spin conductance G in Eq. (5.19).

We next argue that Eq. (5.19) remains valid also for a finite temperature and an offset magnetic field. Both analytical [142] and recent numerical [131] analysis indicate that, even at finite $T \ll J/k_B$, Eq. (5.14) describes the low energy behavior of the spin-1/2 chain correctly. Similarly, a finite offset magnetic field, $g\mu_B B \ll J$, suppresses quantum fluctuations of \hat{s}_z in the bulk, leading only to a slight decrease of K_b . Our result Eq. (5.19) is hence robust both for finite temperatures and magnetic fields. In summary, an antiferromagnetic spin-1/2

chain suspended between antiferromagnetic reservoirs acts as transport channel for magnetization with a spin conductance of order $(g\mu_B)^2/h$. For N parallel spin chains with vanishing interchain exchange interaction, each chain acts as independent transmission channel and G increases by a factor N . The spin conductance is quantized in units of order $(g\mu_B)^2/h$.

Preparation of a sample as shown in Fig. 5.1(a) is challenging. A promising strategy is the use of a bulk material with an intrachain exchange coupling J much stronger than the interchain exchange interaction, such as Sr_2CuO_3 . If heated to temperatures T much larger than the Néel ordering temperature T_N , the spin chains decouple and magnetization is transported predominantly along the spin chains. Hence, an antiferromagnetic wire heated to $T > T_N$ in its central part, but cooled to $T \ll T_N$ at its ends [Fig. 5.3(b)] provides a realization of the system in Fig. 5.1(a). If both reservoirs are cooled to the same temperature, temperature gradients will not give rise to a net magnetization current between the reservoirs because of symmetry. Recent experiments [143, 144] provide strong evidence that elementary excitations in various quasi one-dimensional systems have mean free paths of several hundred nanometers at temperatures up to 50 K and the mean free path is limited by the defect concentration in the samples. For $L < 1 \mu\text{m}$, transport through the system shown in Fig. 5.3(b) then is indeed ballistic as assumed above.

5.3 Detection of spin currents

We next discuss how G can be measured experimentally. A current of magnetic dipoles produces an electric dipole field [145]. The electric field is most easily calculated by decomposing the magnetization current into contributions propagating at a certain velocity v , $I_m = g\mu_B \sum_v n(v)v$, where $n(v)$ is the line density of magnetic dipoles with velocity v . For each v , the electric field in the laboratory frame is obtained by a Lorentz transform of the magnetic dipole field in the co-moving frame. Summing over v , we find that the total electric dipole field [Fig. 5.4(a)]

$$\mathbf{E}_m(\mathbf{x}) = \frac{\mu_0}{2\pi} \frac{I_m}{r^2} (0, \cos 2\phi, -\sin 2\phi) \quad (5.20)$$

depends only on I_m . Here, $\sin \phi = y/r$, $\cos \phi = z/r$, and $r = \sqrt{y^2 + z^2}$ is the radial distance from the magnetization current. Note that the electric field decreases with $1/r^2$ rather than $1/r$ because the magnetization current is carried by magnetic dipoles. In contrast, the magnetic field produced by a charge current I is proportional to I/r because charge monopoles are transported.

For a numerical estimate, we now consider N parallel uncoupled antiferromagnetic spin-1/2 chains connecting two antiferromagnetic reservoirs. With

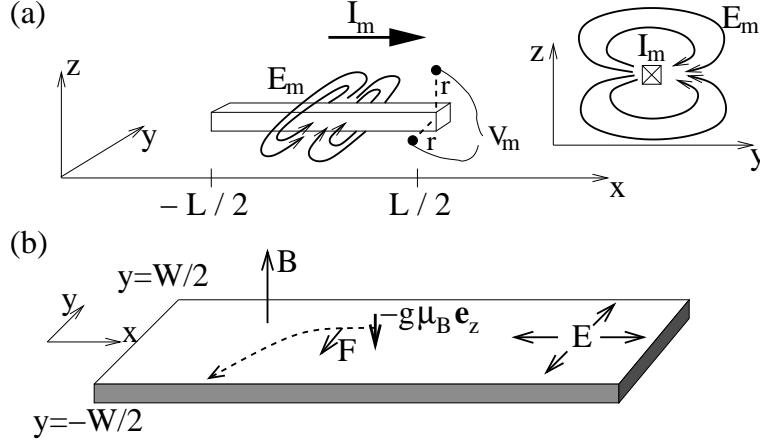


Figure 5.4: (a) A current of magnetic dipole moment I_m produces an electric dipole field leading to a measurable voltage V_m . (b) Magnetic dipoles $-g\mu_B \mathbf{e}_z$ driven by a magnetic field gradient ∇B in an inhomogeneous electric field $\mathbf{E}(\mathbf{x})$ experience a force \mathbf{F} analogous to the Lorentz force.

Eqs. (5.19) and (5.20),

$$|\mathbf{E}_m(\mathbf{x})| \sim N \frac{\mu_0}{2\pi} \frac{(g\mu_B)^2}{h} \frac{\Delta B}{r^2} = N \frac{g^2}{4} \cdot 10^{-19} \frac{\Delta B [T] V}{r[m]^2 m}. \quad (5.21)$$

Even for moderate $\Delta B = 10^{-3}$ T and large $r = 10^{-5}$ m, the magnetization current transported by $N \simeq 10^4$ parallel spin chains leads to an electric field $E_m \sim 10^{-8}$ V/m. The voltage drop between the two points $(0, r, 0)$ and $(0, 0, r)$ indicated in Fig. 5.4(a) is then $V_m = E_m r \simeq 10^{-13}$ V which is within experimental reach. Picovolt sensitivity is reported, for example, in Ref. [146]. For N uncoupled ferromagnetic chains, I_m and thus E_m and V_m are smaller by a factor $n_B(g\mu_B B) \simeq \exp(-\beta g\mu_B B)$. For the temperature range considered in Sec. 5.1, $T \ll g\mu_B B/k_B$, the Bose factor is small compared to unity and the detection of E_m would require a sample with a larger number of chains connecting the reservoirs, $N \gtrsim 10^4 \exp(\beta g\mu_B B)$, for $\Delta B = 10^{-3}$ T and $r = 10^{-5}$ m.

Interactions not included in the Hamiltonian Eq. (5.1) could lead to a relaxation of the magnetization in the reservoirs within the spin-lattice relaxation time τ_s . The expressions for the magnetization current in ferromagnetic and antiferromagnetic systems, Eqs. (5.8) and (5.19), respectively, then remain valid only for $t \lesssim \tau_s$. For a static ΔB , I_m vanishes for $t > \tau_s$. This problem can be avoided by an alternating current measurement where ΔB oscillates with a frequency ω , with $J/\hbar \gg \omega \gtrsim 1/\tau_s$. τ_s can be estimated from the linewidth in ferromagnetic resonance. For example, for YIG, $\tau_s > 10^{-7}$ s [147]. Alternatively, the magnetization could be maintained with a “spin battery” of the type proposed in Ref. [148].

5.4 Spin currents in electric fields

A moving magnetic dipole moment also interacts with an external electric field $\mathbf{E}(\mathbf{x})$, leading to phenomena analogous to the Hall effect. A magnetic dipole $-g\mu_B\mathbf{e}_z$ moving in an electric field acquires an Aharonov-Casher phase [149] and the spin Hamiltonian is modified to

$$\hat{H} = \frac{J}{2} \sum_{\langle ij \rangle} [\hat{s}_i^+ \hat{s}_j^- e^{-i\theta_{ij}} + \hat{s}_i^- \hat{s}_j^+ e^{i\theta_{ij}} + 2\hat{s}_{i,z} \hat{s}_{j,z}] + g\mu_B \sum_i B_i \hat{s}_{i,z}, \quad (5.22)$$

where $\hat{s}_j^\pm = \hat{s}_{j,x} \pm i\hat{s}_{j,y}$ and $\theta_{ij} = g\mu_B \int_{\mathbf{x}_i}^{\mathbf{x}_j} d\mathbf{x} \cdot (\mathbf{E} \times \mathbf{e}_z) / \hbar c^2$. Introducing magnon creation and annihilation operators, Eq. (5.22) can be rewritten in terms of magnons with single-magnon Hamiltonian \hat{h} . From Eq. (5.22), we find

$$\hat{h} = \frac{|J|sa^2}{\hbar^2} (\hat{\mathbf{p}} - g\mu_B \mathbf{E} \times \mathbf{e}_z / c^2)^2 + g\mu_B B. \quad (5.23)$$

Here, we discuss only the classical motion of magnons propagating with velocity $\mathbf{v} = -v_x \mathbf{e}_x$ in a two-dimensional system of finite width W in the y -direction [Fig. 5.4(b)], where $I_m = g\mu_B n v_x W$, and n is the magnon density. From the equation of motion implied by Eq. (5.23), one obtains the force acting on a magnon, $\mathbf{F} = -g\mu_B \nabla [B - (\mathbf{v} \times \mathbf{E}) \cdot \mathbf{e}_z / c^2]$. The second term accounts for the interaction with the electric field. We now focus on $\mathbf{E} = E'(x, y, -2z)$ with $E' = \text{const}$. Then, the equation of motion of the magnons is formally identical to that of electrons in a constant magnetic field. Magnons are deflected into the \mathbf{e}_y direction perpendicular to the transport direction \mathbf{e}_x . Stationarity is reached when the magnon repulsion equals the driving force along \mathbf{e}_y due to the electric field. Taking into account only dipolar forces between the magnons, in the stationary state $B - v_x E' y / c^2$ is constant as function of y . The difference in magnetic fields $\Delta B = B(y = W/2) - B(y = -W/2)$ is related to the magnetization current density by the spin Hall conductance G_H ,

$$\frac{I_m}{W} = -G_H \frac{\Delta B}{W} = -\frac{g\mu_B n c^2}{E'} \frac{\Delta B}{W}, \quad (5.24)$$

in close formal analogy to the Hall conductance for charge transport in a transverse magnetic field.

We next provide an estimate for the magnitude of the spin Hall effect. In the hydrodynamic regime, the drift velocity v_x is determined by the magnon scattering time τ . At low temperatures, τ is limited by impurities in the sample. For τ on the order of $10^2 \dots 10^3$ ns, as measured for YIG at 1-4 K [150],

$\partial_x B = 10^5$ T/m, $J = 200 Kk_B$, $s = 1$, and $a = 1 \text{ \AA}$, the drift velocity is $v_x = 10^3 \dots 10^4$ m/s. A variation of electric field $\Delta E = E(y = W/2) - E(y = -W/2) = 10^7$ V/m across the magnetic system then would lead to $\Delta B = 10^{-3} \dots 10^{-2}$ G resulting from the spin Hall effect. Thus, the spin Hall conductance G_H is within experimental reach.

5.5 Conclusion

In conclusion, we have shown that magnetization transport in quasi one-dimensional insulating ferromagnetic and antiferromagnetic systems is described by a spin conductance which is independent of the system parameters. Magnetization currents produce an electric field which allows one to measure the conductance directly. For magnetization transport in an external electric field, phenomena analogous to the Lorentz force and the Hall effect in charge transport emerge. Our results for magnetization transport in insulating magnets are summarized in Table 5.1.

	magnetization transport	charge transport
conductance G	$\frac{(g\mu_B)^2}{h} \mathcal{O}(1)$ (AFM, spin-1/2)	$\frac{2e^2}{h}$
detection	$ \mathbf{E}_m(\mathbf{x}) = \frac{\mu_0}{2\pi} \frac{I_m}{ \mathbf{x} ^2}$	$ \mathbf{B}(\mathbf{x}) = \frac{\mu_0}{2\pi} \frac{I}{ \mathbf{x} }$
Hall conductance G_H	$\frac{g\mu_B n c^2}{E'}$	$\frac{en}{B}$

Table 5.1: Results obtained for the transport of magnetization in comparison with the corresponding results for charge transport. We report the conductance G for one transport channel, the electric field (magnetic field) produced by a magnetization (charge) current, and the Hall conductance for a magnetization current in an external electric field and for electrons in a transverse magnetic field, respectively. See text for further details.

Appendix A

Spin correlation functions of antiferromagnetic molecular rings

A.1 Undoped antiferromagnetic molecular rings

The correlation functions for the antiferromagnetic molecular ring in Eq. (2.28) are derived in the following way. With $M_y = M_z = 0$ [84],

$$\begin{aligned} \chi_{\alpha\alpha}(\tau) = & (g\mu_B)^2 \frac{N\hbar}{4J} \delta(\tau) (1 - \langle n_\alpha^2 \rangle) \\ & + (g\mu_B)^2 \left(\frac{N\hbar}{4J} \right)^2 \frac{1}{Z} \int \mathcal{D}\mathbf{n} [i(\mathbf{n} \times \dot{\mathbf{n}})_\alpha + n_\alpha h_x n_x]_\tau \\ & [i(\mathbf{n} \times \dot{\mathbf{n}})_\alpha + n_\alpha h_x n_x]_0 e^{-\int_0^{\beta\hbar} d\tau L_0[\mathbf{n}]/\hbar}, \end{aligned} \quad (\text{A.1})$$

where the first (second) square bracket is evaluated at τ (0). Using the parameterization in Eq. (2.17) and expanding to second order in $\vartheta = \theta - \pi/2$, for $\alpha = y$ the square bracket reads

$$i(\mathbf{n} \times \dot{\mathbf{n}})_y + n_y h_x n_x = -(h_x - i\dot{\phi})\vartheta \cos \phi - i\dot{\vartheta} \sin \phi. \quad (\text{A.2})$$

The corresponding expression for $\alpha = z$ can be obtained by setting $\phi \rightarrow \phi - \pi/2$. Integrating out ϑ , we obtain

$$\begin{aligned}
\chi_{yy}(\tau) &= (g\mu_B)^2 \frac{N\hbar}{4J} (1 - \langle \cos^2 \phi \rangle) \delta(\tau) \\
&+ \left(\frac{N\hbar}{4J} \right)^2 \frac{1}{Z} \int \mathcal{D}\phi e^{-\int_0^{\beta\hbar} d\tau L_0[\phi]/\hbar} \\
&\times [G_{\vartheta\vartheta}(\tau)(h_x - i\dot{\phi}(\tau)) \cos \phi(\tau) (h_x - i\dot{\phi}) \cos \phi \\
&+ iG_{\vartheta\dot{\vartheta}}(\tau)(h_x - i\dot{\phi}(\tau)) \cos \phi(\tau) \sin \phi \\
&+ iG_{\dot{\vartheta}\vartheta}(\tau) \sin \phi(\tau)(h_x - i\dot{\phi}) \cos \phi \\
&+ i^2 G_{\dot{\vartheta}\dot{\vartheta}}(\tau) \sin \phi(\tau) \sin \phi]. \tag{A.3}
\end{aligned}$$

The Green's functions are defined by $G_{\vartheta\vartheta}(\tau) = \langle T_\tau \vartheta(\tau) \vartheta \rangle - \langle \vartheta \rangle^2$. In the high-field limit $h_x \gg \omega_0$, all Green's functions are strongly peaked at $\tau = 0$. Using the adiabatic approximation outlined after Eq. (2.18), we find from $L_0[\mathbf{n}]$ [Eq. (2.18)] (up to $\mathcal{O}(\omega_0^2/h_x^2)$)

$$G_{\vartheta\vartheta}(\tau) \simeq \frac{2J}{N\hbar(h_x - i\dot{\phi})} e^{-(h_x - i\dot{\phi})|\tau|}, \tag{A.4}$$

$$G_{\vartheta\dot{\vartheta}}(\tau) \simeq \frac{2J}{N\hbar} \text{sgn}(\tau) e^{-(h_x - i\dot{\phi})|\tau|}, \tag{A.5}$$

$$G_{\dot{\vartheta}\vartheta}(\tau) \simeq \frac{4J}{N\hbar} \delta(\tau) - \frac{2J(h_x - i\dot{\phi})}{N\hbar} e^{-(h_x - i\dot{\phi})|\tau|}, \tag{A.6}$$

where $\dot{\phi} = \dot{\phi}(0)$. Along the classical path, the field ϕ varies on a timescale $1/\omega_0$, i.e. slowly on the timescale over which the Green's functions vanish, which allows us to set $\exp[-(h_x - i\dot{\phi})|\tau|] \rightarrow (2/(h_x - i\dot{\phi}))\delta(\tau)$ in $G_{\vartheta\vartheta}$ and $G_{\dot{\vartheta}\vartheta}$. Because $G_{\vartheta\dot{\vartheta}} = -G_{\dot{\vartheta}\vartheta}$ the second and third term in Eq. (A.3) cancel. To leading order in ω_0/h_x we then obtain

$$\begin{aligned}
\chi_{yy}(\tau) &\simeq (g\mu_B)^2 \frac{N\hbar}{4J} \left[(1 - \langle \cos^2 \phi + \sin^2 \phi \rangle) \delta(\tau) + \frac{h_x}{2} e^{-h_x|\tau|} \right] \\
&= (g\mu_B)^2 \frac{N\hbar h_x}{8J} e^{-h_x|\tau|} \simeq (g\mu_B)^2 \frac{N\hbar}{4J} \delta(\tau), \tag{A.7}
\end{aligned}$$

and

$$\chi_{zz}(\tau) \simeq (g\mu_B)^2 \frac{N\hbar h_x}{8J} e^{-h_x|\tau|} \simeq (g\mu_B)^2 \frac{N\hbar}{4J} \delta(\tau). \tag{A.8}$$

By Fourier transform one obtains Eq. (2.28), i.e., $\chi_{yy}(i\omega_n)$ and $\chi_{zz}(i\omega_n)$ have no resonance at the tunnel splitting Δ .

A.2 Doped antiferromagnetic molecular rings

The matrix element $|\langle e|\hat{S}_z|g\rangle|$ for the modified AFMR is most easily obtained in the following way. As shown in Sec. 2.2.1, for weak tunneling $\tilde{\mathcal{S}}/\hbar \gg 1$, the low-energy sector of the (modified) AFMR can be described as a two-state model with basis states $|\uparrow\rangle$ and $|\downarrow\rangle$. In this approximation, $\hat{H} = -(\tilde{\Delta}/2)(|\uparrow\rangle\langle\downarrow| + |\downarrow\rangle\langle\uparrow|)$, where the parameters of the original microscopic Hamiltonian enter $\tilde{\Delta}$.

For any operator \hat{O} , the transition matrix element between $|g\rangle$ and $|e\rangle$ can be evaluated from

$$\begin{aligned} \langle e|\hat{O}|g\rangle &= \frac{1}{2} \left(\langle\uparrow|\hat{O}|\uparrow\rangle - \langle\downarrow|\hat{O}|\downarrow\rangle \right. \\ &\quad \left. + \langle\uparrow|\hat{O}|\downarrow\rangle - \langle\downarrow|\hat{O}|\uparrow\rangle \right). \end{aligned} \quad (\text{A.9})$$

For $h_x \gg \tilde{\omega}_0$ the state $|\uparrow\rangle$ describes a Gaussian probability distribution for \mathbf{n} in the plane $\perp \mathbf{B}$ with variance $\langle\uparrow|\cos^2\phi|\uparrow\rangle = 2\tilde{J}/N\hbar\tilde{\omega}_0 = 1/(\tilde{\mathcal{S}}/\hbar)$ (Sec. 2.2). Expanding $\sin\phi \simeq \pm(1 - \cos^2\phi/2)$ around $\phi \simeq \pi/2$ and $\phi \simeq 3\pi/2$, respectively, we obtain

$$\begin{aligned} |\langle e|\sin\phi|g\rangle| &\simeq \frac{1}{2} |\langle\uparrow|\sin\phi|\uparrow\rangle - \langle\downarrow|\sin\phi|\downarrow\rangle| \\ &\simeq 1 - \frac{\tilde{J}}{N\hbar\tilde{\omega}_0}. \end{aligned} \quad (\text{A.10})$$

The terms $\langle\downarrow|\sin\phi|\uparrow\rangle$ are of order $\exp(-\tilde{\mathcal{S}}/\hbar)$ and hence negligible in the weak tunneling regime. Similarly, we also find

$$|\langle e|\sin^3\phi|g\rangle| \simeq 1 - 3\frac{\tilde{J}}{N\hbar\tilde{\omega}_0}. \quad (\text{A.11})$$

From Eqs. (A.10) and (A.11) follows the AC susceptibility for the modified AFMR, Eq. (3.39).

Appendix B

Spin cluster qubits: effective coupling Hamiltonians

B.1 Spin chains

Here, we derive the effective coupling Hamiltonian in Eq. (4.12) from Eq. (4.11). The first and second term in Eq. (4.12) result from $J_*(t)\hat{\mathbf{s}}_{n_c}^I \cdot \hat{\mathbf{s}}_1^{\text{II}}$ in the microscopic coupling. Decomposing $\hat{\mathbf{s}}_{n_c}^I \cdot \hat{\mathbf{s}}_1^{\text{II}} = \hat{s}_{n_c,z}^I \hat{s}_{1,z}^{\text{II}} + (\hat{s}_{n_c}^{I+} \hat{s}_1^{\text{II}-} + \hat{s}_{n_c}^{I-} \hat{s}_1^{\text{II}+})/2$ in terms of spin ladder operators, one can readily evaluate the matrix elements in the two-qubit product basis. Because, by definition, $\hat{S}_z|0\rangle = (\hbar/2)|0\rangle$ and $\hat{S}_z|1\rangle = (-\hbar/2)|1\rangle$ and $\hat{s}_{n_c,z}^I \hat{s}_{1,z}^{\text{II}}$ conserves the z -component of total spin in each cluster separately it follows that

$${}_I\langle 0 | {}_{\text{II}}\langle 1 | \hat{s}_{n_c,z}^I \hat{s}_{1,z}^{\text{II}} | 1 \rangle_I | 0 \rangle_{\text{II}} = 0. \quad (\text{B.1})$$

Similarly, all other off-diagonal elements of $\hat{s}_{n_c,z}^I \hat{s}_{1,z}^{\text{II}}$ vanish. Because of

$${}_I\langle 0 | \hat{s}_{n_c}^{I\pm} | 0 \rangle_I = {}_I\langle 1 | \hat{s}_{n_c}^{I\pm} | 1 \rangle_I = 0, \quad (\text{B.2})$$

the transverse exchange $J_*(t)(\hat{s}_{n_c}^{I+} \hat{s}_1^{\text{II}-} + \hat{s}_{n_c}^{I-} \hat{s}_1^{\text{II}+})/2$ has finite matrix elements only between the states $|0\rangle_I |1\rangle_{\text{II}}$ and $|1\rangle_I |0\rangle_{\text{II}}$. This completes the proof that the intercluster exchange term $J_*(t)\hat{\mathbf{s}}_{n_c}^I \cdot \hat{\mathbf{s}}_1^{\text{II}}$ leads to the first and second term in Eq. (4.12).

It remains to show that a possible change in intracluster exchange interaction constants during two-qubit gate operation, $J_*(t) \sum_{j=1}^{n_c-1} (v_j^I \hat{\mathbf{s}}_j^I \cdot \hat{\mathbf{s}}_{j+1}^I + v_j^{\text{II}} \hat{\mathbf{s}}_j^{\text{II}} \cdot \hat{\mathbf{s}}_{j+1}^{\text{II}})$, only leads to a term proportional to $\mathbf{1}$ in Eq. (4.12). This term conserves all components of the total spin of clusters I and II,

$$[\hat{S}_\alpha^I, \sum_{j=1}^{n_c-1} v_j^I \hat{\mathbf{s}}_j^I \cdot \hat{\mathbf{s}}_{j+1}^I] = 0, \quad (\text{B.3})$$

for $\alpha = x, y, z$, and similarly for II. Hence, all off-diagonal matrix elements such as ${}_I\langle 1|v_j^I \hat{\mathbf{s}}_j^I \cdot \hat{\mathbf{s}}_{j+1}^I|0\rangle_I$ vanish. Finally, because $|1\rangle_I = \hat{S}^{I-}|0\rangle_I = 2\hat{S}_x^I|0\rangle_I$, with Eq. (B.3),

$$\begin{aligned}
& {}_I\langle 1|_{{\text{II}}}\langle 0|J_*(t) \sum_{j=1}^{n_c-1} v_j^I \hat{\mathbf{s}}_j^I \cdot \hat{\mathbf{s}}_{j+1}^I|1\rangle_I|0\rangle_{{\text{II}}} \\
&= {}_I\langle 0|_{{\text{II}}}\langle 0|2\hat{S}_x^I J_*(t) \sum_{j=1}^{n_c-1} v_j^I \hat{\mathbf{s}}_j^I \cdot \hat{\mathbf{s}}_{j+1}^I 2\hat{S}_x^I|0\rangle_I|0\rangle_{{\text{II}}} \quad (\text{B.4}) \\
&= {}_I\langle 0|_{{\text{II}}}\langle 0|J_*(t) \sum_{j=1}^{n_c-1} v_j^I \hat{\mathbf{s}}_j^I \cdot \hat{\mathbf{s}}_{j+1}^I (2\hat{S}_x^I)^2|0\rangle_I|0\rangle_{{\text{II}}} \\
&= {}_I\langle 0|_{{\text{II}}}\langle 0|J_*(t) \sum_{j=1}^{n_c-1} v_j^I \hat{\mathbf{s}}_j^I \cdot \hat{\mathbf{s}}_{j+1}^I|0\rangle_I|0\rangle_{{\text{II}}}.
\end{aligned}$$

In the second line of Eq. (B.4) we have invoked that $\{|0\rangle_I, |1\rangle_I\}$ belong to one spin-1/2 doublet, the third line then follows from Eq. (B.3). With a similar argument it can be shown that all diagonal matrix elements in the two-qubit product basis are equal and $J_*(t) \sum_{j=1}^{n_c-1} (v_j^I \hat{\mathbf{s}}_j^I \cdot \hat{\mathbf{s}}_{j+1}^I + v_j^{\text{II}} \hat{\mathbf{s}}_j^{\text{II}} \cdot \hat{\mathbf{s}}_{j+1}^{\text{II}})$ translates into a term $J_o(t)\mathbf{1}$ in the effective coupling Hamiltonian Eq. (4.12).

Finally, we prove Eq. (4.14) which implies that, for isotropic intracluster exchange interactions, the effective two-qubit Hamiltonian is also of Heisenberg form. For simplicity, we omit the label I of the spin cluster qubit in the following. In order to formally calculate $\langle 0|\hat{s}_{n_c,z}|0\rangle$ and $|\langle 1|\hat{s}_{n_c,x}|0\rangle|$, we define the spin operators

$$\hat{S}'_\alpha = \hat{S}_\alpha - \hat{s}_{n_c,\alpha} = \sum_{j=1}^{n_c-1} \hat{s}_{j,\alpha} \quad (\text{B.5})$$

of all but the outermost spin $j = n_c$ of the cluster. Generally, $|0\rangle$ can be expanded as

$$|0\rangle = a|\Psi\rangle|\uparrow\rangle + b|\Phi\rangle|\downarrow\rangle, \quad (\text{B.6})$$

where $|\Psi\rangle$ and $|\Phi\rangle$ describe the normed states of the leftmost $n_c - 1$ spins in the array and a and b are real numbers. Because $\hat{S}_z|0\rangle = (\hbar/2)|0\rangle$, $|\Psi\rangle$ and $|\Phi\rangle$ are eigenstates of \hat{S}'_z with eigenvalues 0 and \hbar , respectively. $\hat{S}_x|0\rangle = (\hbar/2)|1\rangle$ is an \hat{S}_z eigenstate with eigenvalue $-(\hbar/2)$, such that $b|\Phi\rangle = -a\hat{S}'_+|\Psi\rangle$, and

$$\begin{aligned}
|0\rangle &= a(|\Psi\rangle|\uparrow\rangle - \hat{S}'_+|\Psi\rangle|\downarrow\rangle), \\
|1\rangle &= a(\hat{S}'_-|\Psi\rangle|\uparrow\rangle - (1 - \hat{S}'_- \hat{S}'_+)|\Psi\rangle|\downarrow\rangle), \\
a &= \frac{1}{\sqrt{1 + \langle \Psi|\hat{S}'_- \hat{S}'_+|\Psi\rangle}}. \quad (\text{B.7})
\end{aligned}$$

From Eq. (B.7) we calculate

$$\begin{aligned}\langle 0|\hat{s}_{n_c,z}|0\rangle &= -\langle 1|\hat{s}_{n_c,z}|1\rangle = \frac{1}{2} \frac{1 - \langle \Psi|\hat{S}'_-\hat{S}'_+|\Psi\rangle}{1 + \langle \Psi|\hat{S}'_-\hat{S}'_+|\Psi\rangle}, \\ \langle 1|\hat{s}_{n_c,x}|0\rangle &= \frac{1}{2} \frac{1 - \langle \Psi|\hat{S}'_-\hat{S}'_+|\Psi\rangle}{1 + \langle \Psi|\hat{S}'_-\hat{S}'_+|\Psi\rangle},\end{aligned}\tag{B.8}$$

which proves Eq. (4.14).

B.2 Larger spins

The matrix elements in Eq. (4.41) can be calculated from coherent state spin path integrals [120]. We focus on strong easy plane systems, $k_z > 0$ and $k_z(s_1^2 + s_2^2)/J \gg 1$. Following the standard approach for antiferromagnetic systems (Sec. 2.1.2), the partition function of the two-spin system is expressed as path integral over the Néel vector \mathbf{n} and homogeneous magnetization \mathbf{l} defined by $\mathbf{s}_1 = s_1\mathbf{n} + \mathbf{l}$ and $\mathbf{s}_2 = -s_2\mathbf{n} + \mathbf{l}$, where $\mathbf{n} \cdot \mathbf{l} = 0$. Integrating out \mathbf{l} in a saddle point approximation and parameterizing

$$\mathbf{n} = \begin{pmatrix} \sin\theta \cos\phi \\ \sin\theta \sin\phi \\ \cos\theta \end{pmatrix},\tag{B.9}$$

the Euclidean action of the system can be written as [49, 50]

$$\begin{aligned}L &= \frac{\hbar^2}{2J} \left(\dot{\theta}^2 + \sin^2\theta \dot{\phi}^2 \right) + k_z(s_1^2 + s_2^2) \cos^2\theta \\ &\quad + i\Delta s \hbar \dot{\phi} (1 - \cos\theta),\end{aligned}\tag{B.10}$$

where the last factor accounts for the difference $\Delta s = s_2 - s_1$ of the spin quantum numbers and $\dot{\phi} = \partial_\tau \phi$ is the imaginary time derivative. In the limit of strong anisotropy, $k_z(s_1^2 + s_2^2)/J \gg 1$, Eq. (B.10) can be expanded to second order in $\theta - \pi/2$ and the fluctuations are integrated out, leading to

$$Z = \int \mathcal{D}\phi \exp \left(- \int_0^{\hbar\beta} d\tau L[\phi]/\hbar \right)\tag{B.11}$$

with an effective Euclidean Lagrangean

$$L_E[\phi] = \frac{\hbar^2 \dot{\phi}^2}{2J} + i\Delta s \hbar \dot{\phi}.\tag{B.12}$$

After continuation to real time, by a canonical transformation we obtain the Hamiltonian of the system in terms of the Néel vector operator,

$$\hat{H} = \frac{J}{2\hbar^2} (\hat{p}_\phi - \hbar\Delta s)^2, \quad (\text{B.13})$$

where

$$\hat{\mathbf{n}} = \begin{pmatrix} \cos \hat{\phi} \\ \sin \hat{\phi} \\ 0 \end{pmatrix}, \quad \hat{\mathbf{I}} = \frac{1}{2} \begin{pmatrix} 0 \\ 0 \\ \hat{p}_\phi/\hbar - \Delta s \end{pmatrix}, \quad (\text{B.14})$$

and \hat{p}_ϕ is the momentum operator conjugate to the in-plane polar angle ϕ , $[\hat{p}_\phi, \hat{\phi}] = -i\hbar$. By inspection of Eq. (B.13), we find that the spin system Eq. (4.37) has been mapped onto the Hamiltonian of a particle on a ring threaded by a magnetic flux $\propto \Delta s$. In particular, for half-integer Δs , the Hamiltonian has a ground state doublet $\{|0\rangle, |1\rangle\}$ with wave functions $\psi_0(\phi) = \exp(i(m+1)\phi)/\sqrt{2\pi}$ and $\psi_1(\phi) = \exp(im\phi)/\sqrt{2\pi}$, where $m = \lfloor \Delta s \rfloor$. From $\hat{s}_{1,x} \simeq s_1 \cos \hat{\phi}$ and $\hat{s}_{2,x} \simeq -s_2 \cos \hat{\phi}$, one immediately obtains Eq. (4.41).

Bibliography

- [1] Plinius maior, *Natural History* (Harvard University Press, Cambridge (Mass.), 1938).
- [2] D. C. Mattis, *The Theory of Magnetism I* (Springer, Berlin, 1981).
- [3] D. A. Thompson and J. S. Best, *IBM J. Res. Dev.* **44**, 311 (2000).
- [4] D. Loss and D. P. DiVincenzo, *Phys. Rev. A* **57**, 120 (1998).
- [5] A. J. Leggett, in *Quantum tunneling of Magnetization*, edited by L. Gunther and B. Barbara (Kluwer, Dodrecht, 1995).
- [6] J. L. van Hemmen and A. Süto, *Europhys. Lett.* **1**, 481 (1986).
- [7] J. L. van Hemmen and A. Süto, *Physica B&C* **141**, 37 (1986).
- [8] M. Enz and R. Schilling, *J. Phys. C: Solid State Phys.* **19**, L711 (1986).
- [9] M. Enz and R. Schilling, *J. Phys. C: Solid State Phys.* **19**, 1765 (1986).
- [10] E. M. Chudnovsky and L. Gunther, *Phys. Rev. Lett.* **60**, 661 (1988).
- [11] D. Loss, D. P. DiVincenzo, and G. Grinstein, *Phys. Rev. Lett.* **69**, 3232 (1992).
- [12] J. von Delft and C. L. Henley, *Phys. Rev. Lett.* **69**, 3236 (1992).
- [13] J. R. Friedman, M. P. Sarachik, J. Tejada, and R. Ziolo, *Phys. Rev. Lett.* **76**, 3830 (1996).
- [14] L. Thomas *et al.*, *Nature (London)* **383**, 145 (1996).
- [15] A. Fort *et al.*, *Phys. Rev. Lett.* **80**, 612 (1998).
- [16] M. N. Leuenberger and D. Loss, *Europhys. Lett.* **46**, 692 (1999).
- [17] M. N. Leuenberger and D. Loss, *Phys. Rev. B* **61**, 1286 (2000).

- [18] W. Wernsdorfer and R. Sessoli, *Science* **284**, 133 (1999).
- [19] W. Wernsdorfer *et al.*, *Europhys. Lett.* **50**, 552 (2000).
- [20] M. N. Leuenberger and D. Loss, *Phys. Rev. B* **61**, 12200 (2000).
- [21] Y. Nakamura, Y. A. Pashkin, and J. S. Tsai, *Nature* **398**, 786 (1999).
- [22] D. Vion *et al.*, *Science* **296**, 886 (2002).
- [23] Y. Yu *et al.*, *Science* **296**, 889 (2002).
- [24] D. D. Awschalom *et al.*, *Phys. Rev. Lett.* **68**, 3092 (1992).
- [25] D. D. Awschalom, D. P. DiVincenzo, and J. F. Smyth, *Science* **258**, 414 (1992).
- [26] S. Gider *et al.*, *Science* **268**, 77 (1995).
- [27] A. Garg, *Phys. Rev. Lett.* **70**, 2198 (1993).
- [28] D. D. Awschalom *et al.*, *Phys. Rev. Lett.* **70**, 2199 (1993).
- [29] A. Garg, *Phys. Rev. Lett.* **71**, 4249 (1993).
- [30] D. D. Awschalom, D. P. DiVincenzo, G. Grinstein, and D. Loss, *Phys. Rev. Lett.* **71**, 4276 (1993).
- [31] A. Garg, *Phys. Rev. Lett.* **74**, 1458 (1995).
- [32] P. W. Shor, in *Proceedings of the 35th Annual Symposium on the Foundations of Computer Science (IEEE, Los Alamitos, California, 1994)*, pp. 124-133.
- [33] L. K. Grover, *Phys. Rev. Lett.* **79**, 325 (1997).
- [34] G. Burkard, D. Loss, and D. P. DiVincenzo, *Phys. Rev. B* **59**, 2070 (1999).
- [35] B. E. Kane, *Nature* **393**, 133 (1998).
- [36] J. M. Kikkawa, I. P. Smorchkova, N. Samarath, and D. D. Awschalom, *Science* **277**, 1284 (1997).
- [37] P. Recher, E. V. Sukhorukov, and D. Loss, *Phys. Rev. Lett.* **85**, 1962 (2000).
- [38] M. N. Leuenberger and D. Loss, *Nature* **410**, 789 (2001).

- [39] P. Ball, *Nature* **404**, 918 (2000).
- [40] S. Datta and B. Das, *Appl. Phys. Lett.* **56**, 665 (1990).
- [41] S. Datta, *Electronic Transport in Mesoscopic Systems* (Cambridge University Press, Cambridge, 1995).
- [42] B. J. van Wees *et al.*, *Phys. Rev. Lett.* **60**, 848 (1998).
- [43] D. A. Wharam *et al.*, *J. Phys. C: Solid State Phys.* **21**, L209 (1998).
- [44] F. Meier and D. Loss, *Phys. Rev. Lett.* **86**, 5373 (2001).
- [45] F. Meier and D. Loss, *Phys. Rev. B* **64**, 224411 (2001).
- [46] A. Honecker, F. Meier, D. Loss, and B. Normand, *Eur. Phys. J. B* **27**, 487 (2002).
- [47] A. Auerbach, *Interacting Electrons and Quantum Magnetism* (Springer, New York, 1994).
- [48] A. Garg, *Europhys. Lett.* **22**, 205 (1993).
- [49] B. Barbara and E. M. Chudnovsky, *Phys. Lett. A* **145**, 205 (1990).
- [50] I. V. Krive and O. B. Zaslavskii, *J. Phys.: Condens. Matter* **2**, 9457 (1990).
- [51] D. Loss, in *Dynamical Properties of Unconventional Magnetic Systems*, edited by A. T. Skjeltorp and D. Sherrington (Kluwer, Dodrecht, 1998).
- [52] R. Rajaraman, *Solitons and Instantons* (North-Holland, Amsterdam, 1996).
- [53] H. Kleinert, *Path integrals in quantum mechanics, statistics and polymer physics* (World Scientific, Singapore, 1995).
- [54] U. Weiss, *Quantum dissipative systems* (World Scientific, Singapore, 1999).
- [55] K. L. Taft *et al.*, *J. Am. Chem. Soc.* **116**, 823 (1994).
- [56] A. Caneschi *et al.*, *Chem. Eur. J.* **2**, 1379 (1996).
- [57] O. Waldmann *et al.*, *Inorg. Chem.* **38**, 5879 (1999).
- [58] O. Waldmann *et al.*, *Inorg. Chem.* **40**, 2986 (2001).

- [59] J. van Slageren *et al.*, Chem. Eur. J **8**, 277 (2002).
- [60] A. Cornia, A. G. M. Jansen, and M. Affronte, Phys. Rev. B **60**, 12177 (1999).
- [61] B. Normand, X. Wang, X. Zotos, and D. Loss, Phys. Rev. B **63**, 184409 (2001).
- [62] B. Pilawa *et al.*, J. Magn. Magn. Mat. **177-181**, 748 (1998).
- [63] M. Affronte, J. C. Lasjaunias, A. Cornia, and A. Caneschi, Phys. Rev. B **60**, 1161 (1999).
- [64] M.-H. Julien *et al.*, Phys. Rev. Lett. **83**, 227 (1999).
- [65] A. Chiolero and D. Loss, Phys. Rev. Lett. **80**, 169 (1998).
- [66] J.-M. Duan and A. Garg, J. Phys.: Condens. Matter **7**, 2171 (1995).
- [67] J. Schnack and M. Luban, Phys. Rev. B **63**, 014418 (2001).
- [68] O. Waldmann, Phys. Rev. B **65**, 024424 (2002).
- [69] O. Waldmann, Europhys. Lett. **60**, 302 (2002).
- [70] V. Y. Irkhin and M. I. Katsnelson, Z. Phys. B – Condensed Matter **62**, 201 (1986).
- [71] A. Lascialfari *et al.*, Phys. Rev. B **57**, 1115 (1998).
- [72] W. Wernsdorfer *et al.*, Phys. Rev. Lett. **84**, 2965 (2000).
- [73] A. Lascialfari *et al.*, Phys. Rev. Lett. **81**, 3773 (1998).
- [74] A. Cornia, A. Fort, M. G. Pini, and A. Rettori, Europhys. Lett. **50**, 88 (2000).
- [75] J. N. S. Evans, *Biomolecular NMR Spectroscopy* (Oxford University Press, Oxford, 1995).
- [76] C. P. Slichter, *Principles of Magnetic Resonance* (Springer, Berlin, 1990).
- [77] E. M. Chudnovsky, J. Magn. Magn. Mat. **140-144**, 1821 (1995).
- [78] A. Chiolero and D. Loss, Phys. Rev. B **56**, 738 (1997).
- [79] B. A. Ivanov and V. E. Kireev, JETP Lett. **69**, 398 (1999).

- [80] F. K. Larsen *et al.*, *Angew. Chem. Int. Edit.* **42**, 101 (2003).
- [81] R. Lü, P. Zhang, J.-L. Zhu, and L. Chang, *Phys. Rev. B* **56**, 10993 (1997).
- [82] R. Lü *et al.*, *Eur. Phys. J. B* **14**, 349 (2000).
- [83] H.-B. Braun and D. Loss, *Int. J. Mod. Phys. B* **10**, 219 (1996).
- [84] S. Allen and D. Loss, *Physica A* **239**, 47 (1997).
- [85] J. G. E. Harris *et al.*, *Phys. Rev. B* **60**, 3453 (1999).
- [86] V. Y. Golyshev and A. F. Popkov, *Europhys. Lett.* **29**, 327 (1995).
- [87] M. Affronte *et al.*, *Phys. Rev. Lett.* **88**, 167201 (2002).
- [88] E. M. Chudnovsky and D. A. Garanin, *Phys. Rev. Lett.* **87**, 187203 (2001).
- [89] K. Park *et al.*, *Phys. Rev. B* **65**, 014426 (2002).
- [90] K. M. Mertes *et al.*, *Phys. Rev. Lett.* **87**, 227205 (2001).
- [91] C. H. Bennett and D. P. DiVincenzo, *Nature* **404**, 247 (2000).
- [92] D. P. DiVincenzo, *Science* **270**, 255 (1995).
- [93] J. I. Cirac and P. Zoller, *Nature* **404**, 579 (2000).
- [94] J. Levy, *Phys. Rev. A* **64**, 052306 (2001).
- [95] V. Privman, I. D. Vagner, and G. Kventsel, *Phys. Lett. A* **239**, 141 (1998).
- [96] G. Feher, D. K. Wilson, and E. A. Gere, *Phys. Rev. Lett.* **3**, 25 (1959).
- [97] F. Meier, J. Levy, and D. Loss, *Phys. Rev. Lett.* **90**, 047901 (2003).
- [98] D. P. DiVincenzo *et al.*, *Nature* **408**, 339 (2000).
- [99] J. Levy, *Phys. Rev. Lett.* **89**, 147902 (2002).
- [100] D. A. Lidar and L.-A. Wu, *Phys. Rev. Lett.* **88**, 017905 (2002).
- [101] D. Bacon, K. R. Brown, and K. B. Whaley, *Phys. Rev. Lett.* **87**, 247902 (2001).
- [102] S. C. Benjamin, *Phys. Rev. Lett.* **88**, 017904 (2002).
- [103] A. Barenco *et al.*, *Phys. Rev. A* **52**, 3457 (1995).

- [104] R. Orbach, Phys. Rev. **112**, 309 (1958).
- [105] L. R. Walker, Phys. Rev. **116**, 1089 (1959).
- [106] E. Lieb, T. Schultz, and D. Mattis, Ann. Phys. (N.Y.) **16**, 407 (1961).
- [107] E. Lieb and D. Mattis, Journ. Math. Phys. **3**, 749 (1962).
- [108] J. C. Bonner and M. E. Fisher, Phys. Rev. **135**, A640 (1964).
- [109] N. Nagaosa, *Quantum Field Theory in Strongly Correlated Electronic Systems* (Springer, Berlin, 1999).
- [110] G. Burkard, D. Loss, D. P. DiVincenzo, and J. A. Smolin, Phys. Rev. B **60**, 11404 (1999).
- [111] A. V. Khaetskii, D. Loss, and L. Glazman, Phys. Rev. Lett. **88**, 186802 (2002).
- [112] J. Schliemann, A. V. Khaetskii, and D. Loss, Phys. Rev. B **66**, 245303 (2002).
- [113] K. Blum, *Density Matrix Theory and Applications* (Plenum Press, New York, 1996).
- [114] S. Eggert and I. Affleck, Phys. Rev. B **46**, 10866 (1992).
- [115] J. Villain, Physica B&C **79**, 1 (1975).
- [116] R. Raussendorf and H. J. Briegel, Phys. Rev. Lett. **86**, 5188 (2001).
- [117] J. Kempe, D. Bacon, D. A. Lidar, and K. B. Whaley, Phys. Rev. A **63**, 042307 (2001).
- [118] B. Koiller, X. Hu, and S. Das Sarma, Phys. Rev. Lett. **88**, 027903 (2002).
- [119] D. Gatteschi, A. Caneschi, L. Pardi, and R. Sessoli, Science **265**, 1054 (1994).
- [120] J. R. Klauder, Phys. Rev. D **19**, 2349 (1979).
- [121] P. Ball, Nature **406**, 118 (2000).
- [122] C. P. Collier *et al.*, Science **285**, 391 (1999).
- [123] D. I. Gittins, D. Bethell, D. J. Schiffrin, and R. J. Nichols, Nature **408**, 67 (2000).

- [124] C. Joachim, J. K. Gimzewski, and A. Aviram, *Nature* **408**, 541 (2000).
- [125] D. Rugar, *J. Appl. Phys.* **68**, 1169 (1990).
- [126] Z. Liu, Y. Dan, Q. Jinjun, and Y. Wu, *J. Appl. Phys.* **91**, 8843 (2002).
- [127] S. A. Wolf *et al.*, *Science* **294**, 1488 (2001).
- [128] *Semiconductor Spintronics and Quantum Computation*, edited by D. D. Awschalom, D. Loss, and N. Samarth (Springer, Berlin, 2002).
- [129] D. Forster, *Hydrodynamic Fluctuations, Broken Symmetry, and Correlation Functions* (W. A. Benjamin, Reading, 1975).
- [130] J. C. Slonczewski, *Phys. Rev. B* **39**, 6995 (1989).
- [131] H. Castella, X. Zotos, and P. Prelovsek, *Phys. Rev. Lett.* **74**, 972 (1995).
- [132] X. Zotos, *Phys. Rev. Lett.* **82**, 1764 (1999).
- [133] J. V. Alvarez and C. Gros, *Phys. Rev. Lett.* **88**, 077203 (2002).
- [134] F. Meier and D. Loss, *Phys. Rev. Lett.* **90**, 167204 (2003).
- [135] J. J. Sakurai, *Modern Quantum Mechanics* (Addison-Wesley, Reading, 1994).
- [136] E. Fradkin, *Field Theories of Condensed Matter Systems* (Addison-Wesley, Reading, 1991).
- [137] F. D. M. Haldane, *Phys. Rev. Lett.* **45**, 1358 (1980).
- [138] F. D. M. Haldane, *Phys. Rev. Lett.* **50**, 1153 (1983).
- [139] I. Affleck, *J. Phys.: Condens. Matter* **1**, 3047 (1989).
- [140] R. Shankar, *Int. J. Mod. Phys. B* **4**, 2371 (1990).
- [141] D. L. Maslov and M. Stone, *Phys. Rev. B* **52**, R5539 (1995).
- [142] S. Eggert, I. Affleck, and M. Takahashi, *Phys. Rev. Lett.* **73**, 332 (1994).
- [143] A. V. Sologubenko *et al.*, *Phys. Rev. B* **64**, 054412 (2001).
- [144] C. Hess *et al.*, *Phys. Rev. B* **64**, 184305 (2001).
- [145] D. Loss and P. M. Goldbart, *Phys. Lett. A* **215**, 197 (1996).
- [146] A. H. Miklich *et al.*, *Appl. Phys. Lett.* **66**, 230 (1995).

- [147] Z. Zhang *et al.*, Appl. Phys. Lett. **73**, 2036 (1998).
- [148] A. Brataas, Y. Tserkovnyak, G. E. W. Bauer, and B. I. Halperin, Phys. Rev. B **66**, 060404(R) (2002).
- [149] Y. Aharonov and A. Casher, Phys. Rev. Lett. **53**, 319 (1984).
- [150] R. L. Douglass, Phys. Rev. **129**, 1132 (1963).

Lebenslauf

von Florian Meier

- 28.3.1976 Geburt in Eggenfelden als erster Sohn von L. Meier und C. Meier (geb. Richthammer)
- 1982-84 Besuch der Grundschule Putzbrunn
- 1984-86 Besuch der Grundschule Wunsiedel
- 1986-94 Besuch des Luisenburg-Gymnasiums Wunsiedel
Abitur im Juli 1994
- 1994-96 Physikstudium an der Ludwig-Maximilians-Universität München
- 1996-97 Physikstudium an der University of Oxford
- 1997-99 Physikstudium an der Ludwig-Maximilians-Universität München
Diplomarbeit: “Josephson-Effekte in schwach wechselwirkenden Bose-Kondensaten” unter Betreuung von Prof. W. Zwerger
Diplom im März 1999
- 1999-2000 Grundwehrdienst
- 2000-03 Promotionsstudium in Physik an der Universität Basel
Dissertation: “Coherent spin dynamics and magnetization transport in nanoscale magnetism” unter Betreuung von Prof. D. Loss
Promotion im Mai 2003

Meine universitäre Ausbildung verdanke ich den folgenden Professoren: I. J. R. Aitchison, H. Bross, C. Bruder, J. Cardy, J. Chalker, D. Dürr, M. Faessler, J. Feldmann, H. Fritzsche, S. Goedecker, D. Habs, I. Kogan, D. Loss, W. Metzner, H. Nöth, A. Sachs, A. Schenzle, H.-J. Schneider, D. Sherrington, H. Spohn, A. Staude, R. B. Stinchcombe, W. Stocker, P. Talkner, A. M. Tsvelik, H. Walther, J. Wess, K. Wolffhardt, H. Wolter, J. M. Yeomans, I. Zupancic, W. Zwerger.

Veröffentlichungen

F. Meier, J. Levy, and D. Loss,
Quantum computing with antiferromagnetic spin clusters,
cond-mat/0304296.

F. Meier and D. Loss,
Magnetization transport and quantized spin conductance,
Phys. Rev. Lett. **90**, 167204 (2003).

F. Meier, J. Levy, and D. Loss,
Quantum computing with spin cluster qubits,
Phys. Rev. Lett. **90**, 047901 (2003).

F. Meier and D. Loss,
Coherent spin quantum dynamics in antiferromagnetic molecular rings,
to appear in Physica B.

M. N. Leuenberger, F. Meier, and D. Loss,
Quantum spin dynamics in molecular magnets,
Monatshefte für Chemie **134**, 217 (2003).

A. Honecker, F. Meier, D. Loss, and B. Normand,
Quantum coherent dynamics in molecular magnetic rings,
Eur. Phys. J. B **27**, 487 (2002).

F. Meier and D. Loss,
*Thermodynamics and spin tunneling dynamics in ferric wheels
with excess spin*,
Phys. Rev. B **64**, 224411 (2001).

F. Meier and D. Loss,
Electron and nuclear spin dynamics in antiferromagnetic molecular rings,
Phys. Rev. Lett. **86**, 5373 (2001).

F. Meier and W. Zwerger,
Josephson tunneling between weakly interacting Bose-Einstein condensates,
Phys. Rev. A **64**, 033610 (2001).

F. Meier and W. Zwerger,
Anomalous condensate fluctuations in strongly interacting superfluids,
Phys. Rev. A **60**, 5133 (1999).